Experimental Study of Inertial Particles in Turbulence: Preferential Concentration, Relative Velocity and Droplet Collisions

Colin P. Bateson

A dissertation
submitted in partial fulfillment of the
requirements for the degree of

Doctor of Philosophy

University of Washington

2016

Reading Committee:

Alberto Aliseda, Chair

John C. Kramlich

James J. Riley

Program Authorized to Offer Degree:
Mechanical Engineering

University of Washington

Abstract

Experimental Study of Inertial Particles in Turbulence: Preferential Concentration, Relative Velocity and Droplet Collisions

Colin P. Bateson

Chair of the Supervisory Committee:
Associate Professor Alberto Aliseda
Mechanical Engineering

Wind tunnel experiments are used to investigate the dynamics of small inertial particles (water droplets $\approx 5 - 150\,\mu$m in diameter) in homogeneous, isotropic, slowly decaying grid turbulence ($\mathrm{Re}_\lambda \approx 350$, $\varepsilon \approx 0.1\,\mathrm{m^2 s^{-3}}$). Phase Doppler Particle Analyzer (PDPA), high-speed imaging measurements and a new 4-frame N+2 Best Estimated Position Particle Tracking Velocimetry (PTV) algorithm are used to determine droplet locations in space and time.

Experimental evidence is found of droplet preferential concentration and enhanced relative velocity resulting from the droplets' inertial interactions with the underlying turbulence. The Radial Distribution Functions (RDF) have strong peaks at small separation distances that indicate the preferential accumulation of droplets in the flow. This result is confirmed by Voronoi analysis results that show droplets with small Voronoi areas (high local concentration) are present with a probability higher than that predicted by a Random Poisson Process (RPP). The 2D RDFs show a consistent trend where the results from the horizontal imaging configurations are always lower than those from the vertical planes. The Voronoi PDFs indicate the same anisotropic particle clustering. This observation that the 2D RDFs and Voronoi PDFs are sensitive to orientation is likely the first experimental evidence that clustering is anisotropic and stronger in the direction of gravity.

Droplet settling velocities are conditioned on Voronoi areas to assess the relationship between settling and local droplet concentration. The settling velocity data, for all but the largest droplets, presents a clear dependency on Voronoi area: as the Voronoi areas decrease (local concentration increases), collective settling effects result in enhanced settling velocities.

The non-dimensional Closing Time ratio is proposed as a new way to interpret droplet relative velocity data that incorporates the fact that the particle collision probabilities depend on both a large relative closing velocity and a small separation distance. The Closing Time shows that once the relative velocity joint PDF is re-framed in the correct non-dimensional ratio, it provides a more meaningful representation of the inertial droplet dynamics. Beyond the ability to provide qualitative understanding, the main benefit of the Closing Time statistics is that they can be used to compute collision probabilities from experimentally measurable quantities of separation distance and relative velocity. This is a novel contribution that provides significant new understanding and quantifying capability for inertial particle dynamics leading to collisions.

TABLE OF CONTENTS

LIST OF FIGURES

LIST OF TABLES

ACKNOWLEDGMENTS

I would like to express my sincerest appreciation and gratitude to...

...Alberto Aliseda for his guidance, flexibility, and patience over the better part of a decade. I have really enjoyed working with you and I consider myself extremely lucky to have such a great advisor and friend.

...Everyone who chipped in along the way: Marita Rodriguez, Alberto Molina, Yoon Baek Kim, Gary Ngai, Serge Matveyev, Riccardo Jordan de Urries, Alicia Clark, and Peter Huck.

...Lynne. Thank you for your love, understanding, and support. You saw me through the worst of it.

...My friends, especially Keith, for your counsel, encouragement and all the timely distractions. You don't stay in school for this long unless you're having a lot of fun!

...My brothers and sister. You have been there since the beginning. Thanks for teaching me to be proud and keeping me humble.

...Most important, my parents. Thank you for your never-ending love and support. I cherish you both and I could not have asked for a better foundation upon which to build my dreams.

DEDICATION

to all of my teachers.

AUTHOR'S NOTE

The research described in this dissertation builds upon work originally published in my masters thesis (Bateson, 2010) and a journal paper (Bateson and Aliseda, 2012). As a result, figures, tables, and some sections of text are drawn directly from those documents. Figures and tables published previously in Bateson and Aliseda (2012) are reproduce with permission from Springer, as indicated in their captions. Excerpts of text in Sections 2.1, 2.2.1, 2.2.4, 2.3.1, 2.3.2, and 4.1.2 that were published previously are included in this dissertation with permission from Springer. These excerpts are acknowledged here rather than in the body of the dissertation. Figures, images, tables and text already published in Bateson (2010) can be found in Sections 1.1-1.4, 2.2.1, 2.2.4, 2.3, and 4.1.1. They are acknowledged here rather than in the body of the dissertation.

Chapter 1

INTRODUCTION

The process of rain formation is a multiscale and multiphysics problem that, despite having been studied for centuries, still defies successful quantitative modeling. Droplet collision-coalescence is a key element of warm rain formation—an element that is necessary to explain the rapid growth of condensation droplets beyond small diameters (on the order of 10 μm) and the spectrum broadening where droplet diameter distributions grow wider with long tails that reach tens or even hundreds of microns as observed from radar backscattering field measurements. This area of multiphase turbulent flows still presents multiple important open questions.

The human relationship with rain is complex, since rain is simultaneously a nuisance and a necessity, so an interest in the rain formation process should not be surprising. The motivation to understand rain is strong enough that scientists have persevered despite the ever-increasing complexity that each new study uncovers. The earliest studies were conducted prior to fully understanding the turbulent fluid environment that is a defining characteristic of rain clouds. Thankfully, the explosion of advanced experimentation has allowed researchers to probe more deeply into the complexity that air turbulence adds to the rain formation problem. Even today, despite the sustained exponential growth of computer processing speed, the range of scales encompassed by the precipitation process requires computing power that will not be available for many decades. Experimental observations are equally challenging. Making precise measurements of the small-scale precipitation processes from a platform that

must survive violent cloud environments is hazardous and expensive. But it is exactly these types of challenges that make this problem so interesting, and why this interest has endured for decades. Today, the scientific community has a solid qualitative understanding of how precipitation forms, but portions of the process still lack the understanding necessary to make accurate quantitative predictions. This dissertation contributes results from laboratory experiments on droplet behavior in turbulence that are relevant to the collision-coalescence process during warm-rain formation.

1.1 Background on Turbulent-Induced Collisions and Rain Formation

The first study done on the role of turbulence in rain formation was that of Arenberg (1939). Using a sinusoidal representation for the turbulent velocity fluctuations, this seminal study considered how turbulence could bring droplets together, but not the conditions necessary for actual collisions. East and Marshall (1954) took the work on droplet collision efficiencies by Langmuir (1948) and applied it to a model of collisions that included both random turbulent motion and gravity. East and Marshall found that drops with similar sizes have similar responses to turbulence, but drops with differing sizes can develop significant relative velocities due to turbulent fluctuations in the carrier flow. They concluded that the random motion of turbulence can be regarded as being equivalent to increasing the acceleration due to gravity. As a result, their model predicts zero increase in the collision rate of similarly-sized drops, but a significant increase for dissimilarly-sized drops. This is due to the fact that their model does not account for spatial variation in the turbulent fluctuations, which would impose differing velocities on neighboring drops even if their size or inertia was similar.

Saffman and Turner (1956) performed what is regarded as the seminal work on the problem of turbulence-induced collisions. They improved on the analysis of East and Marshall (1954) by including a mechanism that would allow equally-sized drops to collide. Saffman and Turner proposed that there are two mechanisms by which turbulence creates the relative

velocities between drops that lead to collision: (1) relative velocities due to spatial variations in the turbulent air motion, and (2) relative velocity created by different drop responses to turbulent motions owing to their different inertia. Saffman and Turner (1956) dismissed the use of the collision efficiencies reported by Langmuir (1948) since they were calculated for drops in a steady, laminar flow around a fixed, large sphere. Instead Saffman and Turner assumed collision efficiencies of 1.0 for all their drops.

de Almeida (1976, 1979a) performed a battery of Monte Carlo simulations to study the increase in the geometric collision efficiency resulting from turbulence. These studies then applied those results to calculate the evolution of cloud droplet size spectra (de Almeida, 1979b) and found that the coalescence process was greatly enhanced by turbulence. However, Grover and Pruppacher (1985) suggested that the work by de Almeida (de Almeida, 1976, 1979a,b) used the wrong part of the turbulent energy spectrum for the drop sizes considered and, for this reason, underestimated inertial effects in the calculations. While this does not totally disqualify those early results, it does question their quantitative validity.

Reuter et al. (1988) published a novel study that incorporated a stochastic model of the drop-collision process in the turbulent carrier flow. In addition to shear and inertia effects, turbulence was thought to create collisions via an "over-lapping eddy" mechanism. In short, this mechanism can be described as the interaction between two turbulent eddies carrying with them droplets entrained in their circular motion. When the eddies collide, the droplets they are carrying may collide as well. Reuter et al. (1989) then developed a probabilistic collection kernel that included the effect of overlapping eddies and used it to calculate the evolution of a cloud droplet spectrum. Those studies concluded that turbulence contributes to the broadening of the droplet spectra, and increasing turbulence intensity increases spectra broadening, but the droplet growth rate remained slow even for the most vigorous turbulence studied.

Khain and Pinsky (1995) studied the increase in volume swept by a drop falling in a number of different shear flows. Pinsky and Khain (1997) increased the complexity level of the previous study to a full two-dimensional (2D) Batchelor turbulence model and studied the relative motion of inertial drops with respect to the fluid. In a companion paper (Khain and Pinsky, 1997), those results were used to study the increase in swept volume with simulated turbulence, and the effects on the collision kernel and the collision-coalescence process as a whole. This was the first application of these concepts to flows with turbulent dissipation rates and droplet radii relevant to cumulus clouds. Pinsky et al. (1999) performed a computational study on the collision enhancement factor in turbulent flows, which they calculated using the superposition method. This method involves calculating the number of droplet collisions per unit time per unit volume that occur in a turbulent flow seeded with a certain number of droplets of certain sizes and comparing the number of collisions to the number that would occur in a purely laminar flow where relative velocity is due only to gravitational settling. In general, they found that the collision enhancement factor is a random variable in time and space, but that the mean value is greater than that for gravity-induced collisions in laminar air. Pinsky et al. (2000, 2001) showed that the effects of turbulence and inertia influence the collision kernel by increasing the swept volume of a collector droplet and increasing the collision enhancement factor. Most important, they showed that the collision enhancement factor is very sensitive to increases in relative velocity, and creating relative velocity between drops is exactly what turbulence does.

1.2 The Dynamics of Inertial Particles in Turbulence

Taylor (1921) was the first to consider how a particle might behave in a statistically homogeneous turbulent fluid. Assuming that the particle has no inertia and therefore follows the turbulent velocity fluctuations perfectly, Taylor (1921) derived an equation for the distance traveled by the particle as a function of time, the root mean square of the turbulent velocity

fluctuations, and the correlation coefficient for the particle velocity at two instances in time. Effectively, Taylor's equation describes how inertia-less particles will diffuse away from a point source as a result of turbulent fluctuations.

Starting from first principles, Maxey and Riley (1983) derived an equation of motion for a rigid spherical particle in a turbulent air flow that includes particle inertia. Their work has contributed significantly to the turbulent collision problem by allowing researchers to use their computational tools to study, in detail, particle-turbulence interactions. As a result, a number of interesting phenomena have been discovered. Maxey performed a series of 2D simulations studying particle motion in simplified representations of turbulence (Maxey and Corrsin, 1986; Maxey, 1987a,b) and found that inertia caused heavy particles to concentrate in regions of high strain and low vorticity, an effect known now as preferential concentration. Another phenomenon found for particles in turbulent flows is that turbulence increases particle settling velocity by preferentially sweeping the particles into downward-flowing regions (Maxey and Corrsin, 1986; Wang and Maxey, 1993).

1.2.1 Preferential Concentration

Preferential concentration is the name given to the tendency of particles to accumulate in certain regions of the flow, among other reasons, because they move away from regions of high vorticity and collect in regions of high strain (Figure 1.1). Squires and Eaton (1990) found this tendency in their results from Direct Numerical Simulations (DNS) of isotropic turbulence and reported that it was most pronounced for an "intermediate time constant". Wang and Maxey (1993) used DNS to show that preferential concentration is the result of the small scale motions of turbulence. For this reason, the Kolmogorov scale was shown to be the correct scale to define the fluid time constant, and they found that preferential concentration was most pronounced when the Stokes number (Eq. 1.1) of the particles was approximately 1. When the results from Squires and Eaton (1990) are rescaled using the

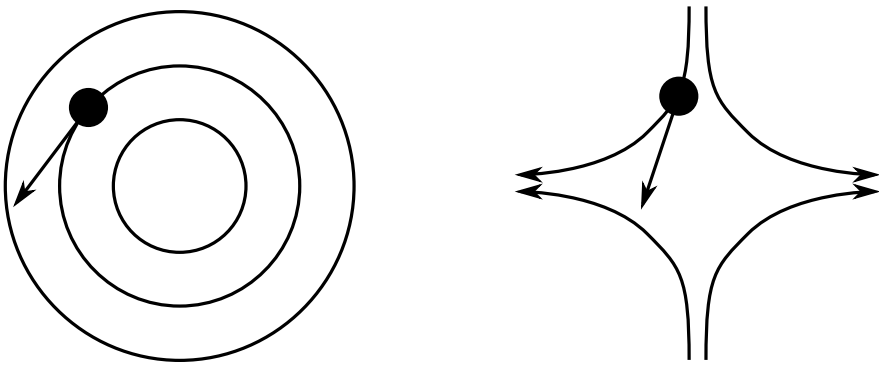

Figure 1.1: Inertial dynamics resulting from fluid flow structures. A cartoon depicting how particles move away from the center of high-vorticity regions (left) and towards the center of high-strain regions (right).

Kolmogorov time scale, their numbers agree with those of Wang and Maxey. The Stokes number is a non-dimensional parameter that quantifies the effect of a particle's inertia on its interactions with the turbulent flow structures. The Stokes number (St) is defined as the ratio of a particle's viscous relaxation time (τ_p) to a turbulent time scale (τ_f). Following Wang and Maxey (1993), the Kolmogorov time scale (τ_κ) is used for a turbulent time scale.

$$St = \frac{\tau_p}{\tau_\kappa} \tag{1.1}$$

The time scales are defined as follows:

$$\tau_p = \frac{d^2 \, \rho_p / \rho_{air}}{18 \, \nu_{air}}, \tag{1.2}$$

$$\tau_\kappa = \left(\frac{\nu_{air}}{\varepsilon} \right)^{1/2}, \tag{1.3}$$

where d is the droplet's diameter, ρ_p is the droplet's density, ρ_{air} is the density of air, ν_{air} is the kinematic viscosity of air, and ε is the turbulent kinetic energy dissipation rate in the turbulent carrier flow.

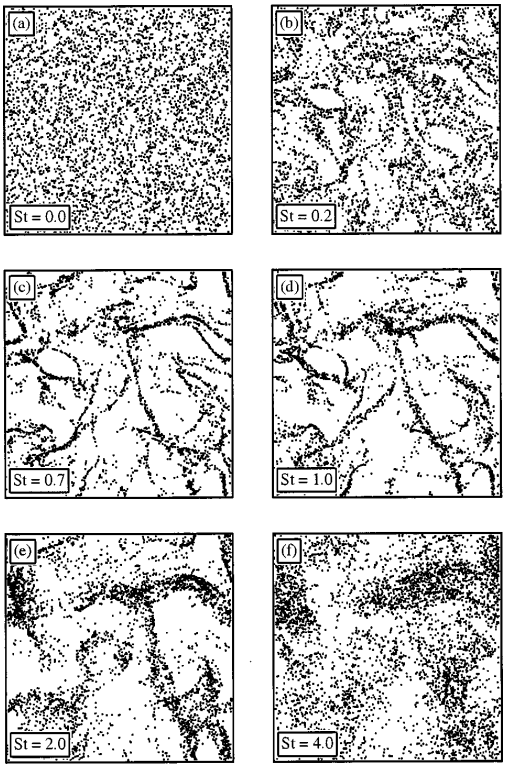

Figure 1.2: Particle clustering as a function of Stokes number. These two-dimensional images, each corresponding to a different Stokes number, show that clustering is most evident when $St \approx 1$. Reprinted from Reade and Collins (2000), with the permission of AIP Publishing.

Figure 1.2 from Reade and Collins (2000) is an illustration of how preferential concentration is a function of the Stokes number. When $St \approx 1$, the particles tend to cluster tightly together into streaks, as opposed to $St = 0$ or $St = 4.0$ when the particles are much more evenly mixed throughout the simulation volume. Eaton and Fessler (1994) measured preferential concentration in their experiments with particles in a turbulent channel flow, providing experimental validation to the DNS results published up to that point.

1.2.2 Enhanced Gravitational Settling

When gravitational forces are considered, heavy particles have a vertical velocity relative to the turbulent fluid that causes them to interact with vortical structures via a process known as the "crossing trajectories" effect (Wells and Stock, 1983). The particles are swept preferentially to the downward regions in the flow and, as a result, the mean effect of the turbulence on the particles is an increased settling velocity (Wang and Maxey, 1993). Aliseda et al. (2002) conducted an experimental study of the settling rate enhancement for inertial particles in turbulent flows. Aliseda et al. found that the heavy particles they injected into homogeneous isotropic turbulence settled significantly faster than they would in a quiescent fluid, validating this same result from earlier computational simulations, but also discovered that there is a collective effect that enhances this settling velocity increase beyond what had been predicted theoretically or numerically (as point-particle simulations in the dilute regime can not reproduce this type of behavior).

1.3 The Turbulent Collision Equation

Sundaram and Collins (1997) studied the cloud drop collision problem by running a full DNS of stationary, forced turbulent flow with particle motion determined by a simplified form of the equation of motion from Maxey and Riley (1983). Using a development analogous to that of the kinetic theory of gases, Sundaram and Collins developed the following equation

for the collision frequency of a monodisperse particle population:

$$N_c = \frac{1}{2}\pi\sigma^2\, n^2\, g(\sigma) \int \mathbf{w}\, P(\mathbf{w}\,|\,\sigma) d\mathbf{w} \tag{1.4}$$

where σ is the particle diameter, n is the particle number density, $g(\sigma)$ is the particle radial distribution function (RDF) evaluated at contact (the separation distance between two particles at the instant of collision, which in a monodisperse particle population is a distance equal to the particle's diameter), $\mathbf{w}$ is the relative velocity, and $P(\mathbf{w} \mid \sigma)$ is the relative velocity probability density function (PDF) conditioned on the contact distance.

1.3.1 The Radial Distribution Function

Sundaram and Collins (1997) were the first to use the RDF to quantify the local concentration of particles in a multiphase flow as the result of preferential concentration. The RDF measures the probability of finding a droplet in a spherical shell of thickness dr and radius r_i, centered on the position of each droplet. The RDF is normalized such that a population of drops that are separated by a totally random distribution of distances will have an RDF that is equal to 1 everywhere. If the droplets concentrate preferentially, the RDF will reflect this local concentration by having a value greater than 1. Originally derived for the field of solid mechanics to describe the distribution of atoms in crystalline or glassy structures, Sundaram and Collins (1997) showed that this statistic is directly proportional to the rate of collisions in a monodisperse droplet system (Eq. 1.4).

1.3.2 Collision Enhancement

Wang et al. (2000) conducted 3D direct numerical simulations (DNS) of particle-laden turbulent flows with the intent to study the separate contributions to the collision kernel from relative velocity enhancements and preferential concentration. Wang et al. referred to the increases in particle relative velocity due to turbulence as "the turbulent transport effect",

and to the tendency of particles to preferentially concentrate in turbulent flows as "the accumulation effect". They confirmed that the turbulent transport effect is a result of the large scale turbulent motions (scales around the flow integral timescale, T_e). The turbulent transport effect enhances collisions by a factor of u'/v_κ, where u' is the root mean square of the velocity fluctuations and v_κ is the Kolmogorov velocity scale. This effect peaks when the particle inertial response time is the same order of magnitude as the flow integral timescale ($t_p/T_e = \mathcal{O}(1)$). Wang et al. showed that the accumulation effect enhances collisions by a factor of $(1 + 0.14\mathrm{Re}_\lambda)$, and this enhancement is most significant when $t_p/t_\kappa = 1$, where t_κ is the Kolmogorov time scale used to characterized the small scale fluid motions.

Wang et al. (2006) calculated droplet sizes and growth rates using a Monte-Carlo approach to capture the stochastic nature of droplet growth from collision events. They studied three aspects related to the influence of air turbulence on stochastic coalescence: (1) the enhancement of geometric collision rates, (2) the changes to the collision efficiencies, and (3) the stochastic fluctuations and correlations in the collision-coalescence process. Wang et al. (2006) showed a 40% reduction in the time for drizzle formation to occur with a turbulence dissipation rate (ε) of $400\,\mathrm{cm}^2/\mathrm{s}^3$ as compared to the time for drizzle formation due to solely gravity-induced collisions ($\varepsilon = 0\,\mathrm{cm}^2/\mathrm{s}^3$).

In 2008, the same group from the University of Delaware published two studies on the turbulent collision problem related to rain formation: Ayala et al. (2008); Wang et al. (2008). Ayala et al. presented a DNS study of the geometric collision rates of cloud droplets in homogeneous isotropic turbulence that focused specifically on the parameter range relevant to clouds in terms of the droplet sizes (d) and turbulent energy dissipation rates ($\varepsilon = 10 - 400\,\mathrm{cm}^2/\mathrm{s}^3$, $d = 20 - 120\,\mu\mathrm{m}$). Ayala et al. showed that air turbulence enhances the geometric collision rate for cloud droplets over that for gravity-induced collisions alone, and they attributed this enhancement to both the increase in radial relative velocity and preferential concentration that result from inertial droplet interactions with turbulent flow

structures. Wang et al. (2008), on the other hand, focused on the turbulent collision efficiency calculated using a novel hybrid DNS technique (HDNS). Their HDNS approach combines a pseudospectral simulation of the air turbulence with an improved superposition method to account for both the local and large-scale flow disturbances created by the droplets. Understanding the local flow disturbances around the droplets is very important because they have been shown to explain how small droplets on collision trajectories with larger drops can flow around the large drops and avoid the collisions. Using their HDNS, Wang et al. calculated increased collision efficiencies due to turbulence. They attributed this efficiency increase to the air turbulence reducing the aerodynamic interactions between droplets that can sometimes disrupt collisions.

In summary, multiple studies from different groups and with different methodologies have shown that turbulence enhances the collision kernel for cloud droplets in the following ways: (1) shear and differential acceleration increase the relative velocity between droplets; (2) preferential accumulation increases the values of functions that depend on pair statistics, like the RDF and the relative velocity, which determine the collision kernel (Pinsky et al., 1997; Sundaram and Collins, 1997; Wang et al., 2000; Zhou et al., 2001; Ayala et al., 2008); (3) selective changes in the settling rate increase the relative velocity between drops (Wang and Maxey, 1993; Aliseda et al., 2002); and (4) turbulence increases collision efficiency (Pinsky et al., 1999, 2000; Wang et al., 2005; Wang et al., 2008). Many of these studies, however, were conducted outside the parameter range relevant to cloud microphysical processes (Vaillancourt and Yau, 2000).

1.4 Warm-Rain Formation

Even today, the warm-rain formation process is not fully understood. We know that clouds form when water vapor in the air condenses onto condensation nuclei, forming tiny droplets. The condensation process is the dominant growth mechanism for these nascent drops until

they reach a size of approximately $10\,\mu m$. These small drops would grow very slowly if only via collision and coalescence because they have negligible settling velocities.

Condensation is a well-understood process that can be modeled accurately. The condensation growth rate per unit volume is inversely proportional to the droplet's radius. As a droplet grows in size, the speed with which it grows slows down. Over time, the condensation process creates a population of droplets with similar sizes ("spectrum narrowing"). Since settling velocity is a function of droplet size, these drops rarely grow via gravitationally-induced collision and coalescence because they all fall with similar speeds. Droplets larger than $100\,\mu m$ have significant settling velocities and therefore large relate velocity with the condensation droplets. Consequently, fast drop growth is the result of gravity-induced collisions of collector drops (in the $100\,\mu m$ range) with smaller droplets (in the $10\,\mu m$ range)—another well understood and accurately modeled process.

Once a drop grows large enough to settle with centimeter-per-second speeds, it collides with the smaller droplets surrounding it. The drop grows quickly as it falls, colliding with more droplets at an increasing rate as the drop continues to grow and its settling velocity increases. Due to the runaway nature of the gravity-induced collision process, only a small number of "lucky" collector droplets need to grow to $100\,\mu m$ in order to start this fast collision process and initiate precipitation in a cloud. The size range between $10\,\mu m$ and $100\,\mu m$ is known as the size gap. The primary mechanism for fast growth through the size gap is debated and the uncertainty surrounding size gap droplet growth is a large source of uncertainty in the current physical models of warm-rain formation. One hypothesis is that the inertia of the condensation droplets interacts with the turbulence to enhance their naturally slow collision rate and allows the droplets to grow across the size gap. Computational simulations have shown this is true in idealized cases. This dissertation explores the validity of this hypothesis using laboratory experiments that cover the range of turbulent dissipation rates and droplet sizes that are relevant to warm rain formation in cumulus clouds.

1.5 The Scope of this Dissertation

This dissertation documents wind tunnel experiments aimed at improving the current understanding and quantitative modeling of the interaction between turbulence and inertial droplets. These experiments were conducted in a parameter range relevant to cloud microphysics. Chapter 2 includes a description of the wind tunnel experiment, as well as the characterization of the disperse (droplets) and carrier (air) phases of the flow. Details concerning our particle tracking velocimetry (PTV) measurement techniques can be found in Chapter 3. Chapter 4 presents results and analysis of our measurements of preferential concentration. Chapter 5 focuses on droplet velocity measurements, including settling velocity, relative velocity, and both of these conditioned on local particle concentration. Chapter 6 is a summary of the main conclusions of this dissertation.

Chapter 2
EXPERIMENTAL SETUP

The experiments in this dissertation were conducted in a horizontal, blow-down, low-speed wind tunnel. Water droplets were injected into nearly homogeneous and isotropic grid-generated turbulence. The characterization of the turbulence in the carrier flow was done by Constant Temperature Hotwire Anemometry (CTA or HWA). Droplet sizes, velocities, and one-dimensional spatial distribution measurements were carried out with a Phase Doppler Particle Analyzer (PDPA). High-speed camera images and Particle Tracking Velocimetry (PTV) were used to measure droplet velocities and spatial distributions in two dimensions.

2.1 Description of the Wind Tunnel

The wind tunnel has an 8:1 ratio expansion section containing wire mesh and honeycomb screens that break down possible turbulent structures and eliminate the large-scale rotational motion of the air flow created by the axial compressor. The air flows into a plenum (2.25 m long and 1.2 m $\times$ 1.2 m square) to dampen the remaining anisotropic turbulent fluctuations. At the end of the flow conditioning section, the flow goes through a dual-purpose grid: it generates homogeneous, isotropic, slowly decaying turbulence; and serves as the support for the droplet injection system.

The experiments presented here were conducted in two different test sections. The first test section was replaced with a newer test section that is 50% longer and has redesigned access windows. The new wind tunnel test section (1.05 m $\times$ 1.05 m constant cross section and 4.5 m long) is formed by acrylic panels to allow optical access to the flow. There are seven tall and slender windows, regularly spaced along on the side of the tunnel, that allow

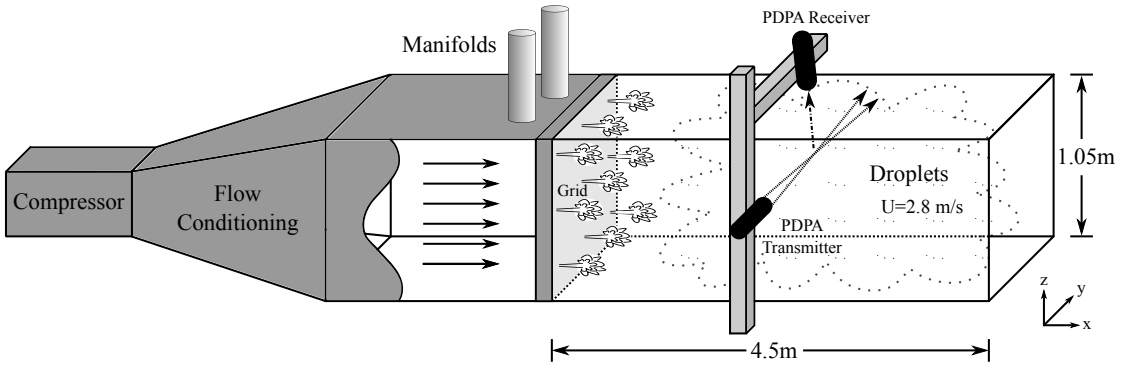

Figure 2.1: The wind tunnel. An illustration of the wind tunnel experiment showing the main components and the test section dimensions. Adapted from Bateson and Aliseda (2012) with permission from Springer.

for instrumentation to be inserted into the flow. The locations of these window define our measurement stations along the length of the tunnel. Figure 2.1 shows the locations of the measurement stations for both the first and second wind tunnel test sections. Where necessary, a note regarding whether the measurements were made in the first or second test section is added to the discussion in this dissertation. At the downstream end of the tunnel, a large diffuser decelerates the flow and discharges it into the atmosphere through a filter that captures the water droplets as they leave the tunnel.

2.2 Carrier Fluid Phase

The air that flows through the tunnel acts as the carrier phase for the multiphase fluid mechanics experiments presented in this dissertation. The wind tunnel generates homogeneous, isotropic, slowly decaying turbulence; a well-understood and easily simulated canonical flow that serves as an excellent background for the study of droplet dynamics in turbulence.

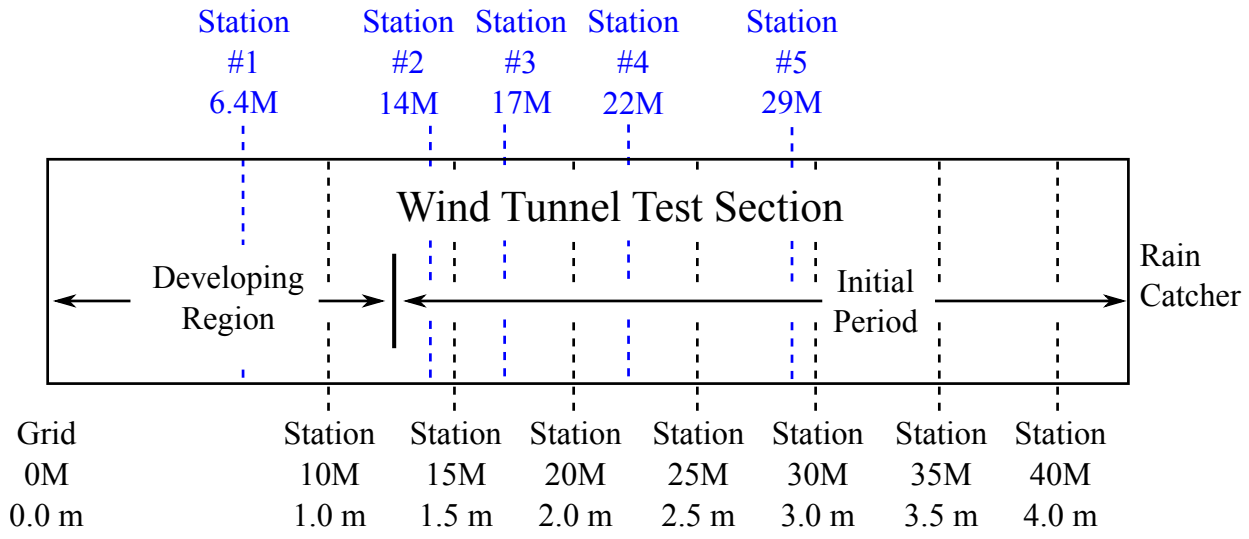

Figure 2.2: Measurement station locations. An illustration showing the measurement stations used throughout these experiments. The newer wind tunnel test section is shown in black along with its measurement stations. These were the locations used for the hotwire measurements and the high-speed imaging. For reference, the measurement stations from the first wind tunnel test section are shown in blue. PDPA measurements were made at these locations.

2.2.1 The Turbulence-Inducing Grid

The turbulence-inducing grid used for the experiments is a 9×9 bi-planar array formed by 1 inch (2.54 cm) diameter aluminum tubes. The water and air supply lines run inside the hollow tubes to each of the eighty-one droplet injectors that are integrated into the intersections of the tubes. The geometry of a turbulence-inducing grid is characterized by the shape of the bars (round tubes), the diameter (d) of the grid tubes, and the grid spacing (M) resulting in two non-dimensional numbers: the grid Reynolds number and the grid solidity (S). The grid spacing, defined as the distance between the center of two adjacent parallel tubes, is 4 inches (10.16 cm). The non-dimensional solidity parameter, defined as the ratio of the obstructed area to the total area of the grid, describes the degree of obstruction the grid creates in the flow. The grid solidity is equal to 0.39 in our experiment. Corrsin (1963) suggested that, in order to avoid the influence of the walls on grid turbulence and ensure that an appreciable part of the tunnel satisfies the criterion for homogeneity, the ratio of the width or height (H) of the wind tunnel to the mesh size (M) should be much greater than one; in the wind tunnel used in this dissertation the value is $H/\mathrm{M} = 11.8$. Similarly, for this "active grid" experiment, the ratio between the gas flow rate injected in the jets and the wind tunnel flow rate is very low ($J = Q_j/Q_{wt} \approx 1 - 2\%$) (Gad-el Hak and Corrsin, 1974).

The homogeneous, isotropic, slowly decaying flow behind a grid can be characterized with the grid Reynolds number, ($\mathrm{Re_M}$), which is defined as $\mathrm{Re_M} = \frac{U_o \mathrm{M}}{\nu}$, where the grid mesh size (M) is the length scale, U_o is the mean free-stream velocity, and ν is the kinematic viscosity of the fluid passing through the grid. The grid mesh size, M, is the same length scale used to non-dimensionalize distances behind the grid. Downstream locations in the flow are described in terms of x/M (i.e. $x = 20\mathrm{M}$), where x is the position along the length of the wind tunnel test section, with $x = 0$ at the grid. Table 2.1 summarizes the dimensions and non-dimensional parameters that describe the active grid used in this dissertation.

The carrier fluid flow downstream of the grid can be divided into two regions. In the

Table 2.1: Important grid dimensions and non-dimensional parameters.

Description	Value
Rod Diameter (d)	2.54 cm
Mesh Size (M)	10.16 cm
Solidity (S)	0.44
Wall Influence ($^{H}/_{M}$)	11.8
Re_M	10,000
Injection Ratio (J)	1-2%

first, the developing region, the wakes behind the grid bars are growing and interacting with each other, and the flow is inhomogeneous and anisotropic. In the second region, the initial period, the non-linear interactions between the different fluid structures coming from the grid have given rise to a fully developed turbulence with a continuous spectrum. The resulting turbulence is nearly homogeneous, isotropic, and slowly decaying. All of the measurements for our experiment were made within the initial period, which is known to extend from approximately 10M to 150M downstream from the grid (Wells and Stock, 1983).

2.2.2 Manipulating the Test Section Velocity Profiles

The velocity profiles in the wind tunnel's first test section originally exhibited very thick regions of slow flow near the tunnel walls. These regions were not traditional boundary layers because the slow flow extend out too far into the tunnel, in a manner inconsistent with being caused only by the walls themselves. A noticeable velocity deficit was measured as far as 30% of the width of the tunnel from the walls. The velocity profile in the first test section more closely resembled a parabolic profile than the expected uniform mean profile.

The high-speed air jets from the droplet injectors, flowing parallel to the free stream,

were found to have a tendency to coalesce into a single jet. As the jets develop downstream, entraining air, they merge until the high momentum fluid injected by the jets is biased towards the tunnel center region. The flow near the walls, where there is no source of injected momentum, is biased towards the slowest velocities.

Dealing with this problem was not straightforward since the atomizing air jets could not be modified without changing the droplet size distribution in the tunnel. Instead, a secondary air jet system was added along the inside surface of the walls. Literature shows evidence that jets located close to walls and surfaces tend to stay close to the wall or surface (the Coanda effect (van Dyke, 1969)), growing as they entrain the outer layer fluid. Thus, by tuning the strength of the wall jets, the tendency of the injector jets to migrate toward the center of the tunnel was corrected by providing enough mass and momentum near the tunnel walls to feed their entrainment. This produced a more uniform velocity profile over a wider region of the wind tunnel test section.

To supply air to the wall jets, four pressure manifolds were designed, constructed and installed just upstream of the grid frame (Figure 2.3). Fed by the laboratory's high-pressure air supply, the manifolds deliver equal flow rates to thirty-six wall jets (nine along each wall so as to align with the grid atomizers). Since the pressure manifolds were size-limited by the dimensions of the grid frame, the manifolds are fed from both ends in order to halve the velocity of the air inside the manifold, thus minimizing the pressure drop along its length. All four manifolds are plumbed together to form a continuous ring. The primary air supply hose is split into four secondary supply hoses that connect to the manifold ring in between each manifold in order to distribute the air equally to the system. The wall jet nozzles consist of 3 in. lengths of $1/8$ in.-O.D. stainless steel tubing. The tubes are glued to flat aluminum bar stock that is attached to the inside of the test section's walls immediately downstream of the grid. The bar stock was selected to be as thin as possible while still being able to fix the wall jet nozzles in place (Figure 2.4).

Figure 2.3: Wall jet manifolds. A photo of the manifolds tucked upstream of the grid. The air supply configuration can be seen in the corner.

Figure 2.4: Wall jet nozzles. A photo of the wall jet nozzles in the aluminum bar used to hold them on the tunnel wall.

2.2.3 Facility Characterization: Velocity Profile and Wall Jet Optimization

After installing the wall jet system, the flow rate that produced the most uniform velocity profile in the tunnel test section had to be selected. Hotwire anemometry had been used to measure the velocity inside the wind tunnel, but this technique proved too time consuming for the iterative task of adjusting the wall jet flow settings and detecting the response to these changes in the measurements of the velocity profile across the test section. The HWA velocity profiles had to be measured point by point, a maximum of only four HWA channels are available, and the results needed to be post-processed before changes could be quantified. Instead, a rake of pitot tubes that could be deployed all the way across the tunnel to measure the entire velocity profile at one time was designed, built and tested to work around the HWA's slow turn-around time.

The pitot rake has twenty-one stagnation pressure tubes equally spaced 5 cm apart along

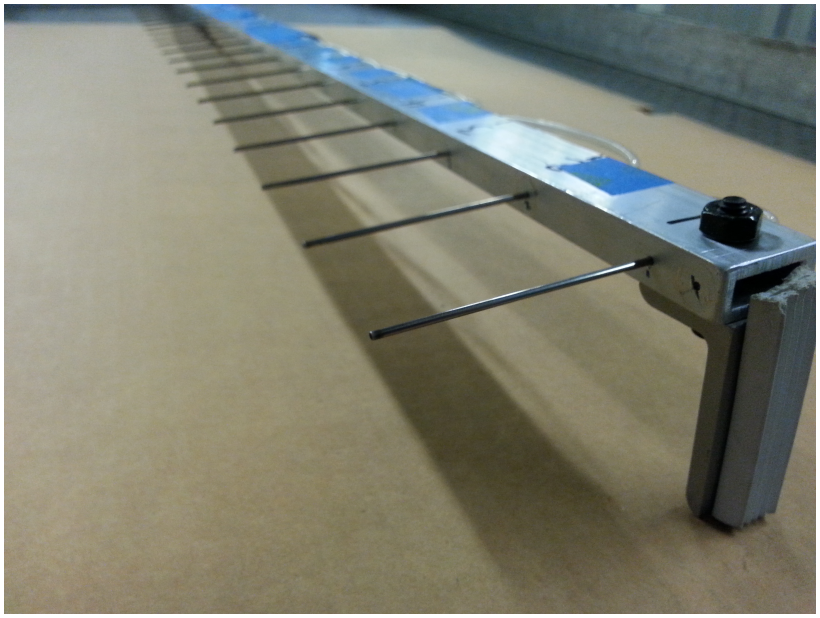

Figure 2.5: The custom-built Pitot rake.

a slender support beam. Flexible tubing connects the pitot tubes to a Scanivalve pressure tap selector switch that allows for quickly cycling through up to forty different pressure sources. The outlet from the Scanivalve is connected to a very sensitive differential pressure transducer selected specifically for its ability to measure low differential pressures under 10 Pa. A LabView Virtual Instrument (VI) was programmed to read out and average the velocity measurements directly, allowing for all the pitot tubes in the rake to be read in less than three minutes. Previously, a single velocity profile with the HWA could take up to an hour. A characterization of the error in the pressure measurements across the taps in the pitot rake is included in the Appendix D. The systematic error across the twenty-one measurement points in the device was less than 0.2%.

The pitot rake was used to optimize the velocity profile at Station 30M in the test section by varying the flow rate supplied to the wall jets. The new velocity profiles are a significant improvement over the previous tunnel's velocity profiles, as can be appreciated in Figures 2.6,

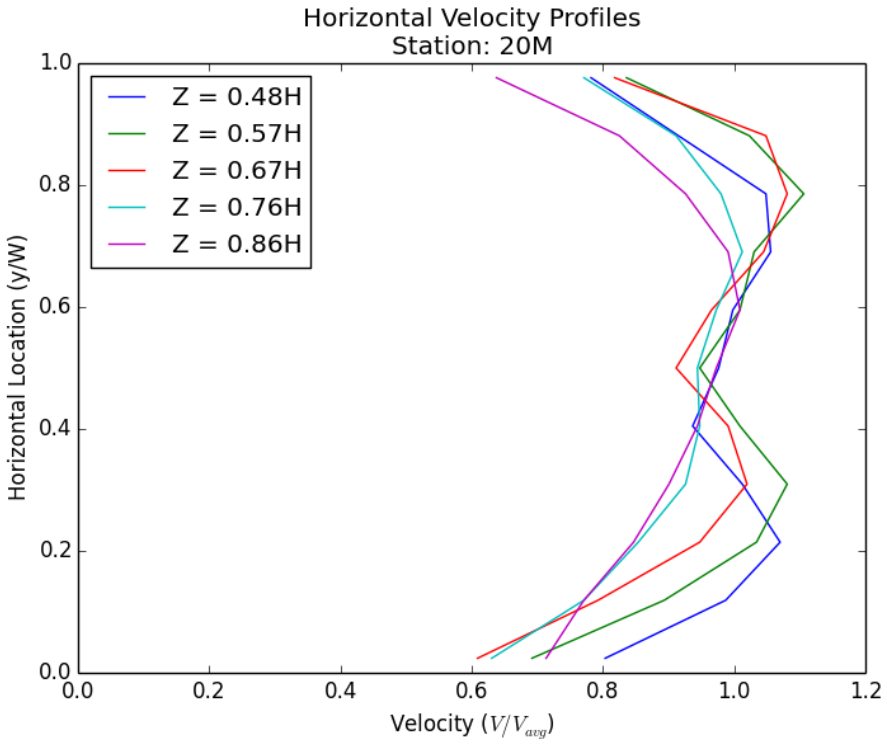

Figure 2.6: Horizontal Velocity Profiles - Station 20M. A plot of the horizontal profiles of the wind tunnel velocity normalized by the mean (V/V_{avg}) measured with the pitot rake at $x = 20$M. Measurements were made from just below the center of the tunnel ($Z = 0.48H$) to the maximum height allowed by the tunnel windows ($Z = 0.86H$).

2.7, and 2.8. When the velocities closest to the walls are excluded, all the profiles deviate less than ±8% from the mean. Previously, the average velocity had varied approximately ±14% from the mean, but the measurement region had to be restricted to a 40 cm-wide band at the center of the tunnel.

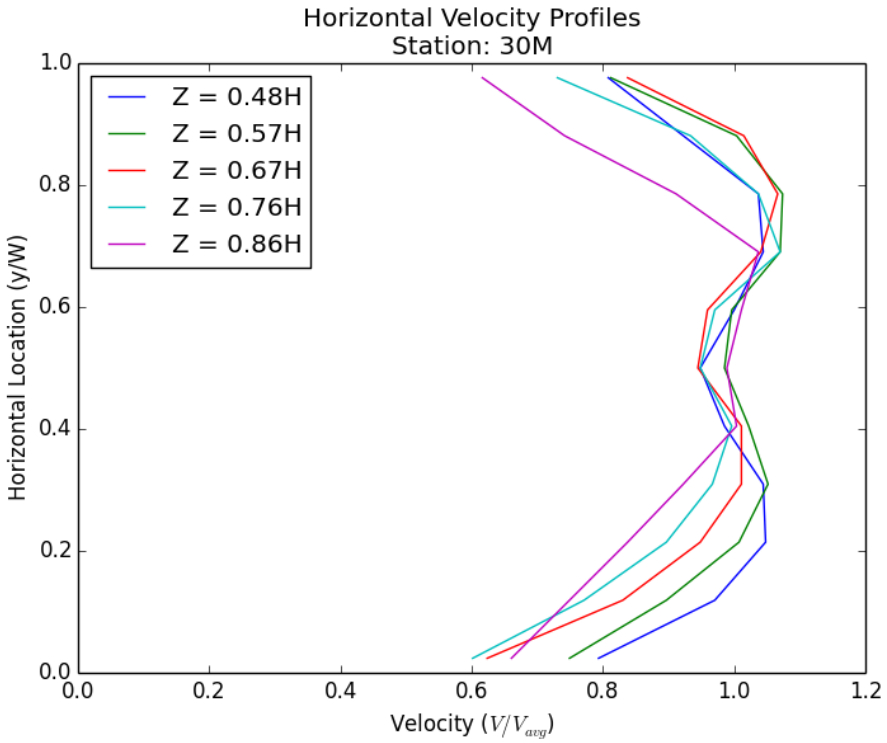

Figure 2.7: Horizontal Velocity Profiles - Station 30M. A plot of the horizontal profiles of the wind tunnel velocity normalized by the mean (V/V_{avg}) measured with the pitot rake at $x = 30$M. Measurements were made from just below the center of the tunnel ($Z = 0.48H$) to the maximum height allowed by the tunnel windows ($Z = 0.86H$).

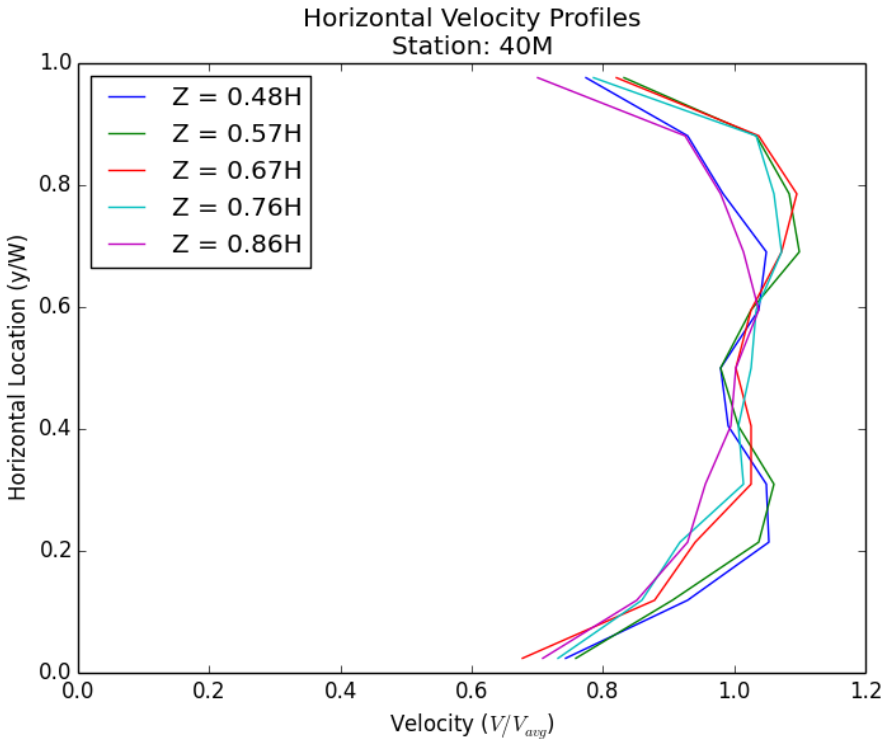

Figure 2.8: Horizontal Velocity Profiles - Station 40M. A plot of the horizontal profiles of the wind tunnel velocity normalized by the mean (V/V_{avg}) measured with the pitot rake at $x = 40$M. Measurements were made from just below the center of the tunnel ($Z = 0.48H$) to the maximum height allowed by the tunnel windows ($Z = 0.86H$).

Table 2.2: Hotwire anemometry settings.

Setting	Value
HWA System	A.A. Lab Systems AN-1005
Sampling Frequency	10 kHz
Number of Samples	2.5×10^6
Wire Diameter	3.8 μm
Wire Length	1.27 mm
Operating Resistance (R_{op})	9.50 Ohms
Overheat Ratio (OHR)	1.5

2.2.4 Characterization of the Carrier Phase

In order to characterize the homogeneous, isotropic turbulence in the wind tunnel, hotwire anemometry* measurements were collected at each of the primary measurement stations ($x =$ 20M, 30M and 40M). At each of these three stations, HWA data was collected on the tunnel centerline, as well as at locations coincident with the high-speed imaging measurements. Since the presence of water drops in the flow is incompatible with hotwire measurements (the water droplet impacts destroy the thin resistive wire at the heart of the fast-response hot wire system), the HWA velocity measurements were done with air flowing through the droplet injectors. Under the low water-air momentum ratio and mass loading at each injector, the droplet formation process does not affect the turbulence levels inside the tunnel significantly. Table 2.2 included details about our HWA system and the settings used.

In order to characterize the turbulent flow in the wind tunnel, and to verify that the turbulence is indeed isotropic and homogeneous, velocity data collected at five measurement

*Hotwire calibration information can be found in the appendix (C.1).

stations were used to calculate the statistics of the turbulence. The average velocity (U), the root mean square (RMS) of the velocity fluctuations (u'), the longitudinal one-dimensional energy spectrum (E_{11}), the turbulent kinetic energy dissipation rate (ε), and the Kolmogorov and Taylor microscales were computed.

The flow downstream from the grid can be divided into four important regions, with two of them found in the wind tunnel test section used in this dissertation. The first region is where the flow is still developing. The wakes behind the grid are growing and interacting, and the flow is inhomogeneous and anisotropic. This region, referred to as the "developing region" is not useful for experimentation. In the second region, which is known as the "initial period," the flow is nearly homogeneous and isotropic, and the turbulence is slowly decaying. This second region is where the study was conducted.

The RMS values of the velocity fluctuations can be used to characterize the intensity of the turbulence and how this intensity decays as the fluid flows downstream from the grid. Multiple studies have investigated the nature of the decay of grid-generated turbulence. Analytical derivations and experiments have all shown that the decay follows a weak power law with an exponent between 1.0 and 1.5. For the sake of simplicity, and since the range over which the measurements in this dissertation were made is rather small ($x = 20\text{M}–40\text{M}$), the turbulence in the wind tunnel was expected to exhibit a linear decay ($n = 1$).

In the graph included as Figure 2.9, the values of $({}^{U}/_{u'})^2$ for this experiment are plotted versus the distance from the grid. Two linear regressions to the data were made, one with all five data points, and a second that excluded the data from the first station (${}^{x}/_{\text{M}} = 6.4$, $x = 0.65\,\text{m}$) since this point does not fit the definition of the "near region." The regression to the data from the last four measurement stations shows that the decay is indeed nearly linear, matching one of the distinguishing characteristics of homogeneous, isotropic grid-turbulence.

Longitudinal 1D turbulent energy spectra (E_{11}) were computed using the velocity measurements collected with hotwire anemometry. Figure 2.10 shows E_{11} plotted as a function of

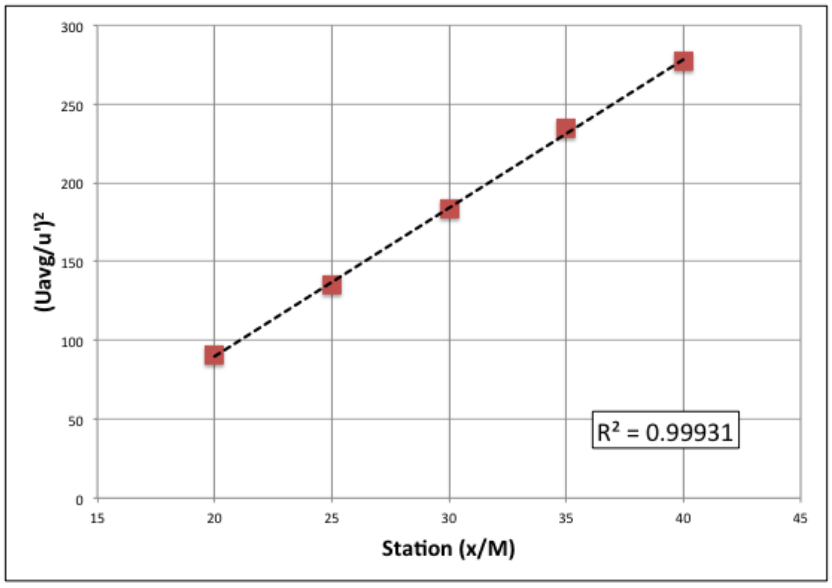

Figure 2.9: Turbulence Decay. A plot showing the linear decay of the turbulence intensity $(U/u')^2$ as a function of distance (x/M) downstream from the grid.

frequency (ω) along the wind tunnel centerline. A dashed line with a slope of $-5/3$ is included as a visual reference to the slope predicted for the inertial range of turbulent energy spectra by Kolmogorov's theory (Kolmogorov, 1941). The well-defined inertial range matches another characteristic of slowly decaying high Reynolds number turbulence. The monotonic decrease in the spectral densities from 20M to 40M shows the rate of decay of the turbulence intensity and dissipation rate.

The second turbulence spectra figure (Figure 2.11) shows the spectra for the three different HWA measurement locations at Station 30M. The agreement between the three locations is excellent, with the spectrum at the horizontal high-speed imaging location nearly indistinguishable from the spectrum at the tunnel centerline. The similarity between these three spectra is a statement of the degree of transverse homogeneity in the wind tunnel.

Table 2.3 contains the relevant flow parameters and scales describing the carrier fluid

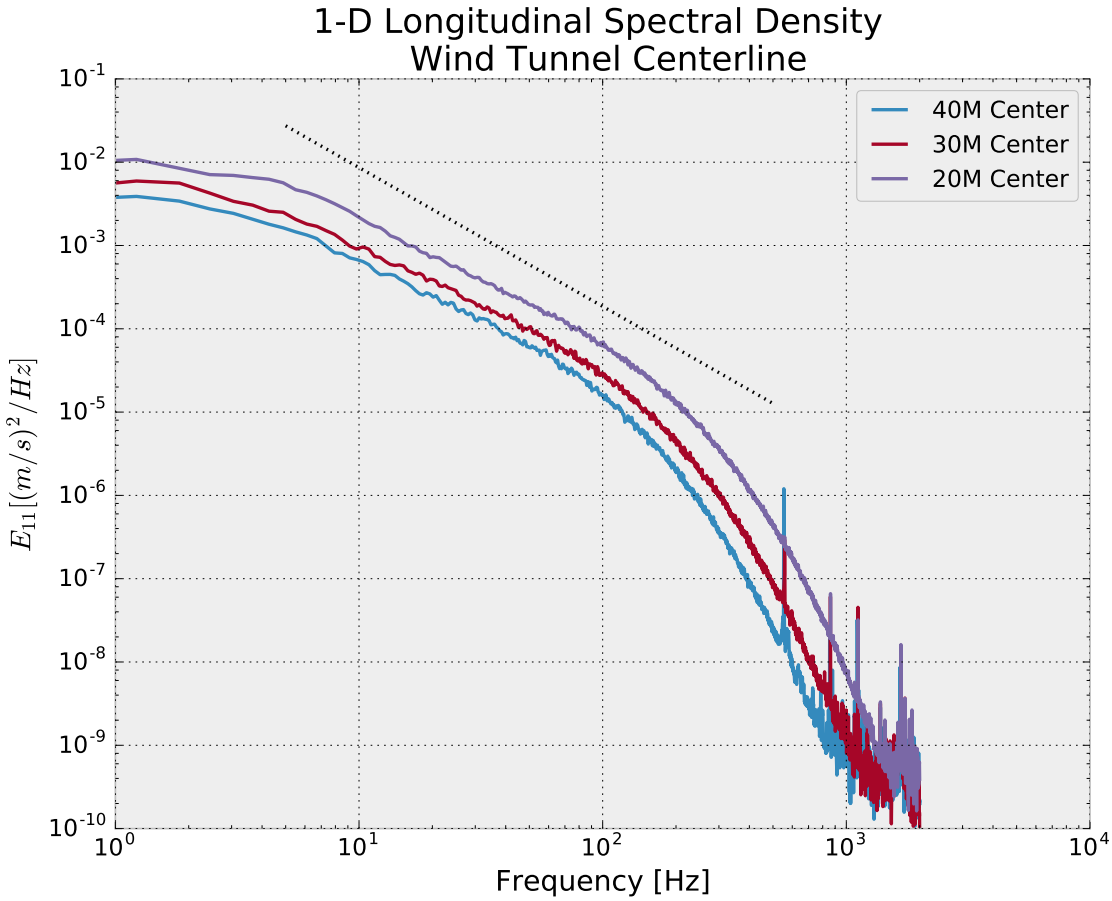

Figure 2.10: 1-D Longitudinal Spectral Density - Wind Tunnel Centerline. A plot of the turbulent energy spectrum from hotwire measurements made at the tunnel centerline for Stations 20M, 30M, and 40M. The dashed line, with a $-5/3$ slope, is included as a visual reference for the slope predicted by Kolmogorov's theory for the inertial range of turbulent energy spectra.

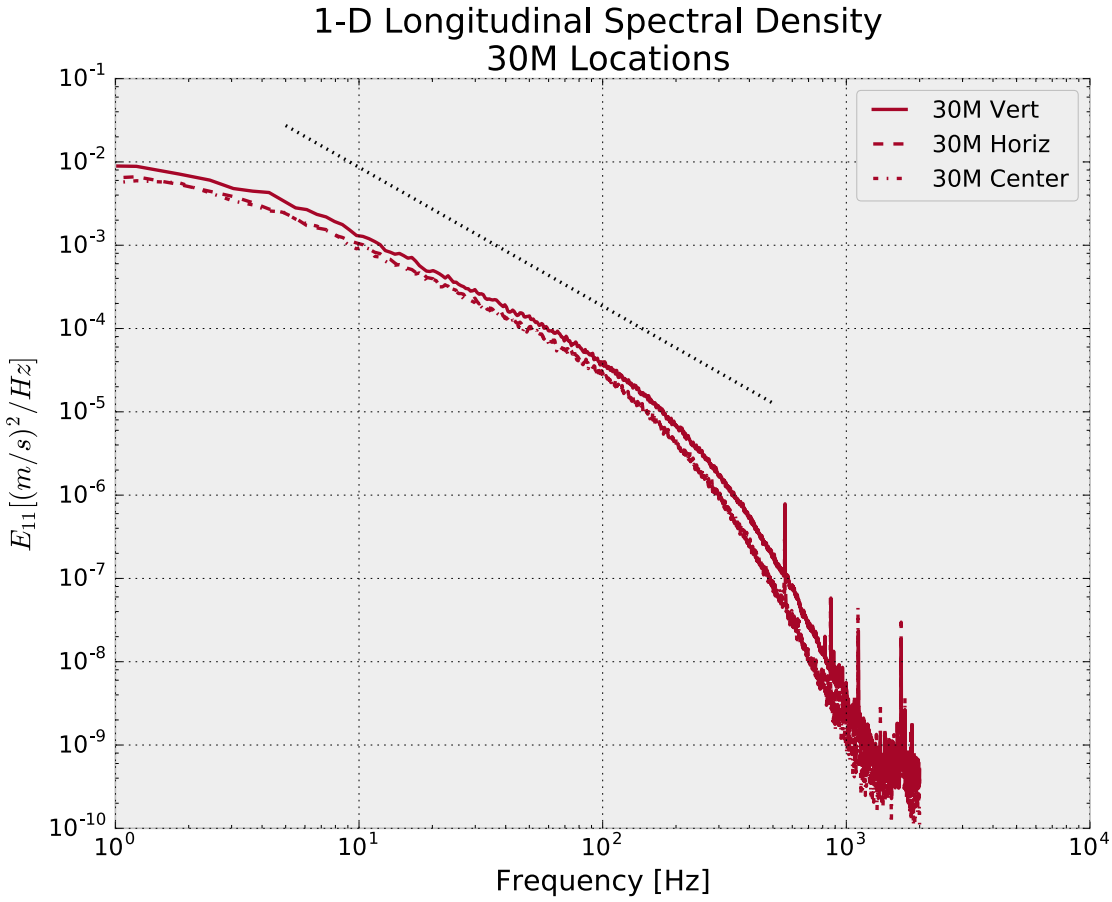

Figure 2.11: 1-D Longitudinal Spectral Density - Station 30M Measurement Locations. A plot of the turbulent energy spectrum from hotwire measurements made at the tunnel centerline, as well as the measurement locations of the vertical and horizontal high-speed imaging planes at Station 30M. The dashed line, with a -5/3 slope, is included as a visual reference for the slope predicted by Kolmogorov's theory for the inertial range of turbulent energy spectra.

conditions inside the wind tunnel. These include the RMS of the velocity fluctuations (u'); the turbulent dissipation rate (ε); the Kolmogorov length (η_κ), time (τ_κ), and velocity (u_κ) scales; the Taylor microscale (λ); and the Reynolds number based on the Taylor microscale (Re_λ).

Taking the integral of the energy spectrum, an approximate value for the turbulent kinetic energy dissipation rate (ε) was calculated.

$$\varepsilon = 15\,\nu \int_0^\infty k^2 E_{11}(k)\,dk \tag{2.1}$$

This estimate of the dissipation rate is limited in its accuracy by the lack of detailed information about the smallest scales in the turbulent kinetic energy spectrum. For this reason, the Taylor microscale λ (used to characterize the turbulence through the Reynolds number Re_λ) was computed from a correlation that uses the integral length scale L_{11} (Eq. 2.2) rather than the value of the turbulent dissipation rate.

$$\lambda/L_{11} = \sqrt{10/\mathrm{Re}_L} \tag{2.2}$$

From the dissipation rate, the rest of the Kolmogorov microscales (Equations 2.3, 2.4, and 2.5) are calculated as follows:

$$\eta = \left(\nu^3/\varepsilon\right)^{1/4} \tag{2.3}$$

$$\tau_\kappa = \left(\nu/\varepsilon\right)^{1/2} \tag{2.4}$$

$$u_\kappa = \left(\nu\varepsilon\right)^{1/4} \tag{2.5}$$

An analysis of the sources of error in the HWA measurements can be found in the Appendix.

2.3 Disperse Phase

2.3.1 Droplet Delivery System

The droplet delivery system (Figure 2.12), consisting of separate air and water pressure manifolds that supply the two-fluid atomizers embedded in the turbulence-inducing grid,

Table 2.3: Relevant flow parameters and scales describing the conditions inside the wind tunnel: the turbulent dissipation rate (ε); the Kolmogorov length (η_κ), time (τ_κ), and velocity (u_κ) scales; the Taylor microscale (λ); and the Reynolds number based on the Taylor microscale (Re_λ).

Station	U (m/s)	u' (m/s)	U/u'	ε (m^2/s^3)	η_κ (μm)	τ_κ (ms)	u_κ (m/s)	λ (mm)	Re_λ
20M	2.88	0.30	0.105	0.221	352	8.2	0.043	17.5	353
25M	2.87	0.25	0.086	0.123	407	11.1	0.037	21.3	350
30M	2.85	0.21	0.074	0.077	457	13.9	0.033	24.8	348
35M	2.87	0.19	0.065	0.053	503	16.9	0.030	28.3	353
40M	2.89	0.17	0.060	0.038	546	19.9	0.027	32.1	373

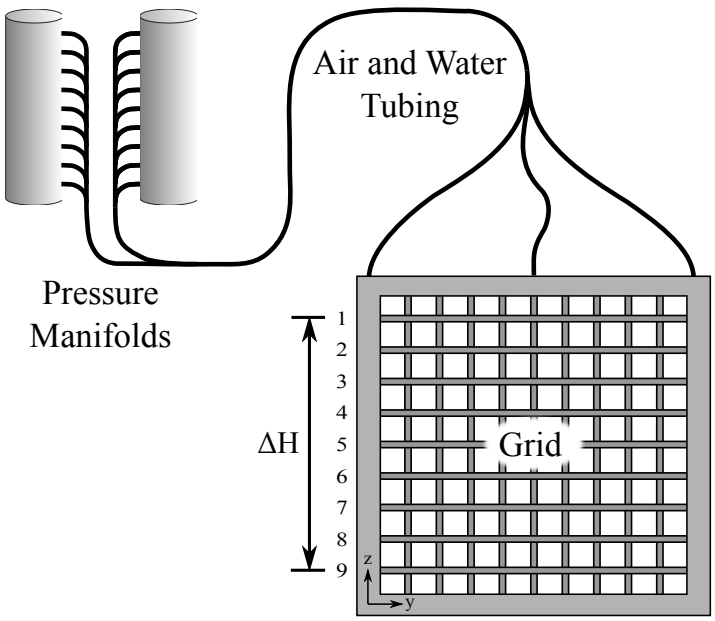

Figure 2.12: The droplet delivery system. An illustration showing how the separate air and water pressure manifolds supply the atomizers embedded in the grid. The height difference (ΔH) between each row of atomizers creates a hydrostatic pressure head for which the manifolds have been designed to compensate. Reproduced from Bateson and Aliseda (2012) with permission from Springer.

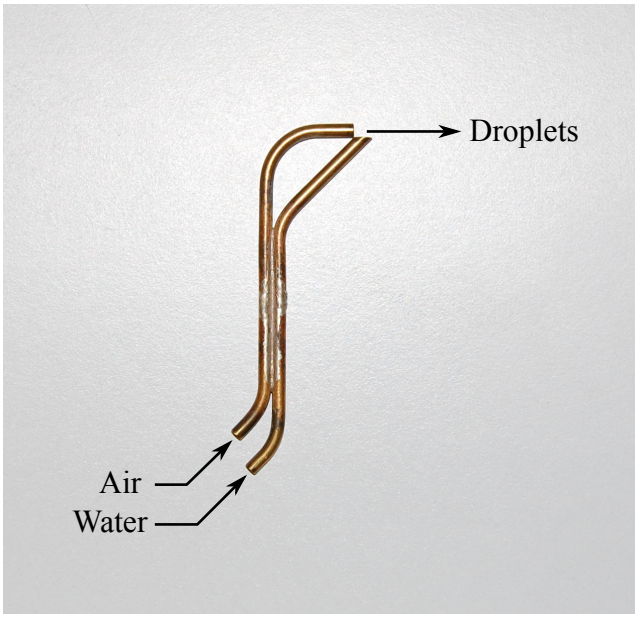

Figure 2.13: Two-fluid atomizer. Also referred to as injectors, the atomizers are used to create droplets in the wind tunnel.

fills the wind tunnel test section with water droplets that resemble those found in warm-rain clouds at the onset of precipitation. At each droplet atomizer, the high-momentum air jet impinges on the low-momentum water jet at a large angle, atomizing the liquid and producing a very dense spray of small droplets ($d = 5 - 150\,\mu$m). The grid was designed to equally distribute eighty-one identical atomizers across the cross-section of the wind tunnel. The atomizers were installed in the grid so that the air jets exit parallel to the mean flow in the wind tunnel (See Figures 2.13 and 2.14).

Droplet size distribution and liquid mass fraction of a two-fluid air-blast atomizer can be controlled by the air supply pressure and the water flow rate, as shown by Lázaro and Lasheras (1992). First, the water and air are fed into pressure manifolds to ensure equal pressures (and volumetric flow rates) at each of the eighty-one injectors. Then, polyurethane tubes run from the manifolds, through holes in the top of the wind tunnel, and down inside

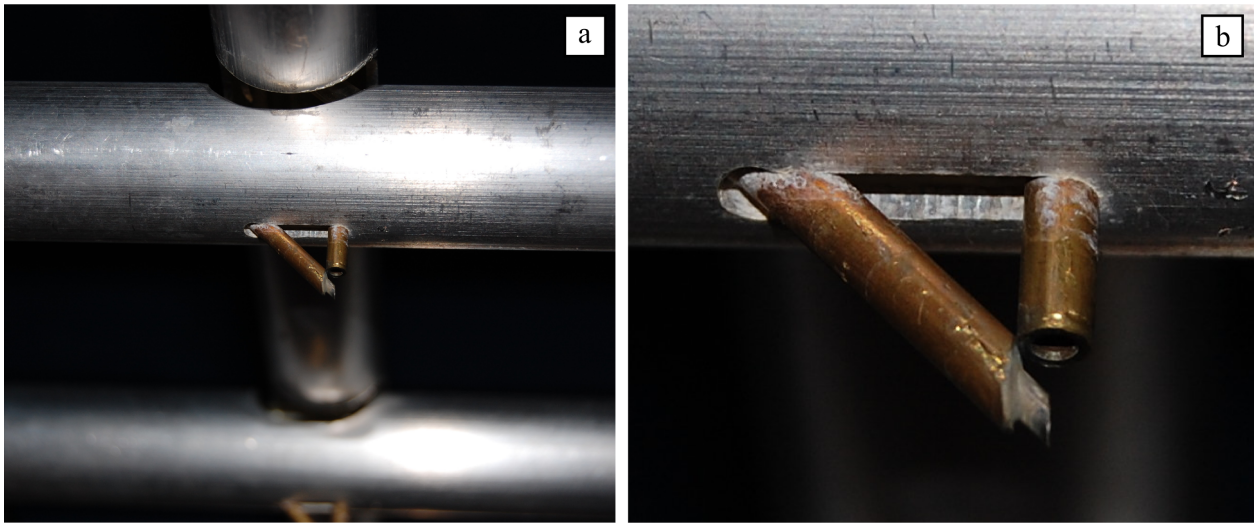

Figure 2.14: Two-fluid atomizers, as installed. Two photos of one of the two-fluid atomizing droplet injectors. (a) One of the grid's eighty-one droplet injectors that are integrated into the intersections of the grid tubes. (b) A close up of the atomizer integrated into the grid.

the tubes of the grid where they are attached to the injectors. All the atomizers are connected to the manifolds with equal lengths of tubing to ensure the same pressure loss between each atomizer and each manifold.

Due to the weight of the water column, the height difference between the tops and bottoms of the feeding manifold and injector grid (ΔH) creates a non-negligible hydrostatic pressure head between the different injector rows. This is a problem, because in order to create a homogeneous spatial distribution of droplets in the tunnel, the flow rate to every injector must be equal. To solve this problem, short lengths of stainless steel microtubing were installed in the manifold outlets. These microtubes alter the pressure drop across the outlets to compensate for that hydrostatic pressure difference (Figure 2.15). A detailed description of the process used to determine the exact dimensions of the microtubes can be found in (Bateson, 2010). As installed, the microtubes equalize the water pressure exiting the manifold so that the same flow rate of water reaches every atomizer regardless of its position

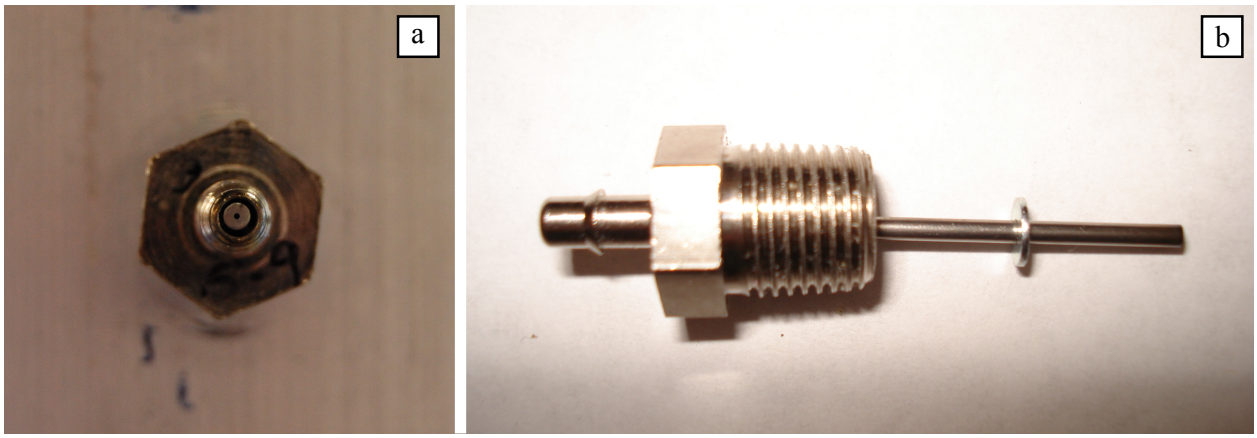

Figure 2.15: Pressure manifold outlet microtubing. Two photos of one of the pressure manifold tube fittings that serve as the outlets to the water manifold. (a) End view of a fitting installed in the manifold. This view shows the small inner diameter of the microtubes. (b) Side view of a fitting just after gluing in a microtube.

or its height in the grid. For the preliminary characterization of the experiment, a volumetric flow rate of 3 LPM of water was used. This flow rate was selected as the result of a trade-off between two competing factors that affected PDPA data collection: (1) Increasing the liquid water content increases collisions and preferential concentration; (2) The higher the volume fraction of water droplets, the faster the droplets deposit on the walls of the test section where they scatter the laser light passing into the tunnel and adversely affect the PDPA measurements. Ultimately, 3 LPM maximized the PDPA data rate during experiments and represented a high volume fraction of water in the flow without jeopardizing the quality of the measurements or the length of the time series necessary to obtain fully-converged statistical turbulent variables.

At 3 LPM of water and a wind tunnel flow rate of approximately 3.2 $^{m^3}/_{s}$, a volume fraction (ϕ_V) of 1.5×10^{-5} is produced in the tunnel test section, which is equivalent to a Liquid Water Content (LWC) of 15 $^{g}/_{m^3}$. While this value is an order of magnitude higher than typical for cumulonimbus clouds, the resulting mass loading and volume fraction of

Table 2.4: Fluid flow rates to the grid atomizers and the wall jets

Setting	Value
Atomizer Air Flow Rate	37.75 SCFM @ 80 psig
Atomizer Water Flow Rate	37 mL/min per atomizer
Wall Jet Air Flow Rate	475 LPM @ 45 psig

water are low enough to assume that no turbulence modulation by two-way coupling occurs. Therefore, the analysis of the data and its implications for the behavior of inertial droplets in turbulence are applicable to cloud processes. The high LWC conditions allow for building well-converged statistics of turbulence-induced droplet dynamics. They also facilitate the experimental characterization of collision processes by increasing the probability of collisions during the short time the droplets have to interact inside the wind tunnel.

2.3.2 Characterization of the Disperse Phase

Phase Doppler Particle Analysis (PDPA)

Phase Doppler Particle Analysis (TSI Inc., Shoreview, MN.) is a non-intrusive, light interferometry system used for measuring the motion of particles (solid particles, liquid droplets, or gas bubbles) immersed in fluid flows. A pair of laser beams, shifted in frequency (40 MHz) from each other by a Bragg Cell, are focused at a small incidence angle on a specific point (the probe volume) inside the particle-laden flow. Measurements of the velocity and diameter of the particles are made by analyzing the frequency and phase shift, respectively, of the light scattered by these particles. Long time series of these measurements are used to calculate statistics of the liquid droplet distributions. Details of PDPA measurement theory and operation can be found in Bachalo (1994); Albrecht (2003). For the results presented in

this dissertation, data was collected using the PDPA optical and operational settings listed in Table 2.5. PDPA measurements were made at five different locations—or *stations*—along the first tunnel test section: $x/\mathrm{M} = 6.4$, 14, 17, 22, 29. At each station, measurements were made at the same position relative to the height (H) of the wind tunnel's square cross section (See Figure 2.16).

The presence of the wind tunnel walls presents challenges in the collection of large data sets of PDPA measurements under the relatively high volume fraction of droplets and high turbulence intensities of these experiments. Water droplets collecting on the inside of the test section walls scatter the laser light, both coming from the transmitter into the probe volume and, more importantly, leaving the probe volume after being refracted by the droplets crossing it. This creates the potential for the measurements to miss the signal from some droplets crossing the probe volume, and this data loss would be biased against the smallest droplets that produce a weaker signal (the droplets scatter a fraction of the incident light proportional to the diameter squared, $I/I_0 \propto d^2$). To minimize this effect, an auxiliary air flow system (*air curtain*) was designed and manufactured, consisting of a flat, fan shaped nozzle attached to the inside of the test section walls using suction cups, and supplied with high pressure air via a tube that runs along the inside corner of the tunnel. The air exits the nozzle and creates a thin curtain of air along the wall that the water droplets in the core of the wind tunnel cannot cross. This *air curtain* inhibits the deposition of drops on the tunnel wall in a small region about $1/2$ inch in diameter. This area is just large enough to allow the light to propagate through the walls in and out of the test section without significant attenuation.

After the installation of the new tunnel test section, water accumulation on the tunnel walls was avoided by shutting off the water to the atomizers closest to the walls and adjusting the water flow rate to the grid proportionately to the number of active atomizers. Due in part to the wall jets and their effect on the tunnel velocity profile, simply turning off the

Table 2.5: PDPA operational settings.

Setting	Value
PMT Voltage	500–600 V
Burst Threshold	30 mV
Bandpass Filter	0.1–1 MHz
Signal to Noise Ratio (SNR)	High
Downmix Frequency	39.5 MHz
Laser Power	1–1.5 W
Beam Expander Ratio	0.5
Transmitter Focal Length	250 mm
Transmitter Beam Width	0.885 mm
Transmitter Beam Separation	10 mm
Fringe Spacing	12.865 μm
Measurement Volume Dimensions	0.19 x 0.19 x 0.19 mm
Receiver Slit Aperature	150 μm
Sample Size (each location)	75,000 drops
Range of Measurable Diameters	1.47–590.07 μm
Intensity Validation	None

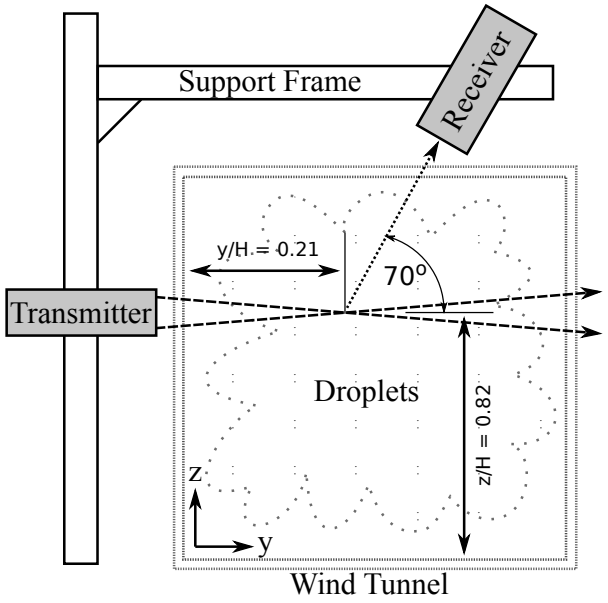

Figure 2.16: PDPA orientation with respect to the wind tunnel. An illustration of the PDPA system showing the relationship between the receiver and the transmitter and their orientation to the wind tunnel. The laser beams leaving the transmitter are represented by dashed lines, and their intersection locates the measurement volume. The dotted line is the light scattered by the droplets that pass through the measurement volume. Measurements were made at the same position relative to the height (H) of the wind tunnel's square cross section ($y/H = 0.21$, $z/H = 0.82$). Adapted from Bateson and Aliseda (2012) with permission from Springer.

water to the atomizing nozzles nearest the walls completely solved the droplet deposition problem. All of the high-speed imaging was conducted in this configuration. To preserve the droplet diameter distributions and the local droplet volume fraction at the measurement locations, the water flow rate supplied to the grid was reduced proportionately to the number of fully active atomizers. For all of the experiments reported in this dissertation, each active atomizer received $3\,\mathrm{LPM} \div 81 = 37\,\mathrm{mL/min}$ of water.

The PDPA receiver was positioned at a 70° angle to the direction of light propagation from the transmitter to collect forward-scattered light in the first mode of diffraction, while

maximizing the range of measurement positions within the wind tunnel with a fixed focal lens (250 mm). This means that the receiver looks into the tunnel at an angle with respect to the tunnel wall (Figure 2.16), which introduces a problem with the refraction of light as it propagates through the acrylic wind tunnel walls. Two triangular acrylic prisms, with a matching 70° angle between their faces, were built and attached to both sides of the top test section wall, creating a rigid body whose surfaces are perpendicular to the receiver's lens, thus minimizing the effects of light refraction through the tunnel walls. One prism sits on top of the tunnel, and the other prism is suspended on the inside of the tunnel using magnets. A thin layer of glycerol, which has an index of refraction similar to acrylic, is used between the surfaces to minimize the light scattered at the interfaces between the prisms and the tunnel walls.

For the diameter measurements based on Mie scattering, the droplets are assumed to be spherical. The Weber number for the droplets, based on the droplet diameter and the turbulent velocity RMS, is on the order of 10^{-2}. Therefore any deformations resulting from unsteady pressure forces in the flow field are quickly dominated by the restoring effects of surface tension. For this reason, it is assumed that the droplets remain spherical throughout the experiments.

To recreate a physical environment similar to that of clouds, the experiments were designed to be in the same range of the relevant non-dimensional parameters that control droplet inertial dynamics: Stokes number, droplet terminal velocity ratio, turbulence dissipation rate, droplet volume fraction, and Re_λ. The dissipation rate (Table 2.3) and volume fraction in the experiments are higher than the values found in cumulus clouds. However, since these values are the same order of magnitude as the cloud parameters, the physics of inertial droplet interactions with turbulence observed are still applicable to cloud processes. The Reynolds numbers in clouds cannot be recreated in the laboratory, but the experiments in this dissertation are at a high enough value ($\mathrm{Re}_\lambda \approx 350$) that the results are characteristic

of a very high Reynolds number flow in the asymptotic Re regime.

The first purpose of the turbulence-inducing droplet injection grid is to create homogeneous and isotropic turbulence inside the wind tunnel. The second purpose is to create a homogeneous distribution of micron-sized droplets. The homogeneity of the droplet size and spatial distribution is primarily determined by the atomization conditions at the grid. After the droplets are introduced into the tunnel air flow, their distribution will quickly be modified by their interactions with the turbulence. To avoid introducing an unwanted source of inhomogeneity into the experiment, it is important that the initial droplet dispersion is homogeneous.

As mentioned previously, the water manifold's tube fittings were retrofitted in order to equalize the pressure head available to each atomizer. The manifold design aimed to provide a homogeneous flow rate of water to each atomizer, with a maximum difference of 5%. However, there are multiple sources of uncertainty in the physical implementation of the manifold and water distribution system that could increase the inhomogeneity in water flow rates to the atomizers beyond the theoretical prediction of 5%. In order to quantify the grid's homogeneity, a simple experiment was conducted to measure the actual flow rate through each atomizer. In this experiment, the grid water supply was turned on while keeping the air supply off, so that no atomization occurred, and the mass of water coming out of each injector was collected for a constant interval of 10 seconds, weighing it with a high precision balance. This measurement was repeated three times to account for the variability in the collection system and the possible unsteadiness of the water injection system. The results are tabulated in Table 2.6.

For each atomizer, the data from the three experiments were averaged and the intra-measurement variability was found to be less than 19%. The average for all the injectors, 17.27 g, was 2% higher than the theoretical value of 16.98 g. This is a good estimate of the accuracy of the model for the pressure loss in the water supply system. The standard

Table 2.6: Statistics calculated for the grid flow rate homogeneity characterization measurements. The values quantify the variation across each row of atomizers in both grams, and the percentage of the row's mean. By design, the atomizers in each row should have identical flow rates. The maximum difference between the mean value of any two rows was 1.6 g (9% of the mean value for the entire grid).

	Mean	Std. Deviation		Max. Difference	
Row	(g)	(g)	(%)	(g)	(%)
1	16.81	0.70	4.2	2.13	12.7
2	16.57	0.91	5.5	3.08	18.6
3	16.57	0.86	5.2	2.67	16.1
4	17.14	0.87	5.1	2.71	15.8
5	17.43	0.43	2.5	1.27	7.3
6	17.29	1.02	5.9	3.68	21.3
7	17.75	0.64	3.6	1.85	10.4
8	17.73	0.89	5.0	2.87	16.2
9	18.15	1.04	5.7	3.34	18.4

deviation in the average values, computed for the entire grid, was 0.95 g or 6% of the mean, and the maximum deviation from the mean for a single injector was 2.14 g, or 12% of the mean. An equally distributed water supply does not guarantee homogeneous atomization. So, the PDPA measurement system was used to characterize the droplet diameter and velocity close to the air/water injectors. The PDPA was traversed vertically across the sprays at two locations downstream from the grid ($x/\mathrm{M} = 0.75$ and $x/\mathrm{M} = 3.75$). Figure 2.17 shows the mean droplet velocity profiles at the two x/M locations. The high velocity jets issuing from the injectors are visible at $x/\mathrm{M} = 0.75$, while at $x/\mathrm{M} = 3.75$ the velocity profiles are nearly uniform across both sprays showing the quick development of homogeneity. The same

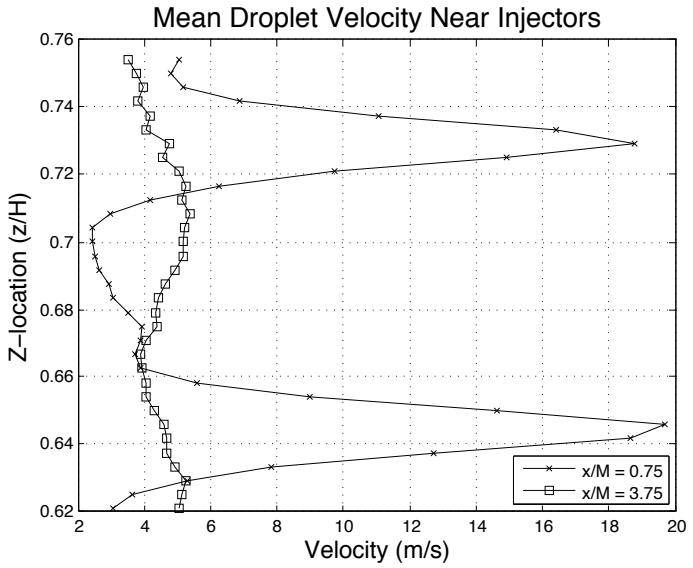

Figure 2.17: Mean droplet velocity near injectors. Vertical profiles of mean droplet velocity from PDPA measurements at $x = 0.75$M and $x = 3.75$M. Reproduced from Bateson and Aliseda (2012) with permission from Springer.

conclusion can be drawn from Figure 2.18. This plot of the mean droplet diameter shows very small droplets near the center of the jets in the $x/\mathrm{M} = 0.75$ profile due to the more efficient atomization created by the high jet velocity. At $x/\mathrm{M} = 3.75$ the mean diameter is nearly uniform across the profile. Figure 2.19 is a plot of all the droplet diameter PDFs calculated at each Z-location in the $x/\mathrm{M} = 3.75$ traverse. The similarity in each of the thirty-three PDFs shows that the entire size distribution of the droplets becomes homogeneous very quickly. All of the results in this dissertation were calculated from measurements made no closer than $x/\mathrm{M} = 20$.

Since the intent of the experiments in this dissertation is to relate our results to the evolution of cloud droplet size spectra, measurements were made to verify that the water droplets created had an appropriate size distribution by the time they reached the measurement locations. Figure 2.20 shows the typical Probability Density Function (PDF) of droplet diameter

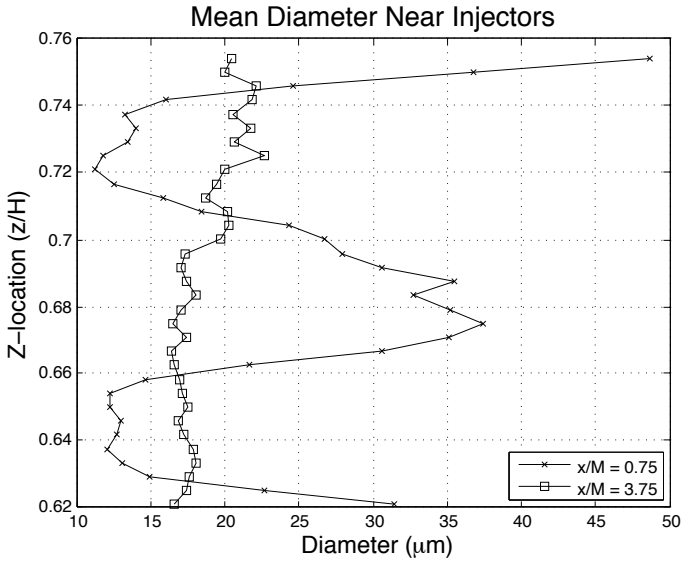

Figure 2.18: Mean diameter near injectors. Vertical profiles of mean droplet diameter from PDPA measurements at $x = 0.75$M and $x = 3.75$M. Reproduced from Bateson and Aliseda (2012) with permission from Springer.

at x=14M, which is just upstream from the first measurement location. The diameter PDF plot highlights the relative position within the distribution of the arithmetic mean diameter (D_{10}), the Sauter mean diameter (D_{32}) and the diameter corresponding to a droplet with a Stokes number[†] of 1.

Since the diameter corresponding to a droplet with a Stokes number of 1 is well within the range of the droplet sizes in the flow, it is clear that droplet inertia will be the key parameter that determines how the droplets will interact with the carrier flow turbulence. Therefore, the influence of turbulence and inertia on droplet collisions can be studied in this experiment. The typical value of the Kolmogorov length scale (η_κ) is 350–550 μm (See Table 2.3), which is much larger than the size of the droplets. The theoretical background used in this dissertation's analysis (Maxey and Riley, 1983) is justified by the limit $d/\eta \ll 1$.

[†]The Stokes number is defined in Section 1.2.1

Additionally, the Reynolds number for the droplets studied (based on diameter and droplet settling velocity) ranges from $\mathrm{Re} \ll 1$ to $\mathrm{Re} \approx 1$. Both the Reynolds number range and the small ratio between droplet size and Kolmogorov length scale support the formulation of the Stokes number in terms of the Kolmogorov time scale and the particle relaxation time based on Stokes flow.

In clouds, droplet size spectra exhibit wide variations due to the large range of conditions that occur in nature. It is worthwhile to note that the size distribution in these experiments exhibits the important general characteristics of the spectrum of a nearly precipitating cloud. The majority of the droplets have diameters under 30 microns, which is comparable to cloud droplets. A second characteristic that the droplet diameter spectrum shares with cloud droplet size spectra is a narrow distribution centered around $20\,\mu$m that, in clouds, is the result of the cloud droplets' condensational growth mechanism. Additionally, the tail in the experimental spectrum has large diameter droplets that correspond to the few collector drops that are necessary for rain formation. This tail in the spectrum allows for the simultaneous study of collisions between cloud droplets ($< 60\,\mu$m) as well as between collector-sized drops ($> 100\,\mu$m) and cloud droplets within the same experiment.

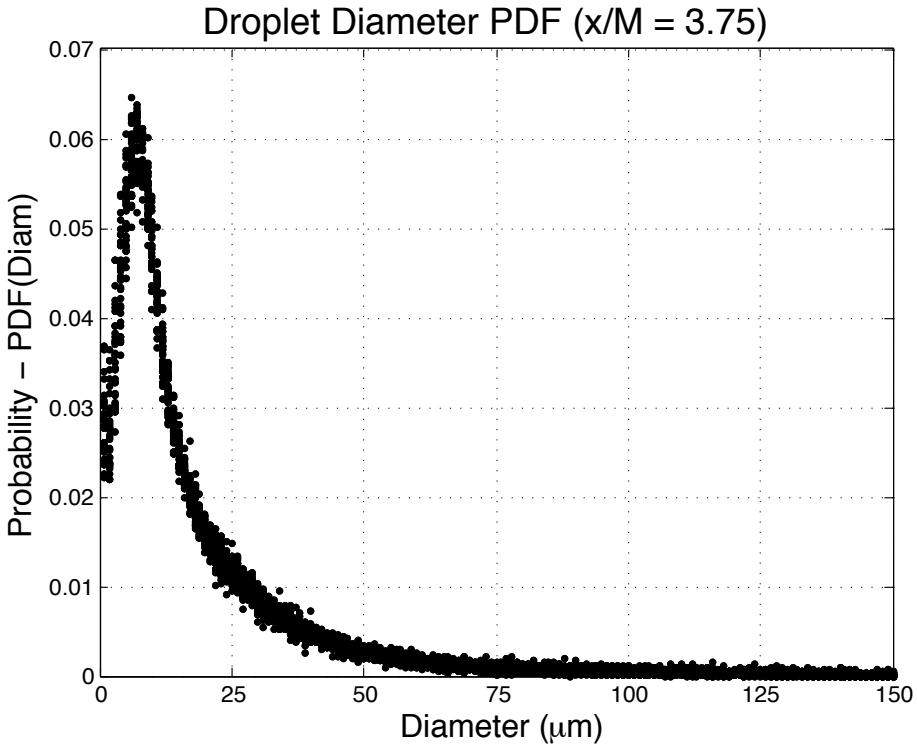

Figure 2.19: Droplet diameter PDF ($x = 3.75$M). The superposition of the droplet diameter PDFs calculated at each of the thirty-three PDPA measurement locations in the vertical traverse at $x = 3.75$M. Reproduced from Bateson and Aliseda (2012) with permission from Springer.

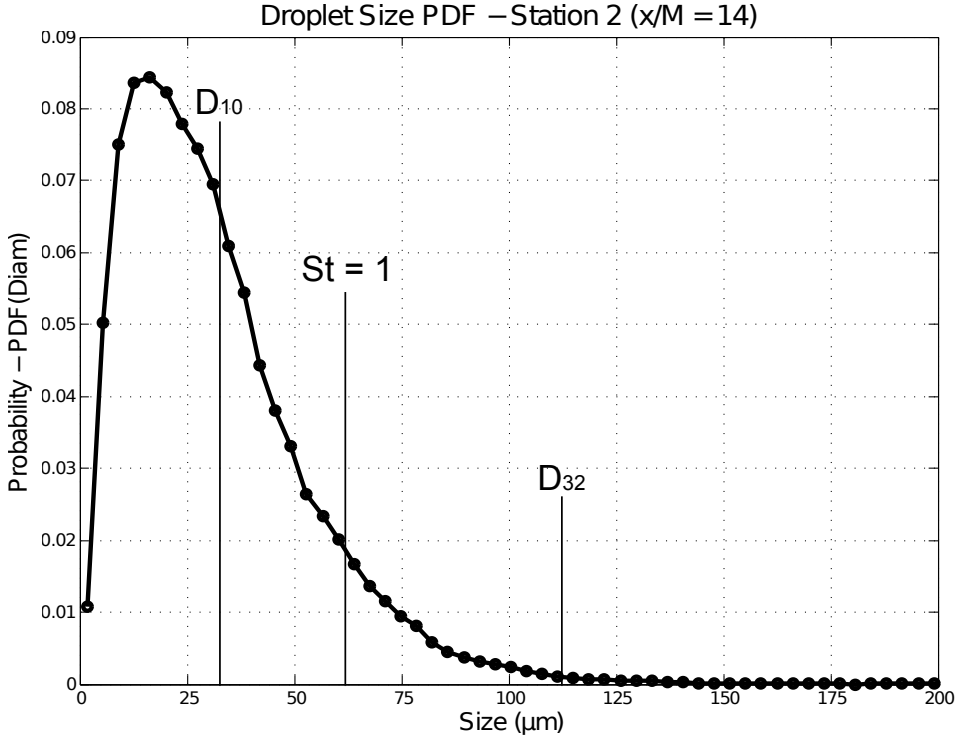

Figure 2.20: Probability distribution of droplet diameters measured with the PDPA at Station 2 ($x/\mathrm{M} = 14$, $y/H = 0.21$, $z/H = 0.82$). From left to right, the black vertical lines corresponds to the arithmetic mean diameter (D_{10}), the diameter of a droplet with a Stokes number equal to 1, and the Sauter mean diameter (D_{32}). Reproduced from Bateson and Aliseda (2012) with permission from Springer.

Chapter 3

MEASUREMENTS AND METHODS: PARTICLE TRACKING VELOCIMETRY (PTV)

In order to investigate the relationship between turbulence and inertial droplet dynamics in the wind tunnel, high-speed camera images and Particle Tracking Velocimetry (PTV) are used to measure droplet velocities and spatial distributions in two dimensions. Using a light source to illuminate a thin plane in a fluid flow seeded with particles and a high-speed camera to record the motion of the particles as they pass through the plane, PTV identifies and tracks individual particle positions through consecutive images to determine their trajectories. PTV measurements of droplet velocities and accelerations are made at multiple locations along the length of the tunnel in order to examine the influence of turbulent dissipation rate on droplet dynamics. At each of these measurement stations, data are collected using both horizontal and vertical imaging planes to capture the influence of gravity. The high-speed movies are processed using a home-made custom PTV code that connects the positions of a given droplet together into a track based on its most probable trajectory through multiple images. PTV results are post-processed by fitting a univariate cubic spline to the droplet coordinates in each track. The splines allow for the calculation of smooth derivatives of the droplet trajectories. After filtering the resulting velocities and accelerations to remove non-physical and noisy results, the data collected under a given set of turbulence conditions are ready for further processing to calculate descriptive statistics of the droplet dynamics.

3.1 Droplet Illumination

The droplets in the tunnel test section are illuminated using an argon-ion continuous laser. A 1.5 W laser beam is directed through a series of mirrors and lenses to create a planar laser sheet. The laser sheet is generated using two lenses: a 50.2 mm focal length spherical convex lens followed by a 38.1 mm cylindrical flat-convex lens. Figure 3.1 shows the lens arrangement and nominal spacing. The lenses are positioned relative to each other so that the resulting laser sheet slowly converges to a focal line. Making fine adjustments to the lens positions, the focal line is located just beyond the measurement region to keep the laser sheet as thin as possible. The measurements reported here were made with a laser sheet approximately 8 mm wide $\times$ 1 mm thick at the measurement location.

3.2 High-speed Camera

High-speed images of the water droplets are made with a Vision Research Phantom v12.1 camera, a Zeiss 100 mm lens and a 2x Teleconverter attachment to increase the magnification and improve the resolution of the droplet positions. The camera is mounted onto a 2-axis traverse. To preserve the same optical settings (aperture and focal plane) for the camera lens throughout all our experiments, the lens is set to the smallest f-stop and the high-precision movement of the traverse is used to focus the camera rather than the camera lens. The camera frame rate and exposure settings are selected based on a trade off between droplet illumination, resolution of droplet motion, and camera memory. With the camera settings listed in Table 3.1 and with typical wind tunnel settings, a droplet moves approximately 1.5 pixels during a 20 μs exposure and 30 pixels between frames.

3.3 PTV Measurement Locations

PTV measurements are collected at three different stations along the length of the tunnel: 20M, 30M, and 40M. At these three stations, high-speed movies are made in vertical and

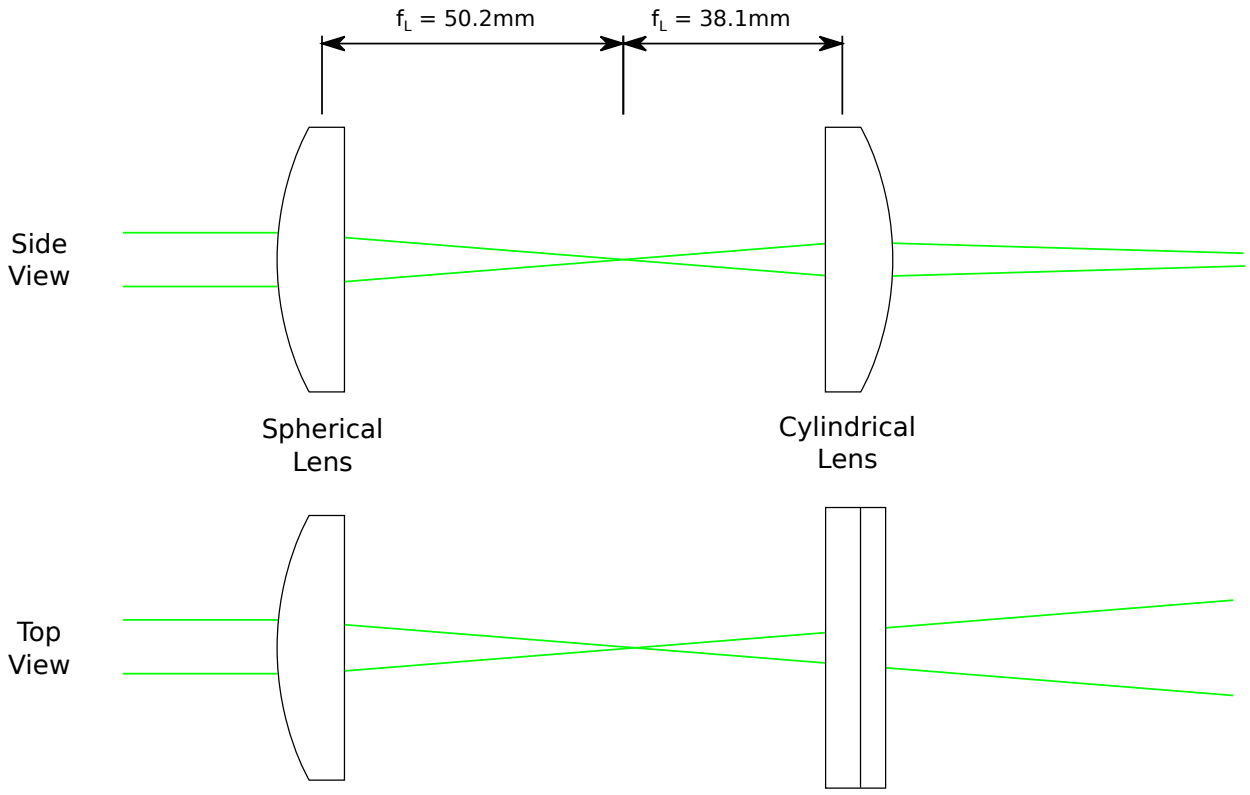

Figure 3.1: PTV lens configuration. An illustration of the lens configuration used to generate the laser sheet that illuminates the droplets for high-speed imaging and particle tracking velocimetry. The spherical lens has a focal length of 50.2 mm and the cylindrical lens has a focal length of 38.1 mm.

Table 3.1: Information about the camera, lens and the operational settings used to make high-speed images.

Description	Value
Camera:	Vision Research Phantom v12.1
Lens:	Zeiss 100 mm
f-stop:	$f/2$
Frames/second:	5000
Camera Exposure:	20 μs
Image Resolution:	1280×800 pixels
Frames/movie:	5270

horizontal orientations. Four movies at each of the three stations are made using the horizontal laser sheets. For the vertical laser sheet orientation, the count is increased to ten movies at each station for better statistical convergence of the particle concentration field, as well as the relative and settling velocities conditioned on the local concentration. Figure 3.2 shows the exact measurement locations with respect to the wind tunnel walls. The maximum magnification of the high-speed images coincides with the shortest distance to the lens' focal plane. This presented a trade off between high resolution images that allow for more accurate measurements of droplet positions at the expense of being able to make measurements at the center of the tunnel. The maximum magnification of the lens is used even though this means that the focusing plane (measurement location) has to be away from the center of the wind tunnel and relatively close to the wind tunnel walls. The resulting imaging locations are far enough from the tunnel walls to be in the homogeneous core of the flow, as shown in Figure 3.2.

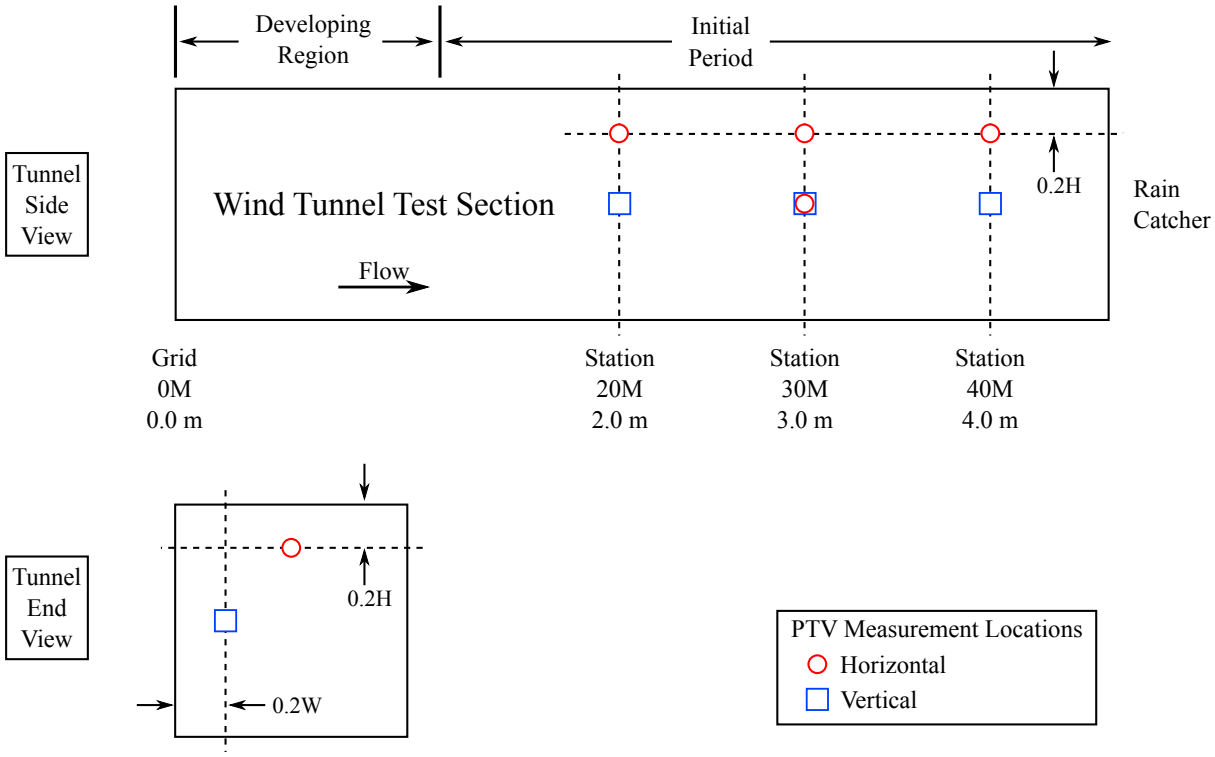

Figure 3.2: Particle tracking velocimetry measurement locations shown relative to the test section geometry.

3.4 Image Processing

ImageJ, an open-source image processing program created by the National Institutes of Health (NIH), was used to measure droplet positions and geometry from the individual images in the high-speed movies. During the initial processing, it was noticed that the camera sensor has a bias that results in higher numbers of droplets being detected in some regions than others. This bias can be seen in Figure 3.3, which is a 2D histogram of all droplet coordinates for a single movie. The histograms for all of the movies have the same feature and the coherent shape of this bias is independent of measurement station, laser plane orientation and laser intensity, but is dependent on camera orientation. This led to the conclusion that the source of the bias is the camera sensor's non-uniform sensitivity. To avoid the possibility that this bias affected any of the spatially dependent statistics (e.g. RDF), the raw images are corrected using a technique proposed in Tropea et al. (2007). In the case of uneven illumination or uneven sensitivity, images can be corrected using the following equation:

$$\mathbf{G}' = c\,\frac{\mathbf{G}-\mathbf{B}}{\mathbf{R}-\mathbf{B}} \tag{3.1}$$

where $\mathbf{G}'$ is a 2D array of corrected pixel intensities, $\mathbf{G}$ is the original image, $\mathbf{B}$ is a black reference image created with a covered lens to measure the sensor's response to zero illumination, $\mathbf{R}$ is a white reference image created with a constant illumination source, and c is an arbitrary proportionality factor used to readjust the pixel intensity values to an appropriate 16-bit range.

Equation (3.1) works by rescaling each individual pixel intensity based on the dynamic range measured for that pixel. The dynamic range is determined by subtracting the background noise resulting from the fact that the pixels have non-zero intensities even when there is no source of illumination (this is the black reference image – $\mathbf{B}$) from the response of all the pixels to a uniform illumination source (this is the white reference image – $\mathbf{R}$).

Lacking a uniform illumination source of the size and intensity needed for this calibration,

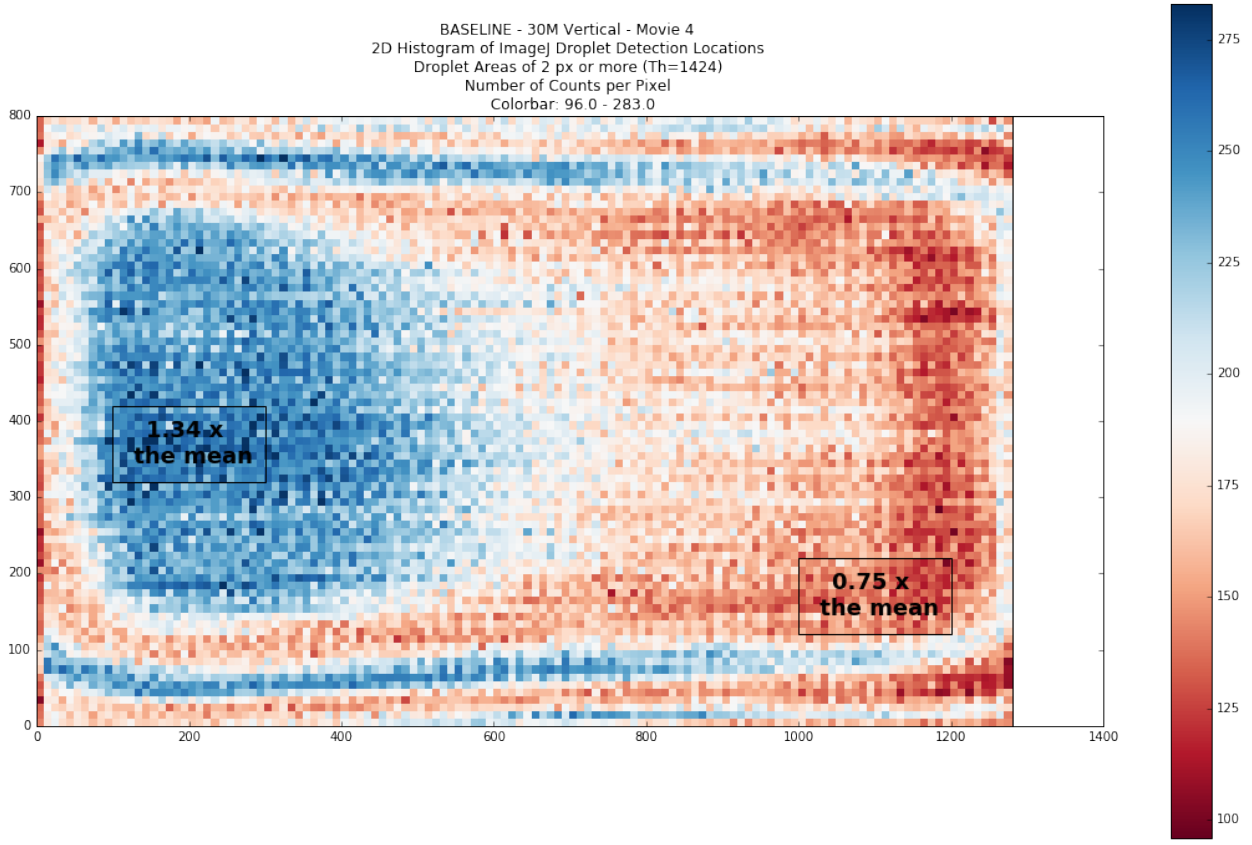

Figure 3.3: 2D histogram of droplet detection counts as a function of X- and Y-coordinates. This plot shows the baseline spatial distribution of droplet detection positions prior to any correction. The histogram bins are 10×10 pixels square. The color bar represents counts per bin and is centered (white color) about the mean value. The two boxes inside the plot show the average value of the counts inside the box relative to the overall mean for the entire area (800×1280 pixels).

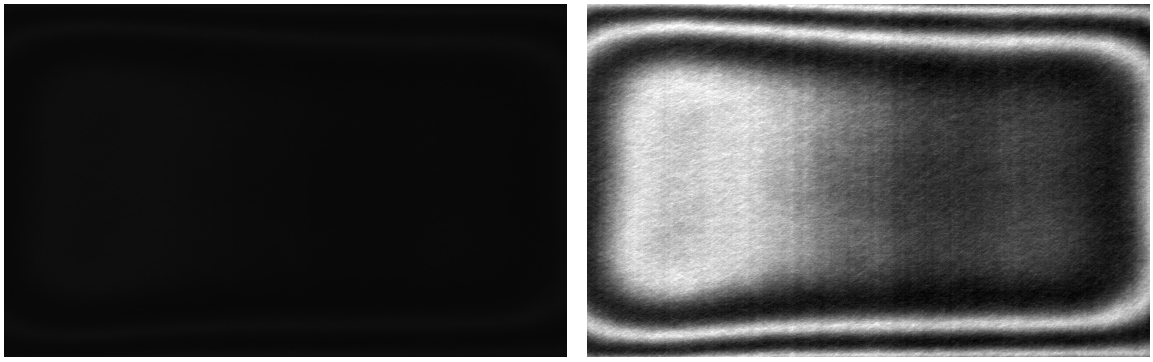

(a) Raw image. (b) High contrast image.

Figure 3.4: White reference image (**R**) used for image intensity corrections. (a) shows the raw 16-bit image intensity. (b) uses high contrast to display the coherent shape of the intensity bias.

a white reference was created by imaging a very dense cloud of droplets created inside the tunnel. Using a long exposure setting on the camera and then averaging all the frames in the movie, the image created is a good approximation to a constant illumination source (Figure 3.4).

As for the black reference image, ideally this would be created immediately before or after making a movie. This is especially critical with our Phantom v12 camera since the camera sensor noise is known to be highly dependent on time and camera operational settings. Since black reference images were never created during the process of making the movies, the black reference images were approximated by measuring the noise directly from the movies themselves. Attempts to reproduce black reference images did not result in successful image corrections.

To automate the application of Eq. (3.1) to the high-speed droplet visualization images, the correction equation was rearranged into the following form:

$$\mathbf{G}' = CF(\mathbf{G} - \mathbf{B}) \tag{3.2}$$

where CF is a Correction Factor constant for each movie and defined as

$$CF = \frac{c}{\mathbf{R} - \mathbf{B}}. \tag{3.3}$$

After creating the white reference image, the post-processing undergone by the high-speed movies is described in the next section.

3.4.1 Steps Used to Determine Droplet Coordinates and Geometry

1. Calculate and remove background noise from the images. $\mathbf{G} - \mathbf{B}$

   A built-in ImageJ function is used to add all the movie images together, summing up the individual pixel intensities and then returning an image where each pixel has an intensity value equal to its average intensity across all the images in the movie. This image is an approximation of the background noise that is used in place of the black reference image ($\mathbf{B}$) from Eq. (3.1). The background noise is then subtracted from all the images in the movie. The image subtraction process rounds to zero any pixel for which it results in a negative intensity. The average background intensity values are a very small fraction of the intensity of an illuminated droplet, so the detection of real droplets is not adversely affected by the background subtraction.

2. Apply Correction Factor (CF).

   Using a python script written to automate the process, the images for a single movie are loaded into memory and the image intensity values are multiplied by the correction factor calculated for that particular movie.

3. Determine the movie's intensity threshold value from a subset of the images in the movie.

   Every 100^{th} image is opened up in ImageJ and the minimum threshold value is adjusted until all residual image noise disappears. The minimum threshold value varies across

images and over the length of a movie, so to be conservative, a threshold value that eliminated noise in all the images in the subset was chosen.

4. Apply the final threshold value to all the images in the movie.

   The threshold value determined in the previous step is then applied to the entire movie. The resulting images have grey-scale illuminated droplets on a pure black background.

5. Run ImageJ's *Analyze Particles* routine to determine droplet coordinates and geometry.

ImageJ produces a large data file containing the image number, X- and Y-coordinates, intensity values, and geometric shape measurements for each and every "particle" in the movie. To show the efficacy of the correction factor technique, a 2D histogram of all the droplet coordinates was plotted again for the same movie, although this time they were determined from the *intensity-corrected* images.

3.5 A New 4-frame N+2 PTV Algorithm

The particle tracking velocimetry (PTV) code used for this research is based on the method published by Ouellette et al. (2006), referred to as a 4-frame Best Estimated Position Tracking Algorithm. The algorithm uses a droplet's position in three previous images to calculate an acceleration. The droplet's position in the next image is determined by finding the droplet whose position minimizes the change in acceleration along the trajectory. Building on Ouellette et al.'s ideas, but allowing for multiple options in the second and third images to compute velocities and accelerations, a routine was implemented that chooses the most likely next position of a droplet in a trajectory by evaluating all possible trajectories two images ($N + 2$) into the future.

This new PTV code uses the data generated by ImageJ, eliminating all the droplets with areas less than two pixels. It was found that most of the fictitious droplets resulting

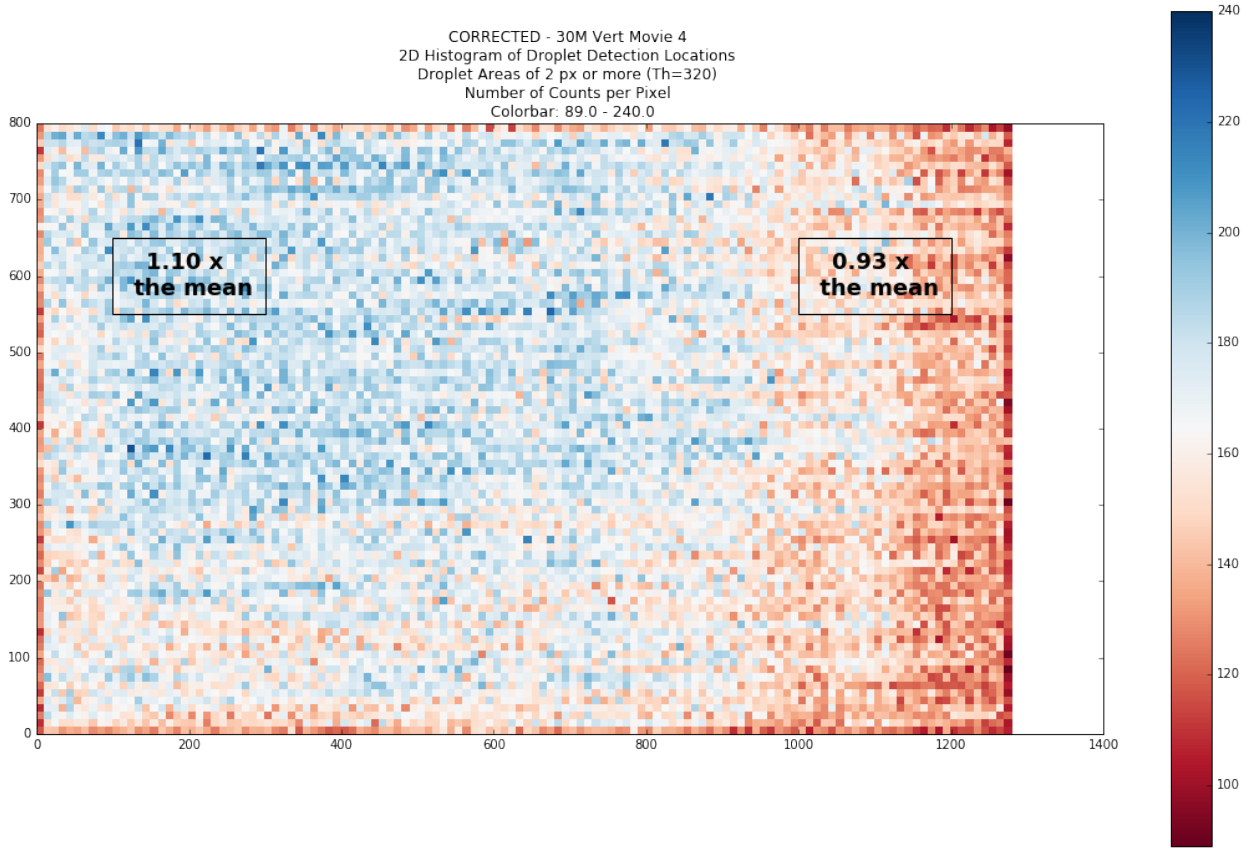

Figure 3.5: 2D histogram of droplets detection counts as a function of X- and Y-coordinates. This plot shows the spatial distribution of droplet detection positions after the images have been corrected for intensity or sensor sensitivity to remove the camera sensor's bias. The histogram bins are 10×10 pixels square. The color bar represents counts per bin and is centered (white) about the mean value. The two boxes inside the plot show the average value of the counts inside the box relative to the overall mean for the entire area (800×1280 pixels).

from noise in the images had areas equal to one pixel. Consistent with this observation, even the smallest droplets in the images should move at least 1.5 pixels during the camera's exposure time. For these reasons, the algorithm eliminates all droplets with areas less than two pixels before matching the positions to tracks, greatly reducing the computational effort and uncertainty in the track assignation.

To describe how the PTV code works, the process used to determine the trajectory for a single droplet across multiple images will be described in detail. This process is used recursively for all droplets that have not yet been matched to a track. The PTV code vectorizes this process to determine trajectories for all the droplets in an image.

For this description, N is the number of the current image. An arbitrary droplet i in image N has position X_i^N. That same droplet in image $N-1$ has a known position X_i^{N-1}, but in image $N+1$ in the "future," the droplet has an expected position $\tilde{X}_i^{N+1}$. An array of the positions for multiple potential matches, called candidate droplets, is denoted using bold typeface: $\mathbf{X}_j^{N+1}$. The time between frames is Δt and is equal to the inverse of the camera frame rate. In this analysis, $(5000\,\text{frames/sec})^{-1} = 20\,\mu\text{s}$.

3.5.1 PTV Processing Steps

1. Calculate a predicted position in image $N+1$.

   (a) If droplet i is not currently part of a trajectory, a new trajectory is started and the droplet's expected position in image $N+1$ is calculated using a velocity prediction*.

   $$\tilde{X}_i^{N+1} = X_i^N + U_{avg}\,\Delta t \tag{3.4}$$

   (b) If droplet i is in a trajectory and its position is known back through image $N-1$,

*The mean velocity of the droplets (the streamwise velocity in the wind tunnel) was used in all velocity predictions. The first time through the code, the mean velocity is approximated by the mean carrier fluid velocity measured with the Pitot rake. Subsequent runs use the mean velocity from the most recent set of PTV results.

its expected position in image N+1 is calculated assuming the droplet moves with constant velocity.

$$\tilde{X}_i^{N+1} = 2X_i^N - X_i^{N-1} \tag{3.5}$$

(c) If droplet i is in a trajectory and its position is known back through at least image N–2, its expected position in image N+1 is calculated assuming the droplet moves with constant acceleration.

$$\tilde{X}_i^{N+1} = 2.5X_i^N - 2X_i^{N-1} + 0.5X_i^{N-2} \tag{3.6}$$

2. Once an expected position has been calculated for image N+1, find all the droplets in image N+1 that are within a radial distance equal to Δt times a predefined number of standard deviations of the droplet velocity fluctuations.

   For the results presented here, the search area was defined using five standard deviations of the velocity fluctuations. All the droplets within the search area are considered candidate droplets ($\mathbf{X}_j^{N+1}$).

3. Calculate an array of multiple expected positions in image N+2 using all the possible trajectories that pass through the candidate droplets' coordinates.

   (a) If droplet i was not previously part of a trajectory, its expected position is calculated assuming constant velocity.

$$\tilde{\mathbf{X}}_j^{N+2} = 2\mathbf{X}_j^{N+1} - X_i^N \tag{3.7}$$

   (b) If droplet i is already part of a trajectory, its expected position is calculated assuming constant acceleration.

$$\tilde{\mathbf{X}}_j^{N+2} = 2.5\mathbf{X}_j^{N+1} - 2X_i^N + 0.5X_i^{N-1} \tag{3.8}$$

4. Find the trajectory that minimizes the separation between its expected position and one of the droplets in image $N+2$. The droplet that this trajectory passes through in image $N+1$ is considered the best match and it is added to the trajectory for droplet i from image N.

The PTV code output is an additional column of data, appended to the ImageJ results, that contains the trajectory number for each droplet in the file. To find all the droplets in a particular trajectory, one needs only to search for all the droplets in the file that share that same trajectory number. The order of the droplets can be determined by the image number associated with each droplet in the trajectory. Velocity and accelerations are determined in a post-processing step described in the following section.

3.6 PTV Post Processing

3.6.1 Spline Fits to the Droplet Trajectories

Rather than calculating velocities for each droplet using a forward or backward difference formula, a univariate cubic spline was fit to the droplet coordinates for each trajectory. The advantage of the spline fit is that it enables the calculation of smooth first and second derivatives of the resulting function to compute velocities and accelerations for the droplets. Even at the maximum magnification, when using a finite difference formula, the pixelization of the droplet positions resulted in a high prevalence of particular velocity values. This was especially problematic in the transverse[†] velocities since their relatively small magnitudes exacerbate the pixelization problem. Many droplets had transverse displacements of exactly one, two, or sometimes zero pixels. This produced very strong peaks in the probability distribution functions (PDF) of the velocities, causing it to be unphysically not smooth regardless of the binning strategy used. Despite being a computationally intensive process

[†]vertical or spanwise, depending on the orientation of the illumination plane.

due to the large number of trajectories, differentiating the spline fits produced much smoother results and, thus, justified the computational cost.

The post processing first eliminates any trajectory shorter than four images long. These short tracks do not represent actual trajectories in a robust way. The remaining trajectories are processed through a univariate spline fitting routine that fits the data to a series of polynomial segments. A positive smoothing factor (S) is prescribed as an input, and this value is used to determine the number of polynomial segments in the spline fit. The number of polynomial segments is increased until the smoothing factor condition given by (3.9)) is satisfied. If x_i and y_i are a set of i coordinates to be fit with a spline, and $s(x)$ is the spline function, then the smoothing factor condition is given by

$$S \geq \sum_{i}^{N} \Big[y_i - s(x_i) \Big]^2. \tag{3.9}$$

To determine an appropriate value of the smoothing factor, an acceptable fit must produce a spline that passes within a reasonable distance from each droplet centroid location. The purpose of the spline is to compensate for the fact that the camera's sensor takes the droplet's true position, which exists on a continuum of possible positions in space, and forces it to fit into a particular discrete position (the pixel map). The camera discretizes the image space into a finite number of possible positions that correspond to the center of each pixel. The spline fits are intended to counter this pixelization by allowing the droplet coordinates to relax to a position within the pixel where it was detected, but the spline fit must not be so flexible so as to avoid returning droplet positions that are far away from the detected position. The spline fit is forced to pass within 0.25 pixels of each original particle centroid location, or alternatively, a maximum error is specified such that $y_i - s(x_i) <= 0.25$ for all i. The smoothing value is then calculated to be $S = L \times (0.25)^2$, where (L) is the trajectory length, which is equivalent to the number of images in the trajectory. A maximum error of 0.25 is used, rather than 0.5, in order to decrease the probability that a spline fit solution

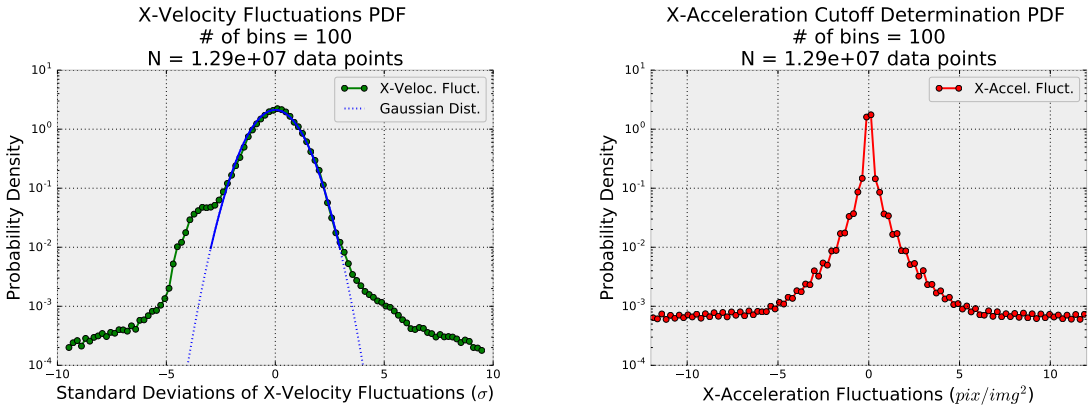

Figure 3.6: PDFs of the streamwise (X) velocity and acceleration prior to the data filtering used to remove the noise floor in the data. This floor is easiest to see in the acceleration PDF.

will have an error greater than 0.5 for one coordinate by having very small errors at the rest of the coordinates.

3.6.2 PTV Results Filtering

One of the drawbacks of polynomial regressions is that they can develop very steep derivatives very quickly, especially near the ends of the range of data fitted. This leads to unrealistic velocity and acceleration values. For some trajectories, the spline fitting routine completely fails to find a spline that can satisfy the smoothing condition. Both of these scenarios are dealt with by filtering the data set.

The first filter simply removes the trajectories with failed spline fits as well as any of the velocities or accelerations that are more than ± 7 standard deviations from the mean. This removes the non-physical values that are large enough to skew the mean value of the data set despite their relative infrequency. The next round of filtering involves plotting PDFs of the velocities and the accelerations to determine where the noise floor in the data occurs. Figures 3.6(a) and 3.6(b) show representative plots of the velocity and acceleration data

with this noise floor. For each of the PDFs of the X- and Y-velocities, as well as the X- and Y-accelerations, a range of data was determined in terms of standard deviations from the mean, that clipped off most of the noisy data. This final filtering process is iterative as the mean values of the PDFs shift slightly as data is removed. Eventually, the mean values converge and at this point the filtering is considered complete.

The final adjustment made to the data corrects for any misalignment between the camera and the direction of gravity. The relatively small settling velocities are particularly sensitive to camera alignment due to their small magnitudes. Alignment of the camera axis with the wind tunnel test section within 1° is not feasible in this high Reynolds number laboratory environment. To account for any misalignment, the vertical velocity data are corrected in post-processing. The details of the theory behind this correction will be described in more depth in Section 5.1.2. In short, assuming that droplets with small Stokes numbers should behave like perfect flow tracers, and assuming that droplets with large Voronoi areas (small local concentrations) will not exhibit enhanced settling velocities, then the subset of droplets that fit both those categories should have zero mean vertical velocity just like the gas carrier flow. At all three measurement stations, the mean vertical velocity for this subset are non-zero. To correct the data, the mean vertical velocity of the subset is subtracted from all the vertical velocities in the data set. The result is that the spread between the mean vertical velocities was reduced from $4.82\,{}^{\mathrm{cm}}/_{\mathrm{s}}$ to $0.33\,{}^{\mathrm{cm}}/_{\mathrm{s}}$. The vertical velocities are shown in Table 3.2.

3.7 PTV Measurement Results and Statistics

Table 3.3 compares the results of the streamwise component of the velocity measured with PTV to the hotwire anemometry (HWA) and the Pitot rake velocity measurements. The mean velocities from the PTV analysis agree well with the other two measurement techniques, supporting the common finding that the particles have the same mean streamwise velocity

Table 3.2: Vertical velocities before and after the adjustment to correct for camera misalignment.

Station	Before $\langle V_y \rangle$ cm/s	After $\langle V_y \rangle$ cm/s
20M	3.77	-2.30
30M	0.39	-2.38
40M	-1.05	-2.63
Spread:	4.82	0.33

as the carrier gas in the wind tunnel and that the RMS of this velocity component is close to, but lower than, the carrier gas u_{rms}. Plots of the particle velocity and acceleration PDFs, in both the streamwise (X) and vertical (Y) directions, are shown in Figures 3.7– 3.12. The acceleration PDFs show the signature of the limits of the image resolution in the periodic spikes in the probability density. This is due to the pixelization creating discretized droplet positions. The spline fits do a good job of smoothing the velocity PDFs, but the second derivatives are much more sensitive to the pixelization and preserved a little of this effect.

The X-velocity PDFs at 30M and 40M both share a prominent, non-Gaussian feature. They have a higher than normal probability of negative velocity events from about 3σ out to where the data are limited by the noise floor at 4σ. The current interpretation of this phenomenon is that the high-speed movies, each one extending only over $\approx 1\,\mathrm{s}$ in time, captured one or more large[‡] coherent structures passing through the field of view. These structures reduced the velocities measured for all the droplets in that portion of the movie enough to alter the statistics of the entire data set. This hypothesis is corroborated by the presence of significantly-long sequences of images in which the number of droplets matched

[‡]but still much smaller than the integral length scale of the turbulence

Table 3.3: A comparison of the mean and fluctuating velocities measured at various points in the test section using PTV, HWA, or a Pitot tube rake. H, V, and CL are used to identify measurements made at horizontal, vertical or centerline measurement locations, respectively.

Station	Particle Tracking Velocimetry			Hotwire		Pitot Rake
x/M	U (m/s)	u' (m/s)	v' (m/s)	U (m/s)	u' (m/s)	U (m/s)
20H	2.88	0.29	0.21	2.67	0.30	2.74
20V	2.84	0.24	0.22	3.09	0.33	
30H	2.87	0.21	0.17	2.73	0.22	2.70
30V	2.77	0.20	0.17	3.05	0.26	
30CL	2.93	0.22	0.17	2.85	0.19	
40H	2.82	0.22	0.16	2.68	0.19	2.63
40V	2.70	0.18	0.16	3.00	0.24	

to trajectories by the PTV algorithm suddenly drop. This decrease in trajectory matches happened because the slow velocities fell outside the PTV search area, which was defined as $\pm 4\sigma$ deviations from the mean velocity calculated from all the movies.

This issue was solved by increasing the size of the search area in the PTV algorithm to 5 standard deviations of the velocity fluctuations. This change resulted in a significant increase in the number of particles successfully associated with a track, but introduced these non-Gaussian "bumps" on the velocity PDFs. The wind tunnel can occasionally eject coherent regions of slow velocity fluid out into the edges of the core region of the flow where the PTV measurements are taken. The lack of integral-scale sampling homogeneity notwithstanding, the good agreement between the Pitot rake, PTV, and HWA velocities validates the use of the new PTV code to investigate the droplets settling and radial velocity behavior.

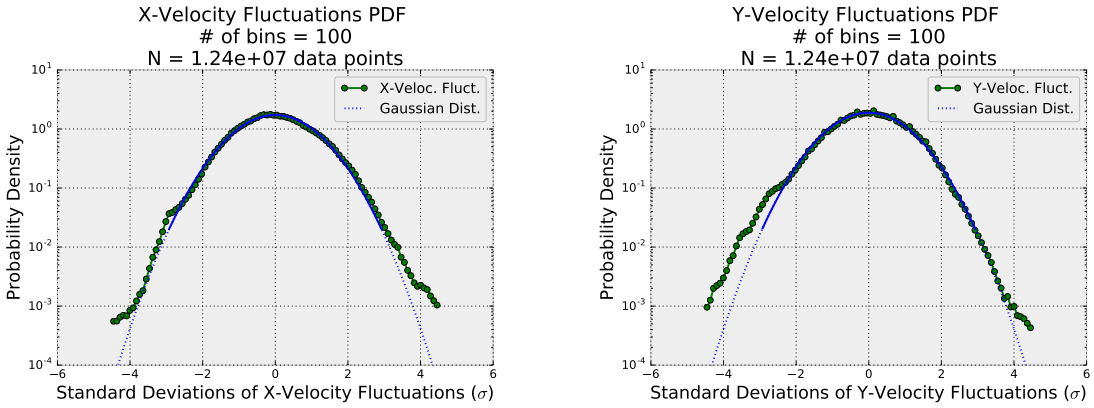

Figure 3.7: Streamwise (X) and vertical (Y) velocity fluctuation PDFs at $x = 20$M. Gaussian fits to the PDFs are shown with a solid and dotted blue line. The solid portion of the curve identifies the range of the PDF data what was used to calculate the standard deviation for scaling the Gaussian fit.

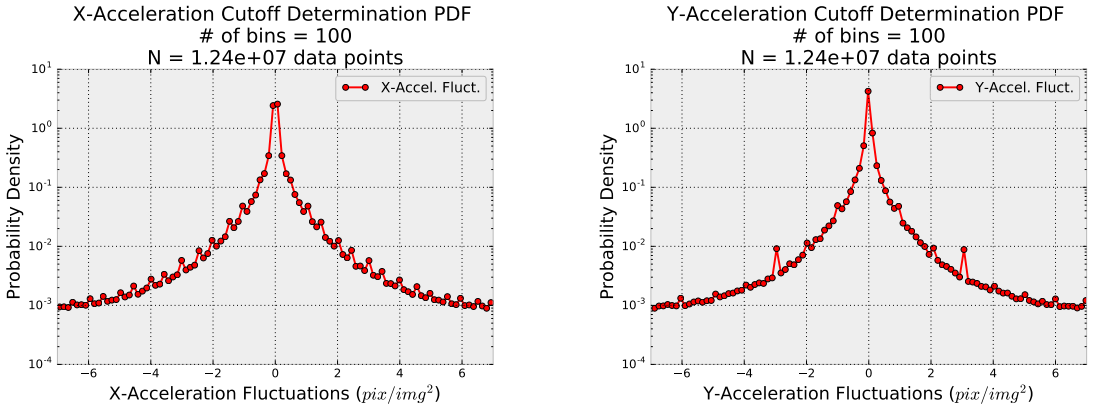

Figure 3.8: Streamwise (X) and vertical (Y) acceleration PDFs at $x = 20$M.

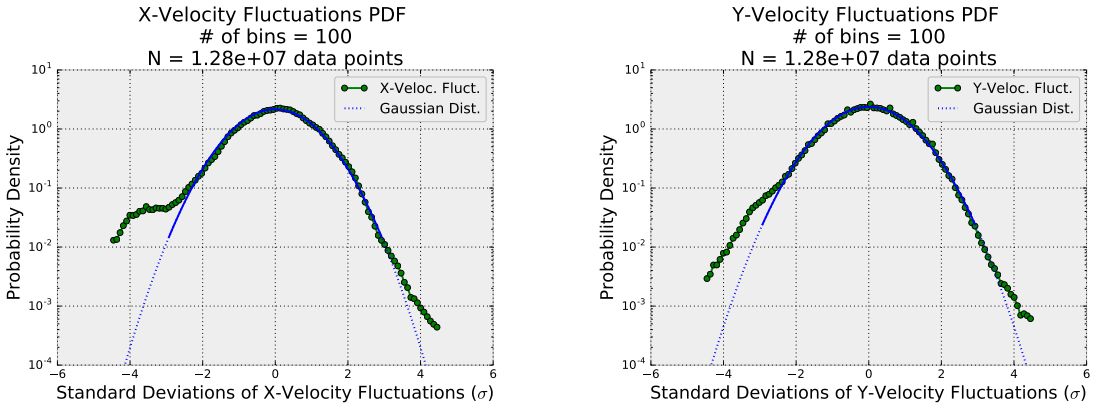

Figure 3.9: Streamwise (X) and vertical (Y) velocity fluctuation PDFs at $x = 30$M. Gaussian fits to the PDFs are shown with a solid and dotted blue line. The solid portion of the curve identifies the range of the PDF data what was used to calculate the standard deviation for scaling the Gaussian fit.

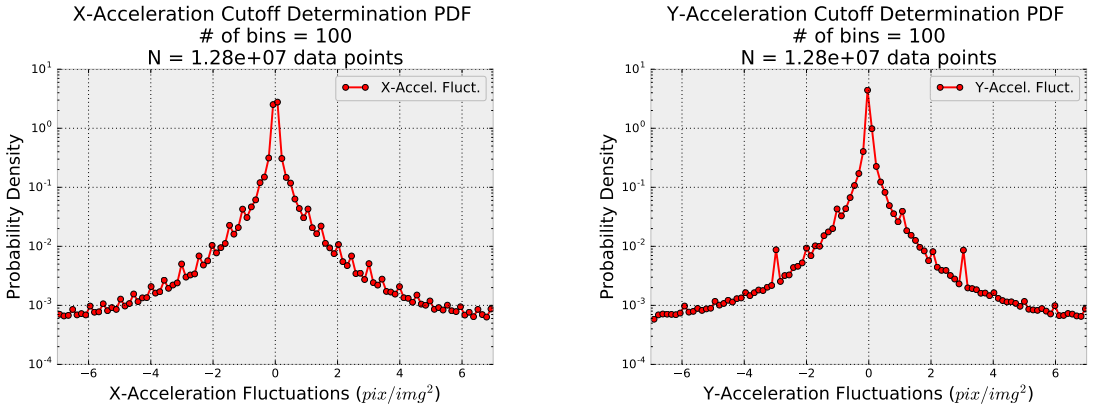

Figure 3.10: Streamwise (X) and vertical (Y) acceleration PDFs at $x = 30$M.

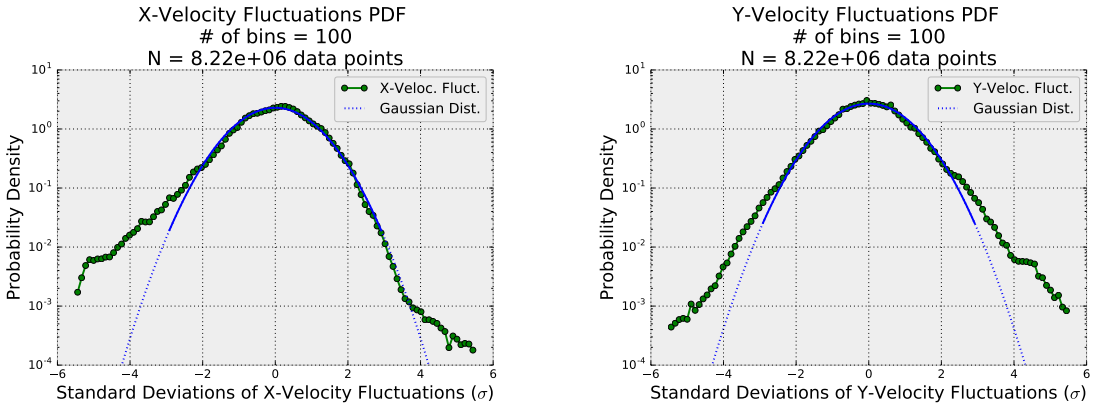

Figure 3.11: Streamwise (X) and vertical (Y) velocity fluctuation PDFs at $x = 40$M. Gaussian fits to the PDFs are shown with a solid and dotted blue line. The solid portion of the curve identifies the range of the PDF data what was used to calculate the standard deviation for scaling the Gaussian fit.

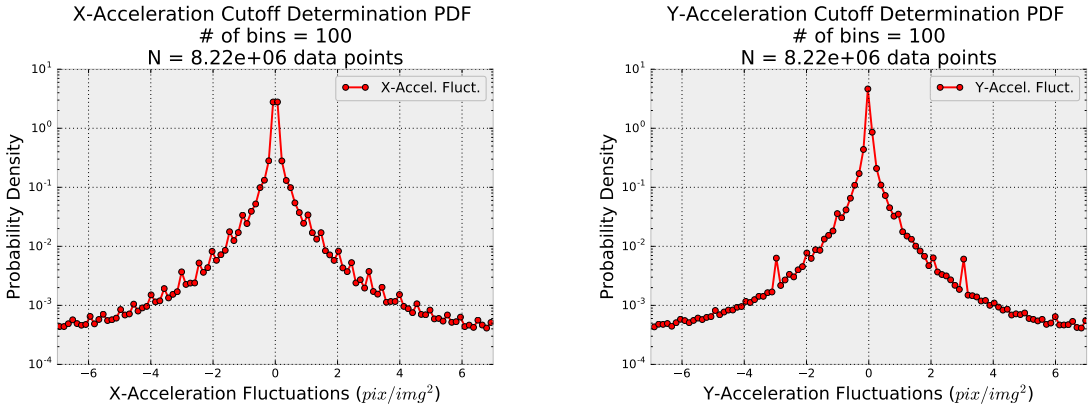

Figure 3.12: Streamwise (X) and vertical (Y) acceleration PDFs at $x = 40$M.

Chapter 4

PREFERENTIAL CONCENTRATION

4.1 Radial Distribution Function (RDF)

4.1.1 Background on the RDF

Sundaram and Collins (1997) were the first to use the Radial Distribution Function (RDF) to quantify the local concentration of particles in a multiphase flow as the result of preferential concentration. The RDF measures the probability of finding a droplet in a spherical shell of thickness dr and radius r_i, centered on the position of another droplet. The RDF is normalized such that a population of drops that are separated by a Random Poisson Process (RPP) distribution of distances will have an RDF that is equal to 1 everywhere. If the droplets concentrate preferentially, the RDF will reflect this local concentration by having a value greater than 1. For an illustration, see Figure 4.1. Originally derived for the field of solid mechanics to describe the distribution of atoms in crystalline or glassy structures, Sundaram and Collins (1997) show that the RDF is directly proportional to the rate of collisions in a monodisperse droplet system (Eq. 1.4). The RDF is, by definition, a three-dimensional function. Due to experimental limitations, 1D and 2D versions of the RDF are computed in this dissertation. These lower-dimensional RDF results are associated with the 3D RDF values via relationships derived by Holtzer and Collins (2002).

4.1.2 1-D RDF Results and Analysis

The 1D RDFs are computed from Phase Doppler Particle Analyzer (PDPA) measurements. By assuming the experiment is statistically stationary and employing Taylor's frozen tur-

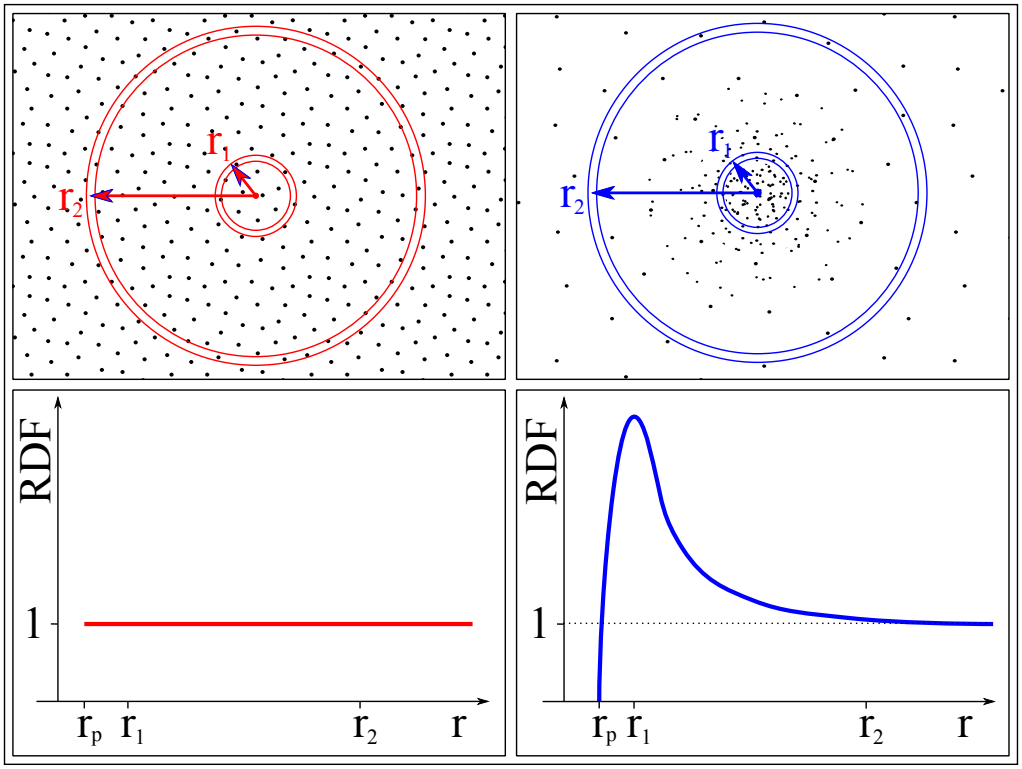

Figure 4.1: A cartoon illustrating the RDF scaling. On the left, a random Poisson distribution results in no preferential concentration (RDF = 1 for all r). On the right, an obvious cluster of particles results in a RDF > 1 for $r \approx r_1$.

bulence hypothesis* (Taylor, 1938), the wind tunnel's mean convective velocity is used to convert the temporal information from PDPA measurements of droplet arrival-time into a droplet separation along a line oriented in the streamwise direction. From this separation information, the probability that two droplets are within a certain distance along this line (the equivalent in 1D to the spherical shell in 3D) can be computed. The 1D RDF is the distribution of that probability as a function of the separation distance.

To determine the 1D RDF, the number of droplets found at increasing radial distances from the location of a central droplet are calculated. This process is repeated with each droplet in the data set serving as the central droplet and the results are averaged and normalized with the total number of droplet pairs found within the sample. The result is a large set of data that characterizes the separation distances between all possible droplet pairs within a certain maximum distance at which the statistics lose their physical meaning. At a large enough separation distances, a spatial correlation is no longer expected to exist between two droplets. Physically, this would occur for the separation distances that are larger than the largest scale in the particle concentration field and, in a turbulent flow that interacts with the inertial particles, this length scale corresponds to the largest scale of the turbulence: the integral scale. To present the RDF data, a histogram plot is produced with the probability of finding particles at a given separation as a function of that separation distance. In three dimensions, the width of the histogram bins corresponds to the thickness of the spherical shell surrounding the central particle. In one dimension, the length of the sampling shell and the size of the histogram bins are identical. Once the separation distances have been sorted and counted in the histogram, the 1D RDF is calculated by the equation

*Taylor's hypothesis allows us to convert point measurements collected over time into spatial information about the structure of the turbulent fluctuations for homogeneous, shearless, grid turbulence at $u'/U_{avg} \ll 1$ (Pope, 2006). In the center of the wind tunnel, u'/U_{avg} is always approximately 0.1 or less. It has been shown from theoretical analysis (Lumley, 1965) that, for a turbulence intensity of 0.1, Taylor's hypothesis introduces an error of approximately 5% to the turbulent dissipation rate and approximately 1% to the Kolmogorov scales.

from Holtzer and Collins (2002) as follows:

$$g_{1D}(r_i) = \frac{\hat{P}_i/L_i}{\hat{P}/L} \tag{4.1}$$

where $\hat{P}$ is the total number of particle pairs in a data set, $\hat{P}_i$ is the number of pairs with separation distances between $r_i - \Delta r/2$ and $r_i + \Delta r/2$, L is the total spatial extent of the sample, and $L_i = \Delta r$ is the length of the sampling shell.

Figures 4.2 – 4.4 show the RDFs at three places along the length of the wind tunnel ($x =$ 14M, 17M, and 22M)[†] calculated out to 30η. If the droplets in our flow were separated by a perfectly random distribution of distances (i.e. the RPP) then the RDF would be equal to 1 everywhere. Our RDFs are much greater than 1 at small separation distances indicating that the droplets accumulate in close proximity to each other due to the turbulence. The length scale of this accumulation relates to the Kolmogorov scale of the carrier flow, but extends down to separations on the order of the diameter of the droplets. This is the key result that links preferential concentration of droplets by turbulence to the collision kernel: the droplet RDF—a measure of the preferential concentration of droplets that the collision kernel is directly proportional to—has a large peak at a spacing below the Kolmogorov scale (η). With this, previous results of inertial droplet clustering at scales around 10η are extended to much larger Re_λ and lower turbulent dissipation rates—a parameter range more representative of cloud conditions. The RDF does not decay to a value of 1 until calculated for separations on the order of the integral length scale (approximately 2000η) at this Reynolds number (Figure 4.5). This is in conflict with some previous experimental measurements of the (2D) RDF, but fully consistent with the view that preferential accumulation for a polydisperse particle population occurs throughout the inertial range, with the purely random spatial distribution being recovered only at very large scales that integrate over lengths larger than

[†]The data used to compute the 1D RDFs was collected in an older version of the wind tunnel test section that was shorter and had irregularly spaced windows. This is why the locations of these measurements do not correspond with others reported in this dissertation.

any correlation length of the turbulence. This aspect of the particle concentration field will be analyzed in detail in the context of the 2D RDF measured from imaging in the wind tunnel under almost identical conditions as the ones presented here for the 1D RDF.

The PDPA probe's finite cross section defines the width of the volume of fluid that is measured as it passes through its cross section. This size-limitation introduces a distortion in the RDF computed for very small separations (comparable to the dimensions of the probe volume). As a result, the 1D RDF can not computed with sufficient accuracy at separation distances smaller than 0.19 mm, or about 0.5η based on the Kolmogorov length scale at Station 2 ($x/\mathrm{M} = 14$). For this reason, the smallest bin used when calculating the RDF is centered around an inter-particle separation of 1η.

The data obtained for the 1D RDF are fit to an exponential law, following (Reade and Collins, 2000),

$$g(\hat{r}; St) = 1 + c_0 \hat{r}^{-c_1} \exp[-c_2 \hat{r}], \tag{4.2}$$

where $g(\hat{r})$ is the RDF, $\hat{r} = r/\eta$, and c_0, c_1, and c_2 are fit coefficients. This allows for extrapolation of the measurements to separation distances smaller than experimental limits; all the way to the separation distance at contact that is the value of interest for the computation of the collision kernel. Additionally, this exponential law fit provides a means of comparison between the different conditions measured in this dissertation and in other studies, and the fit provides quantitative information that can be used to validate future DNS studies.

Figures 4.2 – 4.4 show that Eq. (4.2) fits the experimental data well, except at the smallest separations where it under-predicts the degree of preferential concentration. This is consistent with the fact that droplet-droplet interactions (through collisions or aerodynamic perturbation as computed in four-way coupling models), intrinsically present in this dissertation's experimental data, were not present in the DNS data from which the exponential law fit expression was developed, but are critical to the behavior of the droplets at these small separations distances.

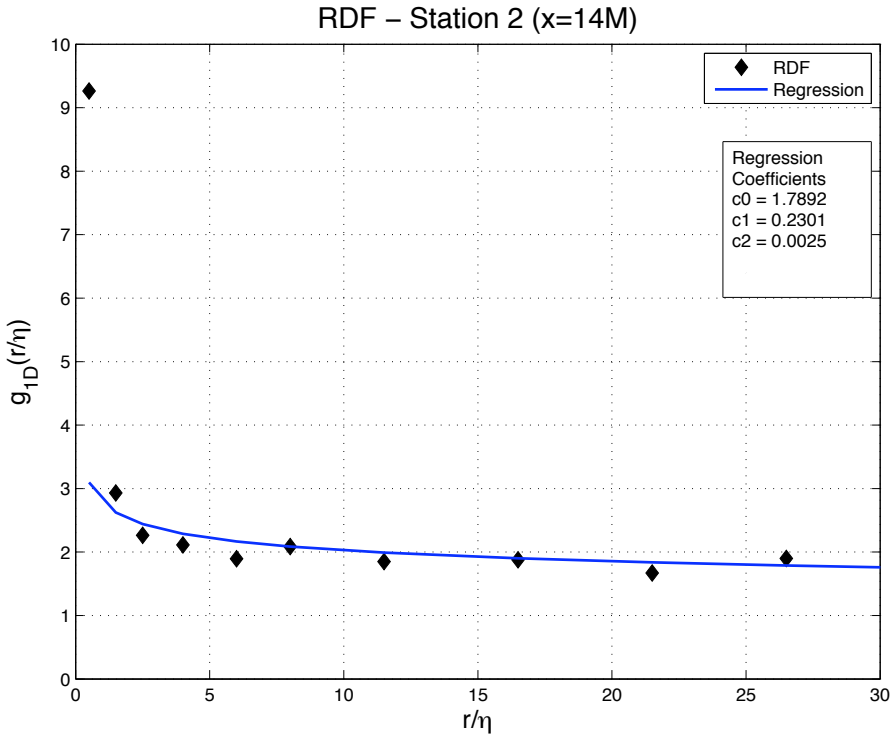

Figure 4.2: The RDF at Station 2 ($x/M = 14$) and the regression to Equation 4.2 shown at small separations. The RDF was calculated from PDPA measurements. Reproduced from Bateson and Aliseda (2012) with permission from Springer.

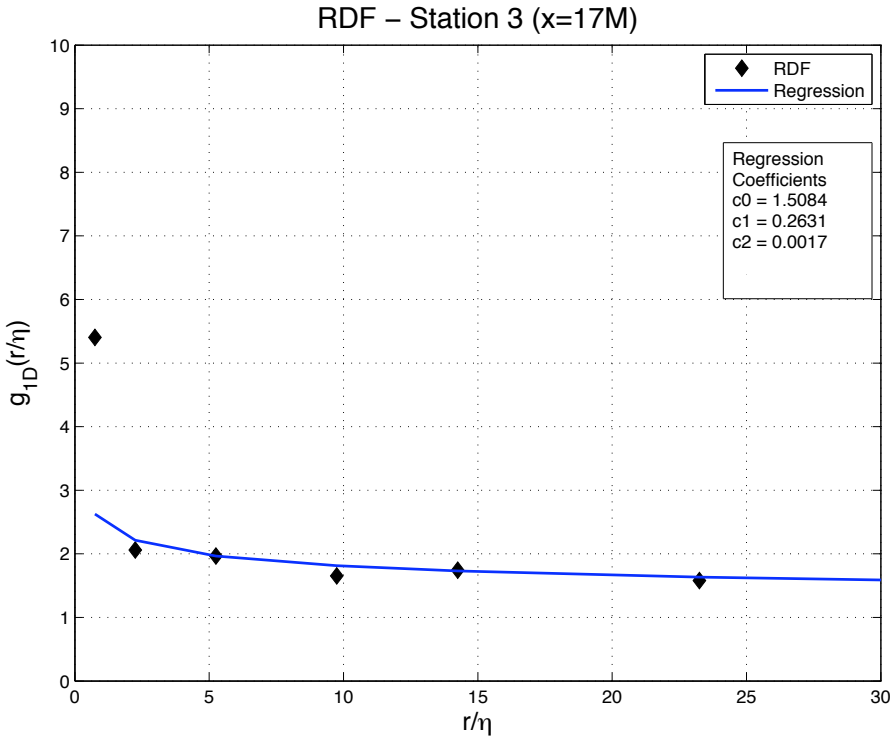

Figure 4.3: The RDF at Station 3 ($x/M = 17$) and the regression to Equation 4.2 shown at small separations. The RDF was calculated from PDPA measurements. Reproduced from Bateson and Aliseda (2012) with permission from Springer.

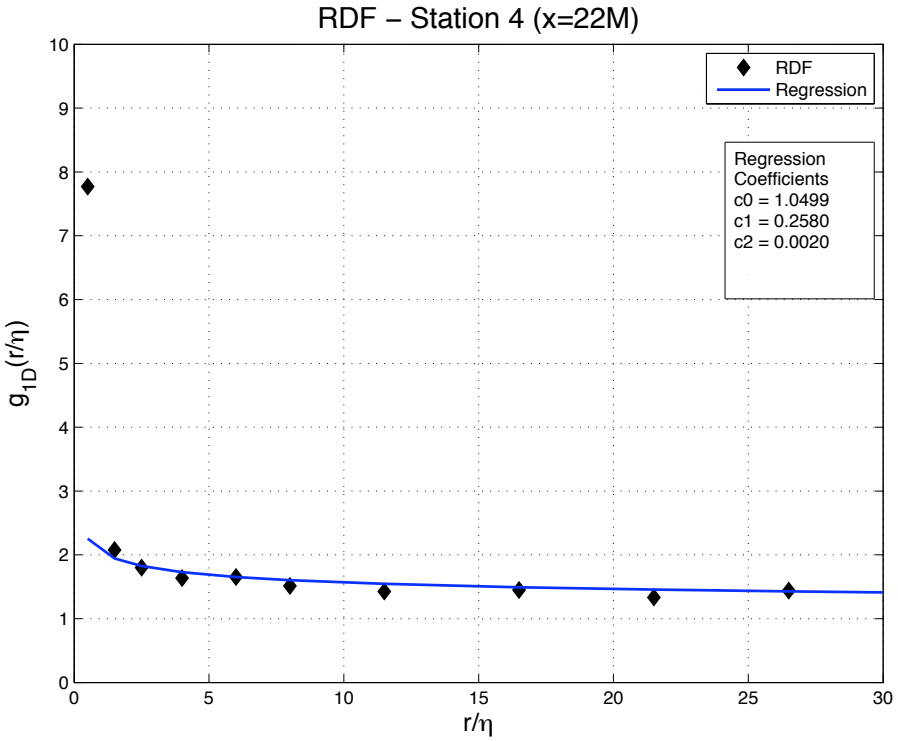

Figure 4.4: The RDF at Station 4 ($x/M = 22$) and the regression to Equation 4.2 shown at small separations. The RDF was calculated from PDPA measurements. Reproduced from Bateson and Aliseda (2012) with permission from Springer. Reproduced from Bateson and Aliseda (2012) with permission from Springer.

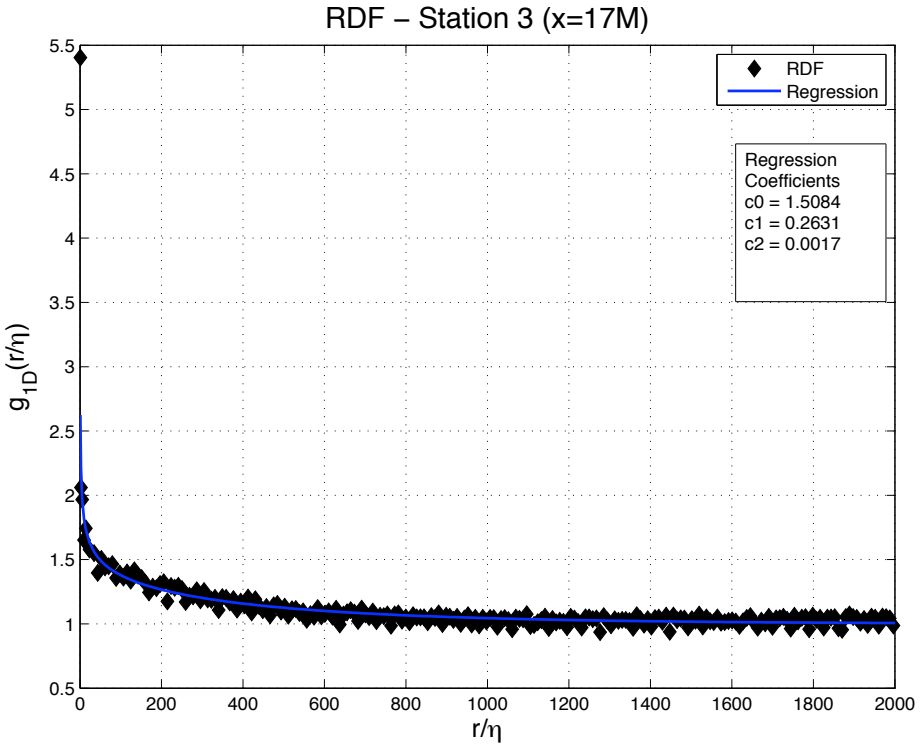

Figure 4.5: The full 1D RDF ($g_{1D}(r/\eta)$) at Station 3 ($x/M = 17$) plotted as a function of the separation distance normalized by the Kolmgorov length scale. The solid line shows the regression to Equation 4.2. Both were calculated out to $2000\,\eta$ to show the complete decorrelation of droplet separation distance. The RDF was calculated from PDPA measurements. Reproduced from Bateson and Aliseda (2012) with permission from Springer.

4.1.3 2-D RDF Results and Analysis

Saw (2008) derived a formulation of the RDF equation that allows for the calculation of the RDF for a subset of the total population of particles. This is particularly useful for determining the RDF from a data set derived from images of particle locations in a turbulent flow (2D RDF). An RDF calculated for particles near the edge of an image will be distorted by the absence of particles beyond the image's extent. To avoid this distortion, a maximum radial separation distance is defined such that the RDF is computed only out to that separation. This maximum separation is used to compensate for the limitation imposed by the image field of view by defining a rectangle centered in the middle of the image that it is offset from the edges on all sides by this maximum distance (Figure 4.6). The RDF calculation is limited to only those drops inside the rectangle in the center of the image and the RDF is calculated using Saw's equation adapted for restricted areas instead of volumes:

$$g(r) = \frac{\psi(r)/N_t}{(N-1)\,\delta A_r/A} \tag{4.3}$$

where $\psi(r)$ is the 'sum over number of particles found at distance r', and δA_r is the infinitesimal annular area centered on the particle, N_t is the total number of particles considered in the calculation (the number of particles inside the box, in our case), and $(N-1)/V$ is the average particle density, calculated here as an average for all the images in a given experimental sequence.

The algorithm to compute the RDF from the particle locations extracted from the images starts by identifying the X- and Y-coordinates for all the droplets in a single movie frame or image. Separation distances between each droplet i and every other droplet j in the image are then computed. The algorithm then moves on to the next frame, calculates all the separation distances for that image, and appends the resultant vector onto the vector from all the previous frames. After this process has been performed for all the frames in a sequence, the entire vector with the separation distances for all particles are sorted into

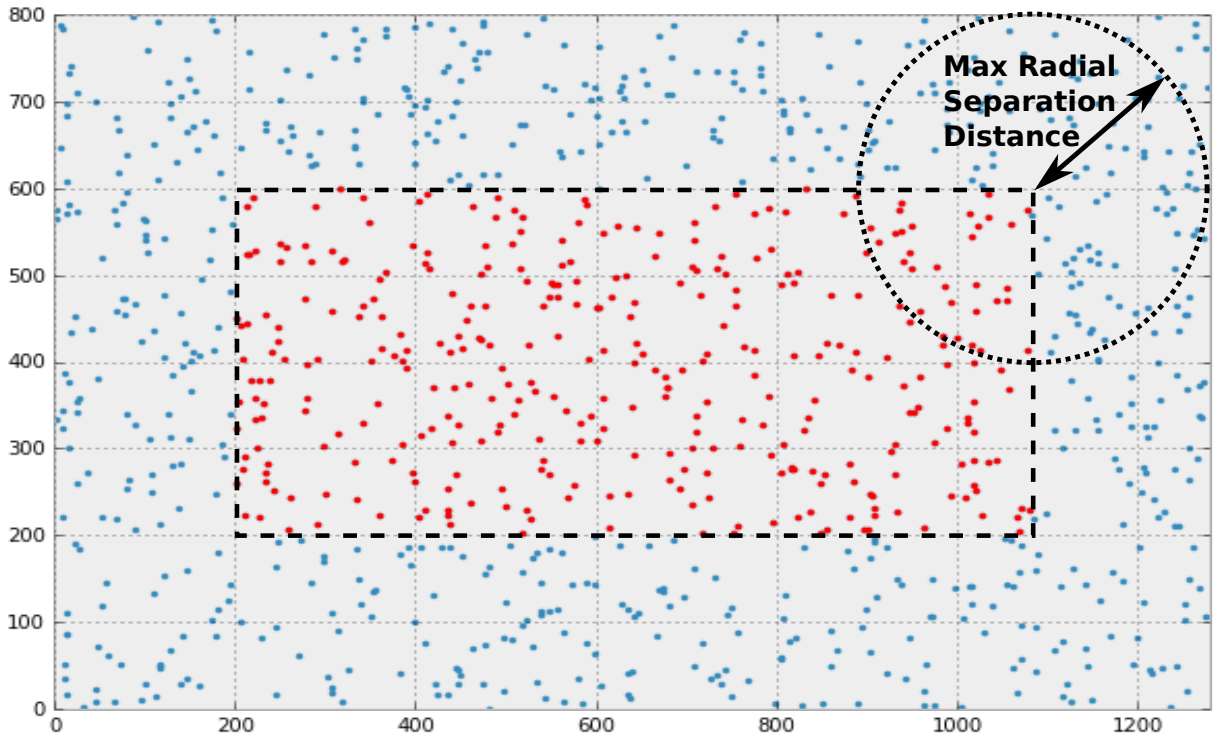

Figure 4.6: Calculating 2D RDFs from finite-sized images. An illustration of how the maximum radial separation distance chosen is used to define a box in the center of each image that will contain the subset of the image's droplets that will be used in the calculation of the RDF. The subset of droplets is used to avoid edge effects influencing the RDF statistics.

histogram bins. These bin counts represent $\psi(r)$ from (4.3). The bin counts are divided by the total number of droplets found in the central box summed up for the entire movie (N_t). Finally, the RDF is calculated by normalizing the bin counts, first by the annular area of the histogram bins (δA_r), and then by the bulk average particle density for all the images taken at a single measurement station ($(N-1)/V$).

Figure 4.7 is a plot of the 2D RDFs for each of the three measurement stations (20M, 30M, and 40M) as well as for both the horizontal and vertical high-speed imaging configurations. These RDFs were calculated using a maximum separation distance equal to 25% of the

shortest dimension of the image, which was a compromise between calculating the RDF out to larger radial distances and maintaining a large enough number of droplets inside the box to have converged statistics.

Figure 4.7 shows evidence of preferential accumulation for the smallest separation distances, peaking between 1.4–1.65 times the average particle concentration, and decaying towards a value of 1.0 for larger separations. Due to the size of our images relative to the flow scales, the RDF can not be computed out to the separation distances needed to see the function decay all the way to 1.0. The peak values of the RDFs are not as high as the values that have been reported in literature for DNS studies. This is partly attributable to the poly-dispersity of the droplet population (Saw et al., 2012) as well as the relatively low Stokes numbers for the majority of the droplets. The percentage of droplets in the experiments that have Stokes numbers close to 1.0 is small enough that the degree of clustering is lower than reported for monodisperse particle populations with $St \approx 1$.

The measurements at the three different stations are statistically indistinguishable, but the RDFs from the horizontal imaging configurations are all lower than those from the vertical configurations. This is consistent with the intuition that clusters of inertial particles under the effect of gravity are not isotropic and that particles accumulate (and therefore spend more time) on the downward side of eddies than on the upward side. To the best of our knowledge, this observation is the first experimental evidence (using two imaging orientations on the exact same flow conditions and locations inside the flow chamber) that clustering is stronger in the vertical direction than in the horizontal direction. Gravity does indeed play a role in the concentration of inertial particles as evidenced by this increase in the maximum value of the RDF in vertical planes compared with horizontal planes under the exact same experimental conditions.

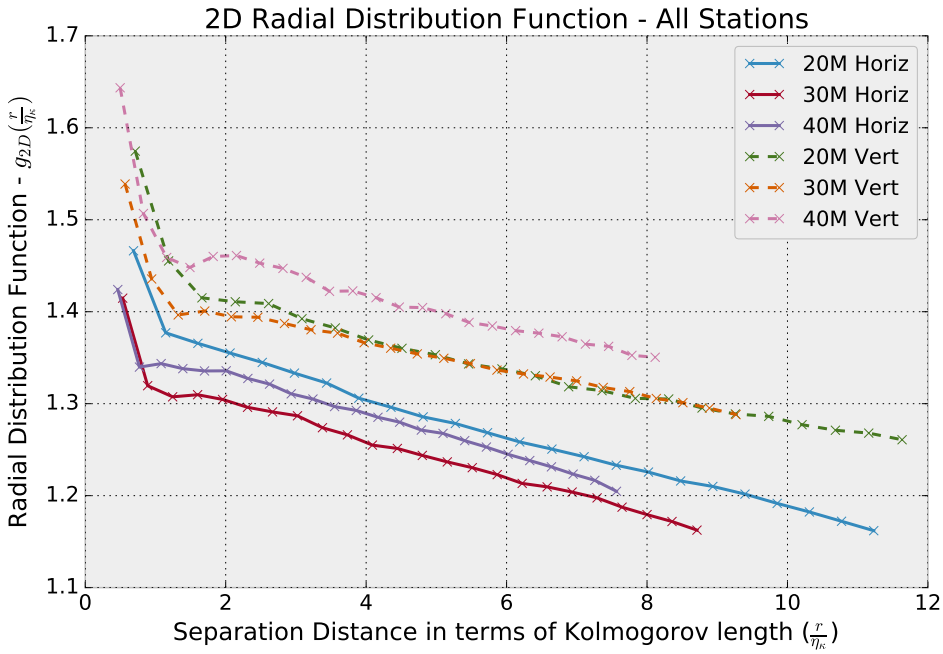

Figure 4.7: 2D Radial Distribution Function - All Stations. A plot of the 2D RDF (g_{2D}) as a function of separation distance in terms of the Kolmogorov length (r/η_κ) from all three measurement stations (20M, 30M, and 40M) for both the horizontal and vertical high-speed imaging configurations.

4.2 Voronoi Analysis

4.2.1 Background on Voronoi Analysis

A Voronoi diagram is a mathematical technique used to divide a 2D space into a group of cells, or tessellations, determined by distances measured to a set of predefined points in the space. Each Voronoi cell is made up of the region of space that is closer to a predefined point than all the other points in the image. As such, Voronoi diagrams are a useful tool for analyzing the clustering, or accumulation, of the points in the diagram since the area of a tessellation is inversely proportional to the local concentration of points. The closer the points are together, the smaller the resulting area of the tessellations. Figure 4.8 is an example of a Voronoi diagram. By calculating Voronoi diagrams for droplets in the experimental images, this technique provides an alternate method for assessing the preferential accumulation of inertial particles in the turbulent flow. One of the disadvantages of the RDF is that it only gives statistically significant information on the preferential concentration as a global or intrinsic property of the multiphase flow. Additionally, the computational time increases exponentially as one calculates the RDF out to larger and larger separation distances. Not only are the Voronoi analysis computations relatively quick in comparison to the RDF, but since the Voronoi areas are associated with particular particles at every time step, Voronoi analysis provides local concentration information that can be tracked through multiple images. This information can be leveraged by conditioning statistics of individual droplet dynamics (for example their settling velocity) based on the droplet's local concentration, as is done in the following chapter in this thesis.

4.2.2 Voronoi Analysis Results

Following the methodology used by Monchaux et al. (2010), after computing the Voronoi cells for any given image, all particles whose areas share a border with the edge of the image

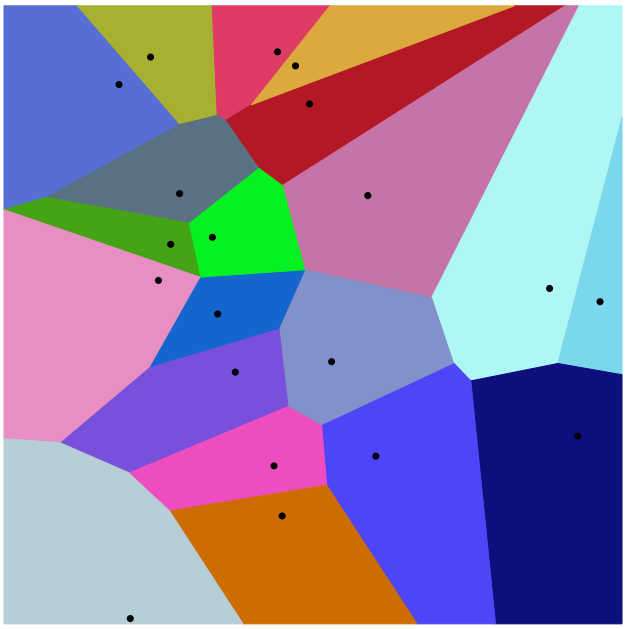

Figure 4.8: An example of a Voronoi diagram. Reference: *By Balu Ertl - Own work, CC BY-SA 4.0, https://commons.wikimedia.org/w/index.php?curid=38534275*

are discarded. These areas are unbounded on at least one side and are infinite as a result (See Figure 4.9). Voronoi results in this dissertation are presented, as in Monchaux et al. (2010), in terms of the normalized area ($\mathcal{V} = A/\langle A \rangle$) and compared to the results of a Random Poisson Process (RPP) as a way of quantifying preferential concentration. The properties of the Voronoi area distribution of a set of particles located spatially according to a RPP were published by Ferenc and Néda (2007); including an expression that approximates the Probability Distribution Function (PDF) of Voronoi areas resulting from an RPP. To date, no exact analytical expression has been found, but the approximation is sufficiently accurate for the purpose of comparing data from inertial particles in turbulence to a random distribution.

Since turbulence tends to cluster inertial particles, the distribution of Voronoi areas is expected to deviate from that of an RPP, as can be see in Figures 4.10 and 4.11. The two points where the Voronoi area PDF crosses the RPP PDF can be used to define clusters and voids (Monchaux et al., 2010). Particles forming clusters can be defined as particles with Voronoi areas below the crossover point where the probability of having a small area is higher in the experimental data than in the RPP PDF. Similarly, voids can be defined as the region of the plot where particles have Voronoi areas larger than the crossover point where the probability of having a large area is higher in the experimental data than in the RPP PDF.

Like the RDF results, comparing the horizontal and vertical data reveals evidence of non-isotropic droplet clustering. This is most easily seen in the data in Table 4.1. The table shows the $A/\langle A \rangle$ values where the Voronoi PDFs intersect with the RPP curves. These are the same values used to define voids and clusters as discussed previously. The "diff." column shows the spread between the intersection points. This spread can be used to quantify the amount of preferential concentration in the flow: the larger the spread, the more obvious the segregation between clusters and voids. The consistently larger spreads in the vertical Voronoi PDFs support the interpretation that there is non-isotropic clustering in the flow

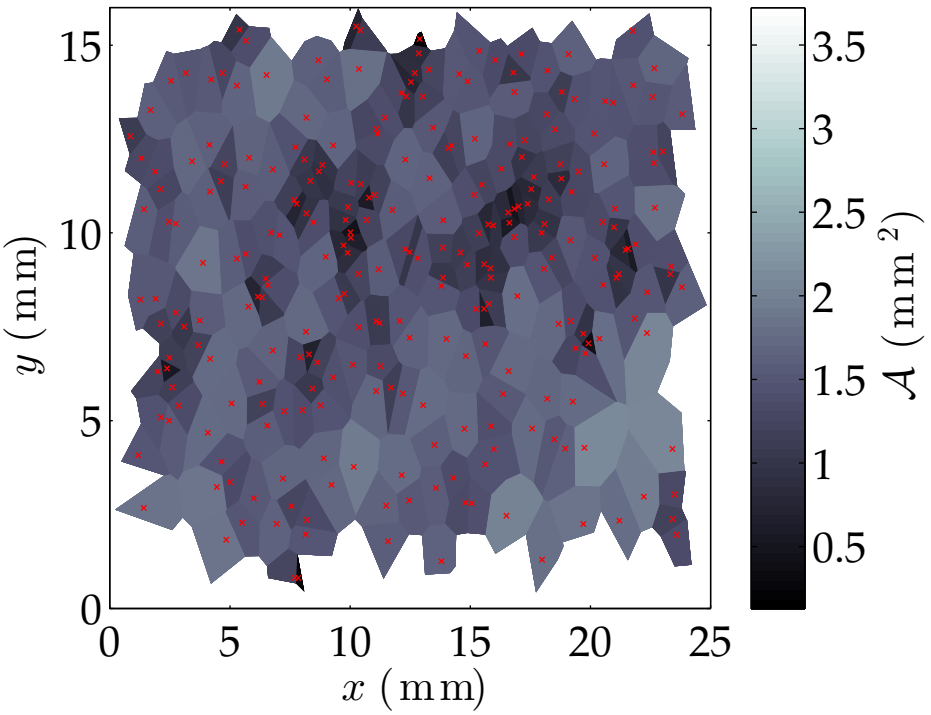

Figure 4.9: Voronoi analysis results. An example of the results of a Voronoi analysis on a representative set of particles. The red points indicate particle positions and the associated Voronoi areas are shaded according to their area. The jagged edge to the areas and the surrounding white space are the result of the exclusion of particles and their associated Voronoi areas along the edge of the image.

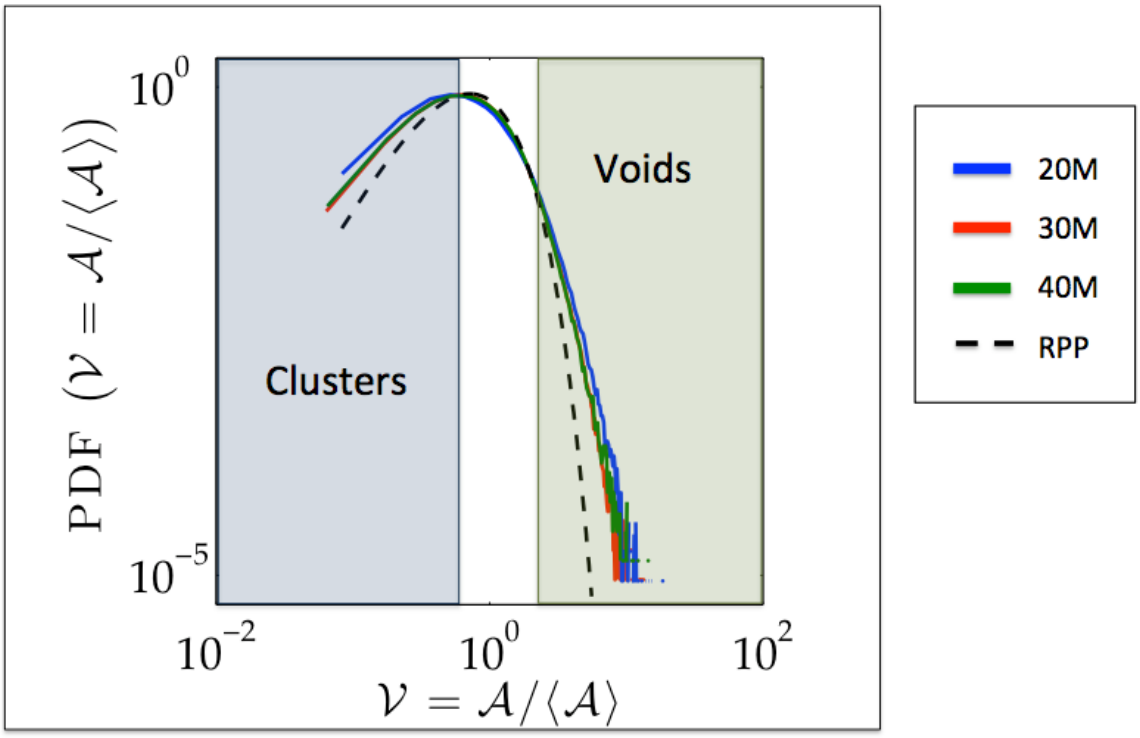

Figure 4.10: A plot of the Probability Distribution Function of the normalized Voronoi area ($\mathcal{V} = {}^{A}/_{\langle A\rangle}$) from vertical imaging data collected at each of the three measurement stations (x = 20M, 30M, and 40M). The dashed line is the PDF for a Random Poisson Process (RPP). Clusters can be inferred by the higher than random probability of small areas and voids by the higher than random probability of large areas.

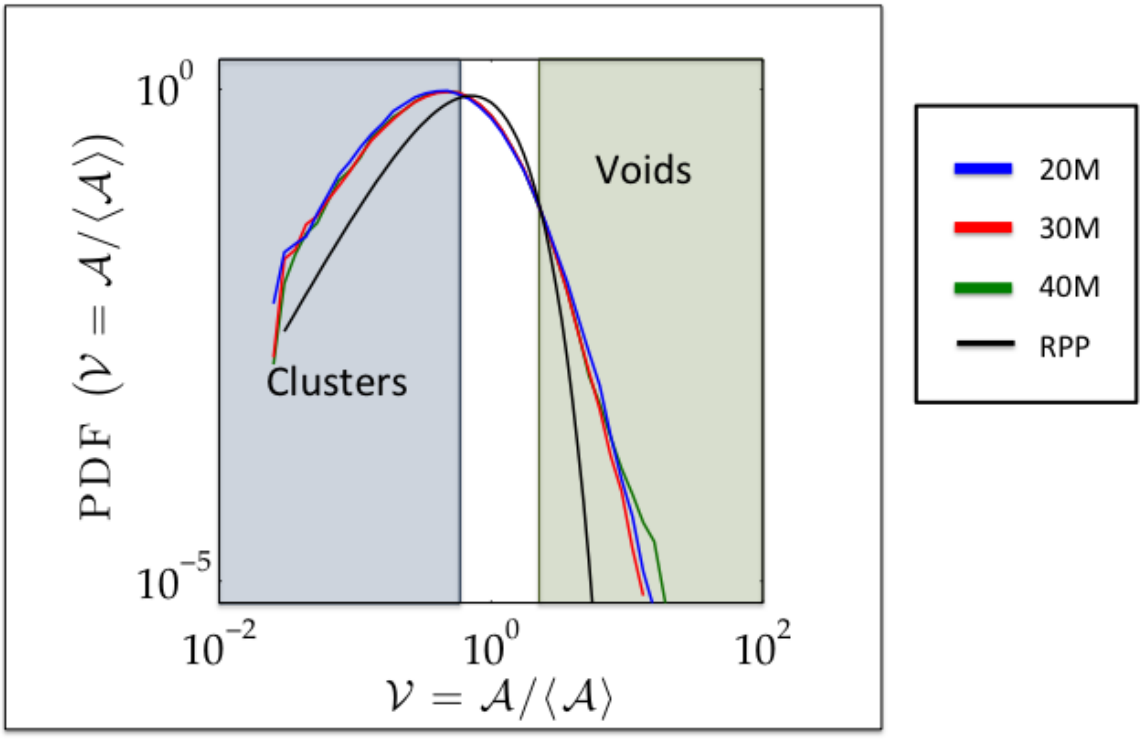

Figure 4.11: A plot of the Probability Distribution Function of the normalized Voronoi area ($\mathcal{V} = {}^{A}/_{\langle A\rangle}$) from horizontal imaging data collected at each of the three measurement stations (x = 20M, 30M, and 40M). The solid line is the PDF for a Random Poisson Process (RPP). Clusters can be inferred by the higher than random probability of small areas and voids by the higher than random probability of large areas.

Table 4.1: A comparison of the horizontal and vertical normalized Voronoi areas $A/\langle A \rangle$ corresponding to the intersection points with a Random Poisson Process PDF.

	Vertical			Horizontal		
Station	Cluster	Void	Diff.	Cluster	Void	Diff.
20M	0.664	2.171	1.507	0.637	2.049	1.412
30M	0.652	2.228	1.576	0.617	1.949	1.332
40M	0.647	2.218	1.571	0.602	1.906	1.304

favoring the vertical direction.

Additionally, the data in Table 4.1 and Figures 4.10 and 4.11, show that clusters are larger for the vertical images: more particles with small areas, and this increased probability extends to larger areas. The voids—understood as the distance between clusters—are also larger. It makes sense that voids are larger in the vertical data. Since the clusters are elongated, there is more space between them than in the horizontal planes, where they are more round and therefore have less space between themselves.

Chapter 5

DROPLET DYNAMICS AND VELOCITIES

5.1 Settling Velocity

When gravitational forces act, heavy particles have a vertical velocity relative to the turbulent carrier flow that causes them to interact with vortical structures in an anisotropic way, giving rise to preferential sweeping caused by this "crossing trajectories" effect. The particles are swept preferentially to the downward regions in the flow, and as a result, the mean effect of the turbulence on the particles is a downward drag leading to an increased settling velocity (Wang and Maxey, 1993). Aliseda et al. (2002) conducted an experimental study of the settling rate enhancement for inertial particles in turbulent flows and found that the heavy particles injected into homogeneous isotropic turbulence settled significantly faster than they would in a quiescent fluid. For the lowest volume fraction of droplets in the flow, the observations validated the results from earlier computational simulations (Maxey and Corrsin, 1986; Maxey, 1987a; Wang and Maxey, 1993). But a new phenomenon was uncovered where for higher particle concentrations, but still well under the volume fraction for which two- or four-way coupling effects are expected, the settling velocity of particles increased significantly over the value predicted for isolated particles in turbulence. This novel collective effect was attributed to preferential accumulation forming clusters where the particles are locally close enough to interact aerodynamically and enhance their respective settling velocities by falling as a heavy structure in a light fluid.

To examine these phenomena experimentally, the Probability Density Function (PDF) of

the settling velocity is measured and analyzed*, conditioned on the distance to the droplet's nearest neighbor. Then, for further insight, the average settling velocity is computed conditioned on both Voronoi area and droplet size.

5.1.1 Settling Velocity Conditioned on the Distance to the Nearest Neighbor

The settling velocity of each inertial droplet in the flow is associated with the radial distance to its nearest neighbor, computed from the location of all the droplets in an image. The array with the droplet vertical velocity and nearest-neighbor-distance information is then sorted, binned by inter-particle distance. Then, the mean settling velocity for each group of particles with a neighbor at a certain distance is computed. The intent is to use the inter-particle nearest-neighbor distance as a substitute for local concentration. Figure 5.1 shows the settling velocity plot from $x = 40$M.

The PDF of the settling velocity is plotted as a function of the vertical velocity (V_y), non-dimensionalized by the Kolmogorov velocity (v_κ). The PDFs are conditioned on separation distance into seven bins spanning $0 - 10\eta$. The legend shows the number of droplets used in each bin as well as the average vertical velocity for the droplets in that distribution. Only one wind tunnel location (Figure 5.1) is included here as a representative of all the data collected in the experiments. The data from the other two measurement stations are presented in Appendix A. To examine the dependence on turbulent dissipation rate and/or turbulence length scales, Taylor and integral, the settling velocity PDFs from all three measurement stations (with corresponding different turbulence characteristics) are shown in Figure 5.2 using the same range on the axes.

A trend in the height and width of the settling velocity distributions can be seen clearly. The curves at 20M are narrowest and with the highest peak, while the curves from 40M

*The settling velocity is defined as the vertical component of the droplet velocity. A droplet with a negative settling velocity is moving down in the same direction as gravity.

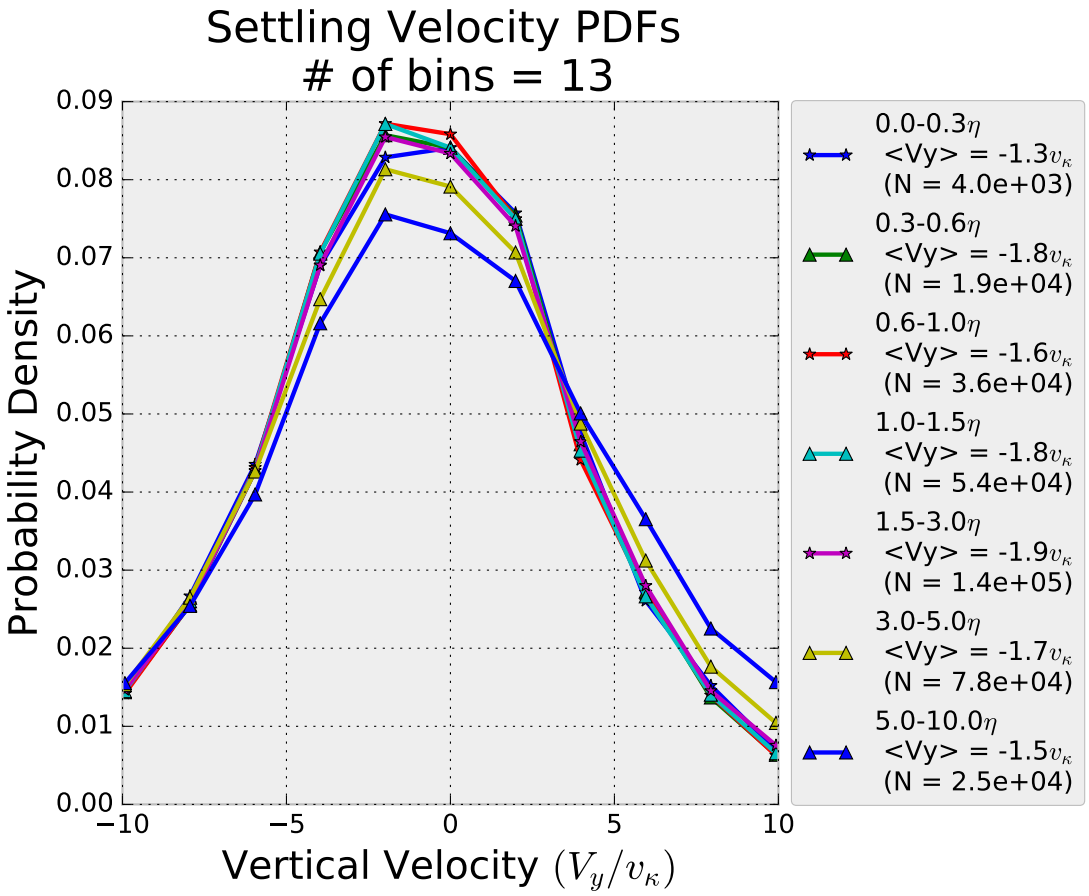

Figure 5.1: Settling velocity PDFs measured at $x = 40$M. The PDFs are plotted as a function of vertical velocity (V_y) scaled by the Kolmogorov velocity (v_κ). The data are binned according to distance to the nearest neighboring droplet measured in multiples of the Kolmogorov length (η). The legend shows the number (N) of droplets in each bin, as well as the mean velocity ($\langle V_y \rangle$), non-dimensionalized by the Kolmogorov velocity for all droplets.

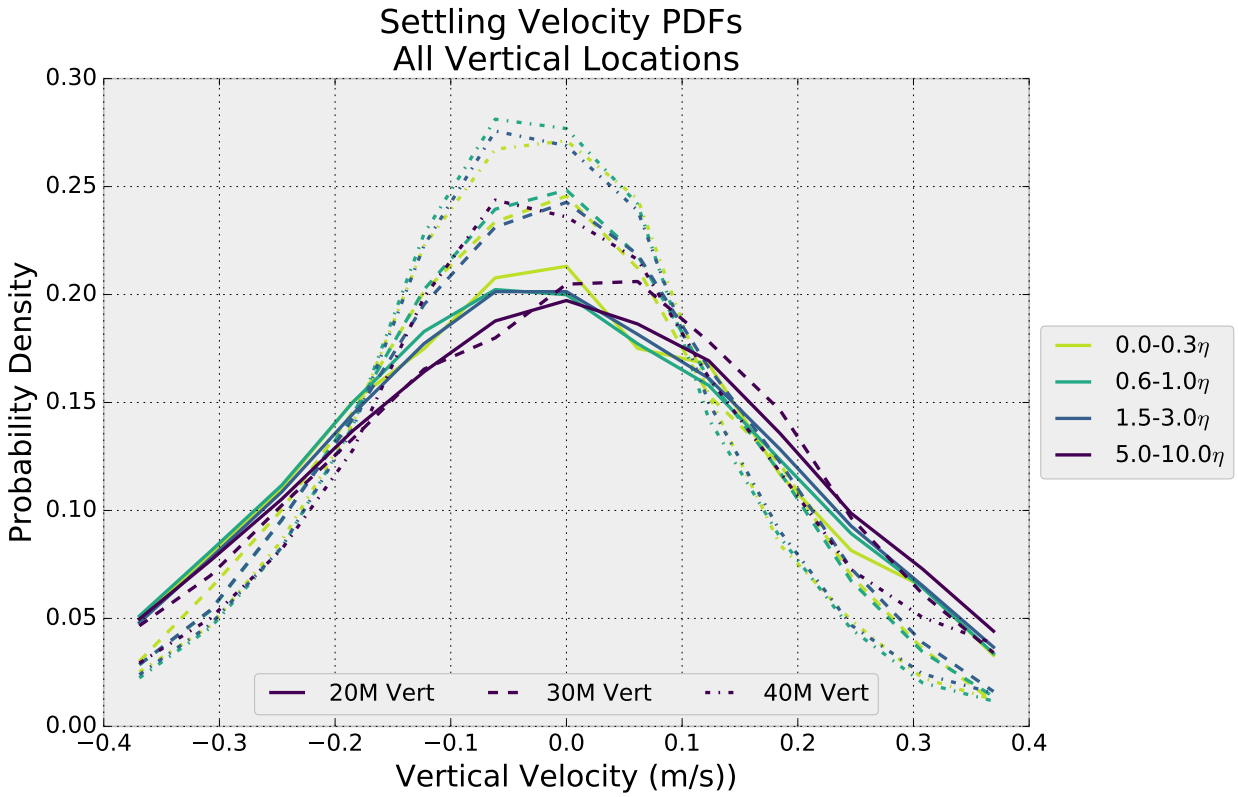

Figure 5.2: Settling velocity PDFs from all three measurement stations: $x = 20$M (—), 30M (- -), and 40M (-.-). The PDFs are plotted as a function of vertical velocity (V_y) in physical units (meters per second, m/s). The data are binned according to nearest-neighbor-distance, non-dimensionalized by the Kolmogorov length (η).

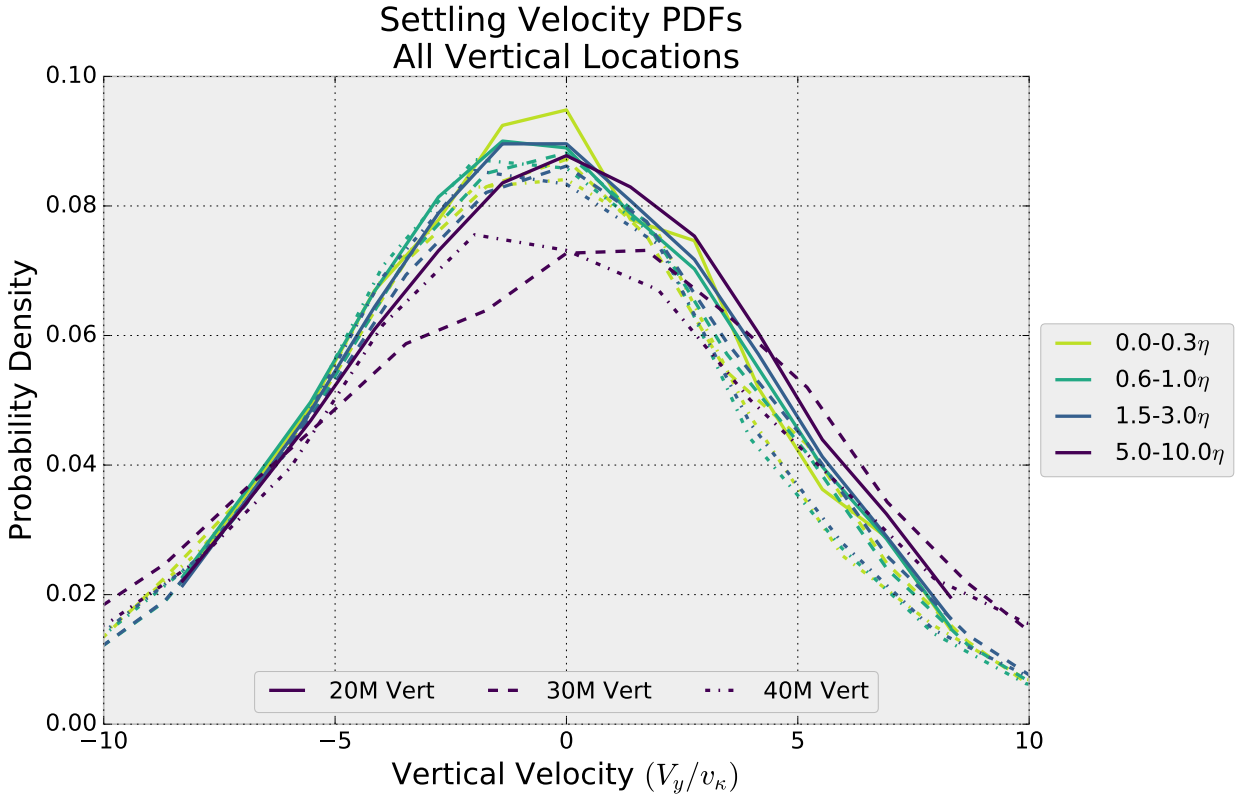

Figure 5.3: Settling velocity PDFs from all three measurement stations: $x = 20$M (—), 30M (- -), and 40M (-.-). The PDFs are plotted as a function of vertical velocity (V_y) scaled by the Kolmogorov velocity (v_κ). The data are binned according to nearest-neighbor-distance, non-dimensionalized by the Kolmogorov length (η).

are the broadest. All the curves share a similar shape, but not the same range. By non-dimensionalizing the vertical velocities with the Kolmogorov velocity, the relationship to the turbulence can be understood. Indeed, the resulting plot in Figure 5.3 shows that the use of the Kolmogorov velocity normalization caused most of the experimental curves to collapse together. The exceptions are the two curves from Stations 30M and 40M corresponding to the bin for the farthest separation distances. The curve from the same bin ($5\eta - 10\eta$) at 20M collapses well onto the rest of the curves.

The fact that these two data sets deviate from the overall trend indicates an evolution in the droplet dynamics as a result of the turbulence. It is not possible to draw definitive conclusions from these relatively simple data visualizations. The outlying curves are plots of the velocity for droplets that have relatively large nearest neighbor distances. Thus, they must exist in a relatively large particle-void in the flow. These outlying curves are also characterized by broader distributions of vertical velocities compared to the curves that have collapsed onto each other.

5.1.2 Settling Velocity Conditioned on Voronoi Area and Droplet Diameter

Calculating Data for the Plot

To investigate further the dynamics related to the settling velocity, the droplets are sorted into bins based on the droplet's Voronoi Area and diameter, and the average vertical velocity is computed for all the droplets in each bin. These data are plotted in Figures 5.4, 5.5 and 5.6. Droplet sizes are approximated from matching the droplet area distribution determined from the particle-visualization images with the PDF of diameters measured with the Phase Doppler Particle Analyzer (PDPA), squared. The droplet areas are determined from the images by analyzing each droplet track and using the largest apparent area as the true area of the droplet. This imaging area is proportional to the light intensity scattered by each droplet, which is proportional to the diameter of the droplet squared. The uncertainty in prescribing sizes to the droplets using this technique is readily acknowledged, but these data are only used in a semi-quantitative way for the sake of making relative size comparisons between "large" and "small" droplets. The consistent, monotonic trend in all the plots supports the use of this approximate droplet sizing technique: larger droplets always have faster settling velocities than smaller droplets. Since the two PDFs do not overlap exactly, the PDFs are stretched to match up their percentile rankings. For example, if droplets with an area of 10 pixels are in the 10th percentile of the area PDF from all the images, then this

area (10 pixels) corresponds to the diameter in the 10^{th} percentile from the PDPA diameter distribution.

The settling velocity data for the smallest particle sizes are used to correct for the possibility of a vertical misalignment in the camera setup relative to the wind tunnel. Specifically, the smallest droplets behave like perfect flow tracers, and as such, they should have zero mean vertical velocity. To avoid the settling velocity enhancement due to collective settling dynamics of particle clusters that affects even the smallest particles, the zero degree orientation in the images is calculated by zeroing the vertical velocity of a subset of the smallest droplets detected in particle voids, as indicated by their very large Voronoi areas. Any non-zero average vertical velocity for this subset of droplets is assumed to be the result of camera misalignment only. Using this process, the vertical velocities for all data sets are adjusted. The result of these corrections can be seen in the plots of vertical velocity versus Voronoi area (Figures 5.4–5.6). The data points in the upper right corner of each plot—representing the subset of droplets used for the correction—are set to be identically zero at all three measurement stations.

Analysis of the Settling Velocity Enhancement

The main result from the settling velocity data is that, for all but the largest droplets, there is a clear trend between vertical velocity and Voronoi area. As the Voronoi areas decrease (local concentration increases), collective settling effects result in enhanced settling velocities. This trend is consistent at all three measurement stations, but it weakens slightly as droplet size increases corresponding to an increase in Stokes number above the value of 1. Assuming that the scatter in the data for the largest size bin is only the result of less-converged statistics due to a smaller number of droplet measurements, the droplets in this size-class exhibit a near-constant settling velocity across all Voronoi areas. This behavior can be interpreted as these largest droplets having $St \gg 1$ and, as a result, ballistic trajectories that make them

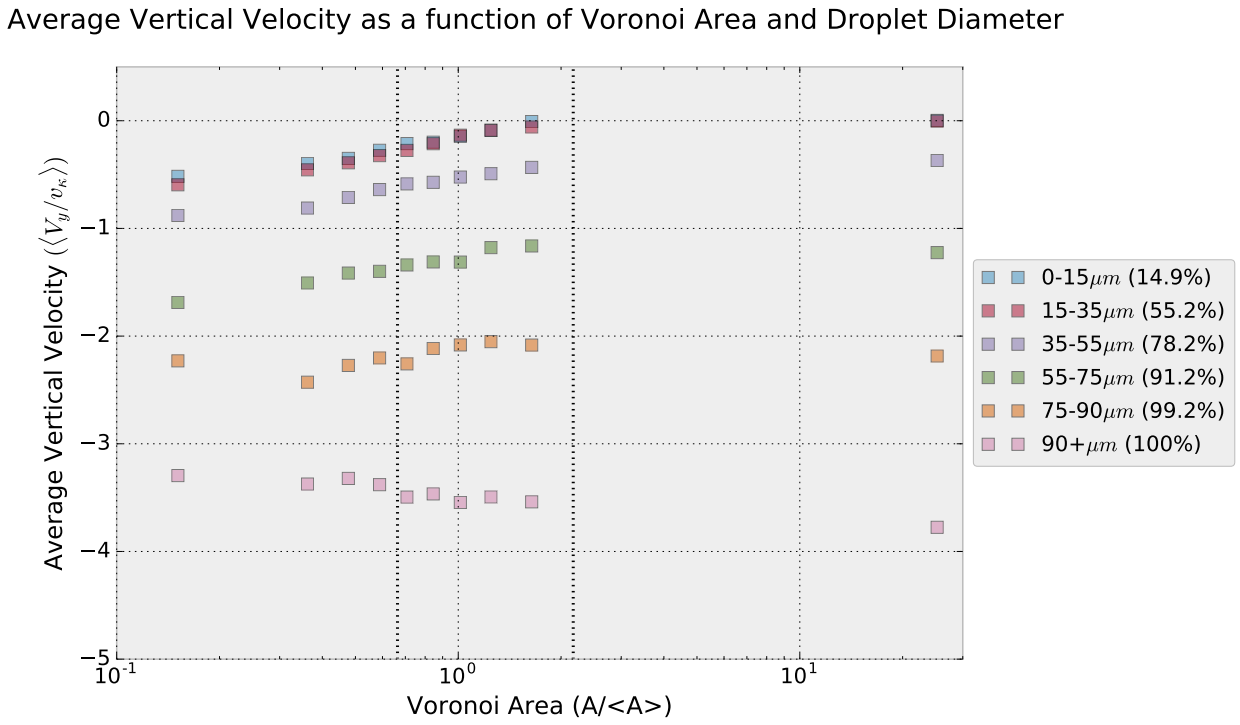

Figure 5.4: The average vertical velocity ($\langle V_y/v_\kappa \rangle$) at $x = 20$M plotted as a function of the normalized Voronoi area ($A/\langle A \rangle$) and the approximate droplet diameter. See Section 5.1.2 for a detailed discussion of how the droplet diameters are determined from the high-speed images. The two vertical dotted lines at $A/\langle A \rangle = 0.66$ and $A/\langle A \rangle = 2.17$ show the normalized Voronoi areas used as the cutoff to define clusters and voids. The droplets in the left-most region are in clusters, right-most are in voids, and droplets in the region in between the lines are in neither clusters nor voids.

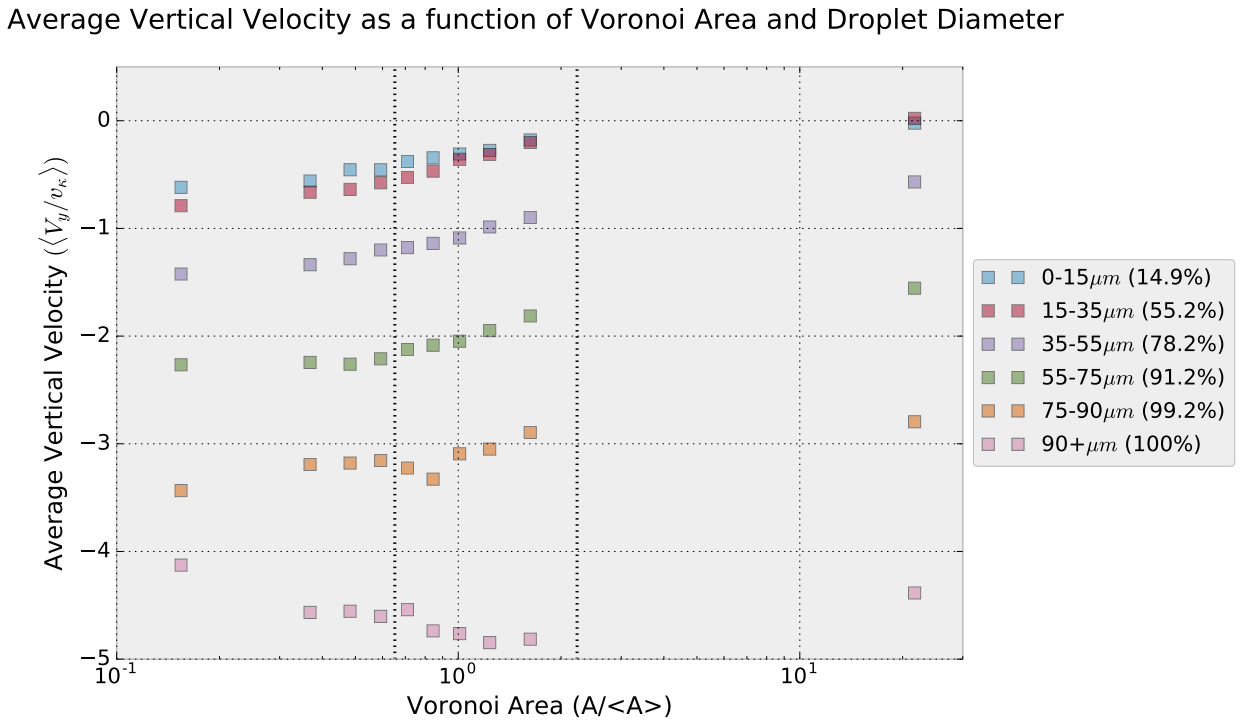

Figure 5.5: The average vertical velocity ($\langle V_y/v_\kappa \rangle$) at $x = 30$M plotted as a function of the normalized Voronoi area ($A/\langle A \rangle$) and the approximate droplet diameter. See Section 5.1.2 for a detailed discussion of how the droplet diameters are determined from the high-speed images. The two vertical dotted lines at $A/\langle A \rangle = 0.67$ and $A/\langle A \rangle = 2.23$ show the normalized Voronoi areas used as the cutoff to define clusters and voids. The droplets in the left-most region are in clusters, right-most are in voids, and droplets in the region in between the lines are in neither clusters nor voids.

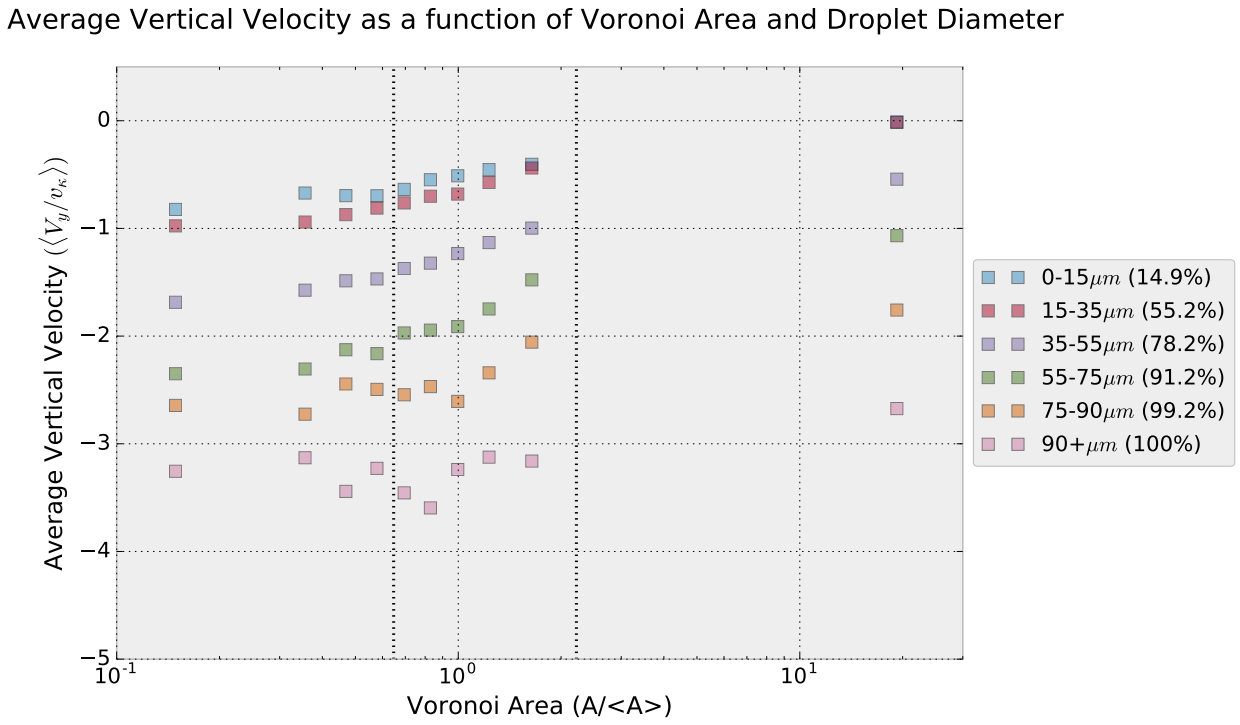

Figure 5.6: The average vertical velocity ($\langle V_y/v_\kappa \rangle$) at $x = 40$M plotted as a function of the normalized Voronoi area ($A/\langle A \rangle$) and the approximate droplet diameter. See Section 5.1.2 for a detailed discussion of how the droplet diameters are determined from the high-speed images. The two vertical dotted lines at $A/\langle A \rangle = 0.65$ and $A/\langle A \rangle = 2.22$ show the normalized Voronoi areas used as the cutoff to define clusters and voids. The droplets in the left-most region are in clusters, right-most are in voids, and droplets in the region in between the lines are in neither clusters nor voids.

less susceptible to influence from the turbulent fluctuations and less likely to be influenced by collective settling dynamics.

The dependency of these results on turbulence characteristics (as associated by the different wind tunnel downstream locations) is not straightforward. For the three smallest droplet size bins, the average vertical velocity, non-dimensionalized with the Kolmogorov velocity, increases as the flow moves downstream. This suggests that this behavior is has a cumulative effect, and is only partially related to the carrier fluid turbulent dissipation rate. The increase is stronger for the smallest Voronoi areas, suggesting that this cumulative effect over time is associated with droplet clustering. As the droplets continue to cluster together, or as they spend more time in a cluster experiencing the effects of the collective dynamics, the result is an increase in the average settling velocity with residence time in the wind tunnel (or downstream measurement location). As for the bins for larger-sized droplets, they exhibit some fluctuation in their behavior across the three measurement stations with no clear trends. The statistics conditioned to droplet size, droplet Voronoi area and turbulent dissipation rate are less converged as a result of a much smaller droplet-count in these bins.

5.2 Relative Velocities

5.2.1 Relative Velocity Calculation

The relative velocity statistics for the droplets are one of the most important components in the droplet collision kernel equation (Eq. (1.4)). These statistics are created by calculating the relative velocity vector between two droplets. Then, this vector is projected onto the radial separation vector between the droplet centers. The resulting signed scalar is the speed at which the two droplets are moving either towards or away from each other. This parameter is called the "closing speed" in this dissertation, but in the literature it is also sometimes referred to as the longitudinal relative velocity.

The algorithm that calculates the relative velocity statistics shares information with the

Radial Distribution Function (RDF) algorithm, described earlier, since the two algorithms have multiple expensive computational steps in common. The Relative Velocity algorithm first takes the X- and Y-coordinates, as well as the X- and Y-velocities, for all the droplets in a single image. Within this subset of positions and velocities at a given instant of time, it loops through each droplet and subtracts its velocity (or position) from the array of the corresponding variable for all the other droplets. For example, using P as a generic variable (that can represent either X, Y, U, or V) then $\delta\vec{P}_i = P_i - \vec{P}$. The resulting array of differences for a given particle i ($\delta\vec{P}_i$) is appended to the array of differences that includes the differences for all other droplets. At the end of the loop, the array $\delta\vec{P}$ contains all the possible differences between every pair of droplets in the image, twice. After removing the zeros resulting from the subtraction of the droplet variable from itself ($P_i - P_i$), the difference arrays can be used to calculate the separation distance,

$$\delta\vec{R} = \sqrt{\delta X^2 + \delta Y^2}, \tag{5.1}$$

and the closing speed,

$$\text{Closing Speed} \;=\; (\vec{V_2} - \vec{V_1}) \cdot \frac{\vec{r}_{21}}{|\vec{r}_{21}|} \;=\; \frac{\delta\vec{U}\delta\vec{X} + \delta\vec{V}\delta\vec{Y}}{\sqrt{\delta\vec{X}^2 + \delta\vec{Y}^2}}. \tag{5.2}$$

The closing speed is conditioned on the separation distance and the PDFs for each range of separation distances are plotted in Figures 5.7–5.9. The range of separation distances used to compute each PDF are given in the legend, along with the number of droplets in each range, to give a sense for the relative level of statistical convergence in each bin. The black dotted line is a Gaussian curve fit to the data from the largest separation distances (the last range from 5 to 10η).

5.2.2 Relative Velocity Analysis and Discussion

The relative velocity curves at small separations look like fluid accelerations. This is consistent with the interpretation that, at small separations, the velocity difference between two

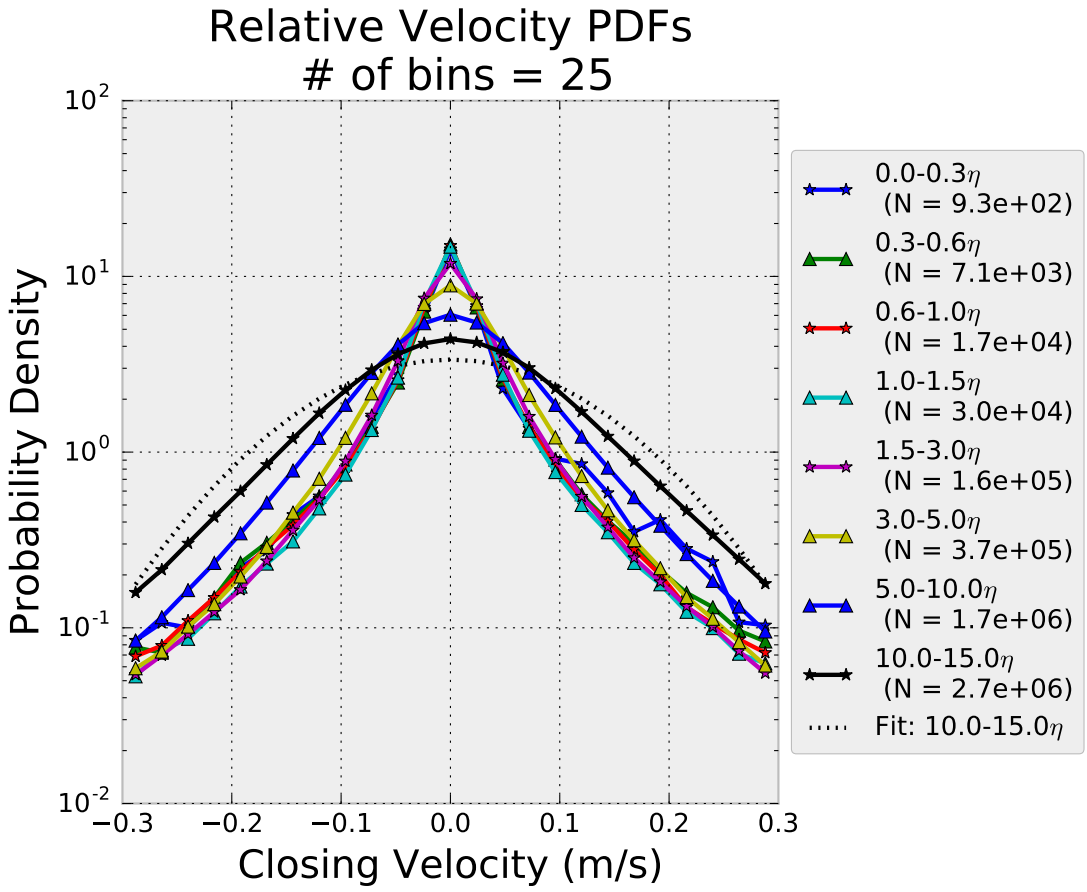

Figure 5.7: PDFs of the closing velocity at $x = 20$M. The various curves represent the different radial separation distance bins, non-dimensionalized with the Kolmogorov length (η). The range of separation distances used to compute each PDF curve is given in the legend, as well as the number of droplets (N) used to generate each curve. The black dotted line is a Gaussian distribution with the same standard deviation as the data from the largest separation distance range.

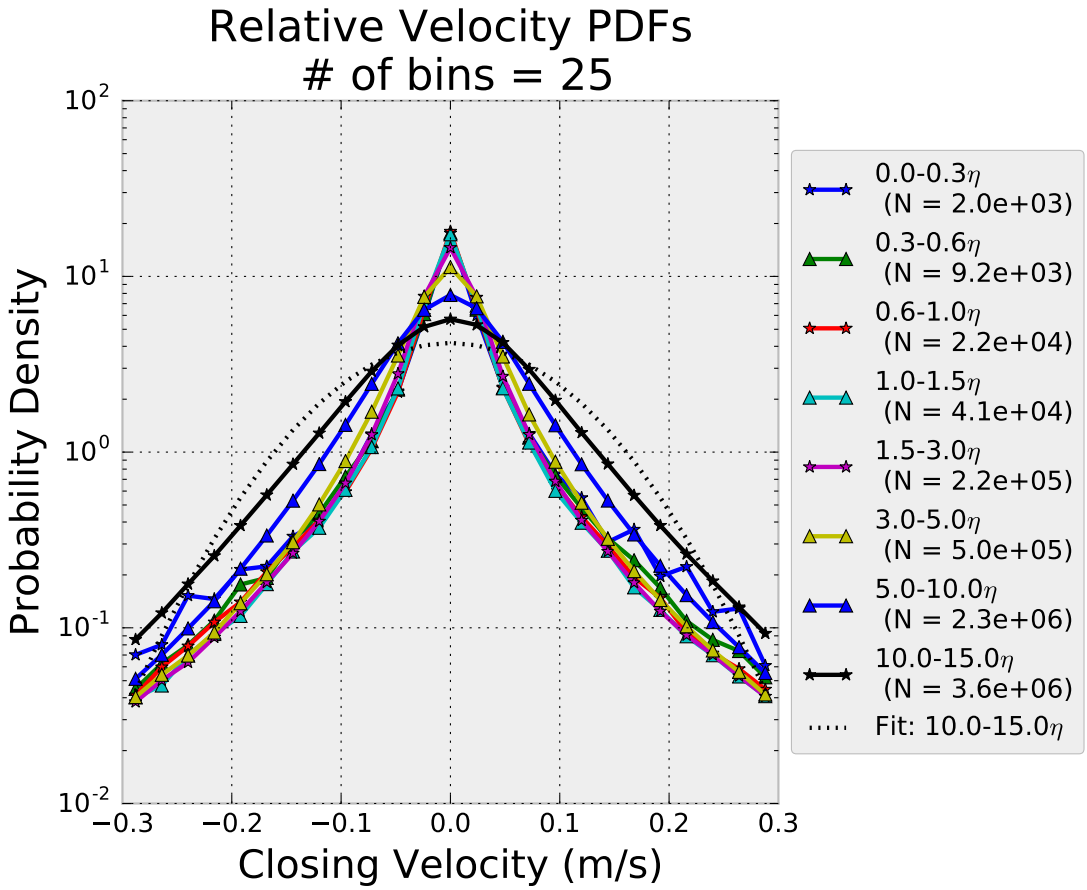

Figure 5.8: PDFs of the closing velocity at x = 30M. The various curves represent the different radial separation distance bins, non-dimensionalized with the Kolmogorov length (η). The range of separation distances used to compute each PDF curve is given in the legend, as well as the number of droplets (N) used to generate each curve. The black dotted line is a Gaussian distribution with the same standard deviation as the data from the largest separation distance range.

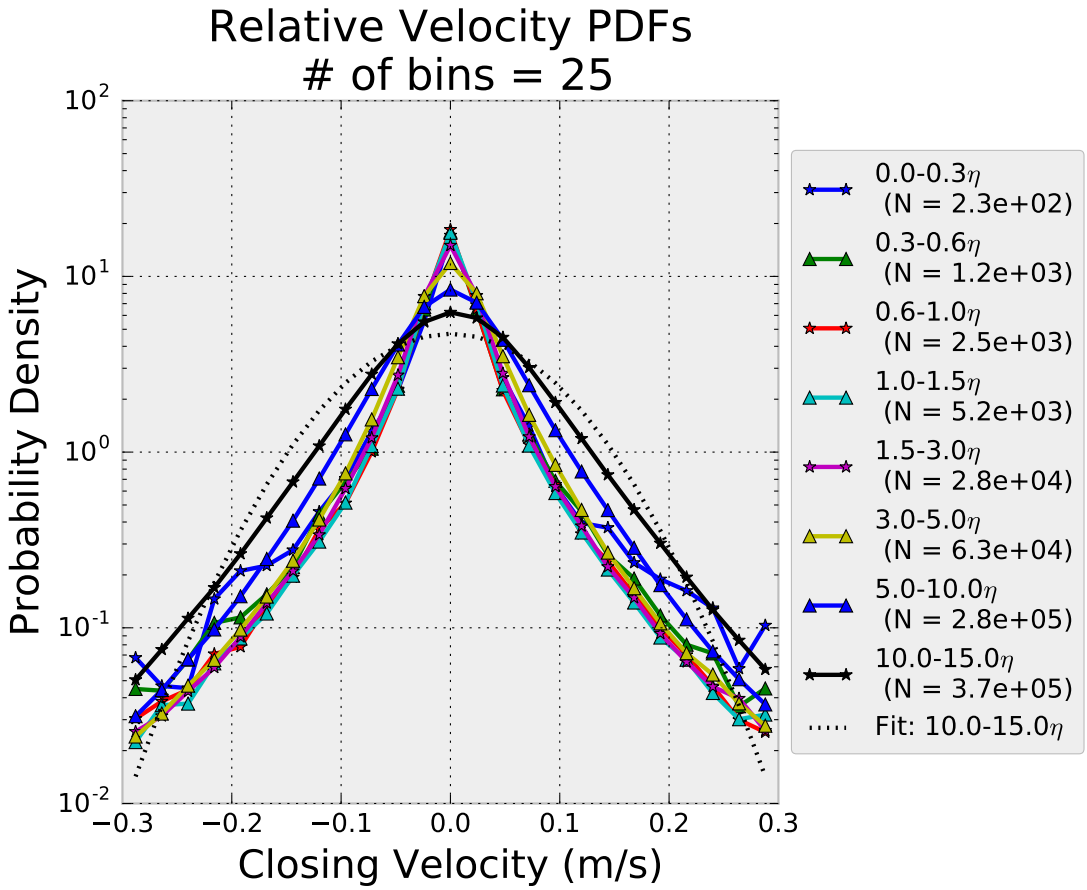

Figure 5.9: PDFs of the closing velocity at $x = 40$M. The various curves represent the different radial separation distance bins, non-dimensionalized with the Kolmogorov length (η). The range of separation distances used to compute each PDF curve is given in the legend, as well as the number of droplets (N) used to generate each curve. The black dotted line is a Gaussian distribution with the same standard deviation as the data from the largest separation distance range.

"points" is representative of the fluid acceleration experienced by a "point" as it crosses a small distance (in a small time interval). The important aspect to study is the deviation of the inertial particles studied in this dissertation from the behavior of fluid "particles".

At larger separations, the velocity differences tend towards a normal distribution, as can be seen in the way the curves start to align with the Gaussian distribution in the plot (black dotted line). This is because as the separation distance between the droplets increases, the influence of the presence of one on the velocity of the other decays quickly and the correlation in the velocity of the flow surrounding those two droplets decreases. The result is that the relative velocity between two uncorrelated droplets looks more like a random variable in the turbulent flow.

The relative velocity plots at the three different measurement stations all look similar. There is a noticeable narrowing of the distributions as the droplets move down the length of the tunnel that can be attributed to the result of two things: (1) the decreasing turbulence dissipation rate, with the corresponding reduction in the strength of the turbulent excitation of the droplet dynamics, and (2) the collective history of the droplets as they continue to cluster together, resulting in a homogenization of the droplet velocities as they interact with the same region of the same turbulent structures within the carrier fluid.

The relative velocity is one of the key parameters in the collision kernel. Thus, it is important to examine this variable's behavior in an effort to tease out the influence of the turbulence on the dynamics of particles leading to collisions. In the previous analysis of the raw data, the statistics of the relative velocity at short separations all collapse along the expected exponential decay of fluid Lagrangian acceleration. At large separation distances, the behavior diverges from that exponential decay and starts to resemble a Gaussian process, but this last set of curves does not correspond to droplets with a high probability of colliding. In order to understand the quantitative effect of the relative velocity statistics on the probability of droplet collisions, the seemingly trivial raw data had to be explored in

a different way. This new method for analyzing the droplet dynamics is based on a novel non-dimensional variable uncovered in this dissertation that we are naming "Closing Time".

5.2.3 Non-dimensional Closing Time

Background

While trying to interpret the relative velocity statistics, and looking for a way to differentiate between the behavior of particles at different separation distances, a new way to interpret the relative velocity data is proposed: the probability of two particles colliding depends on them having a large relative closing velocity and on them having a small separation distance. These two variables that appear in the classical formulation of the collision kernel, relative velocity and separation distance, are not independent parameters. The joint PDF of relative velocity and separation distance, shown in Figures 5.7–5.9, is almost uniform for a range of separation distances where the curves collapse. But two particles will undergo a collision if they have enough closing velocity to reduce their separation distance to zero (actually the sum of the radii, but for all practical purposes that value is negligible compared to the initial separation distance) before their relative velocity changes. This ratio of times—the time it takes for the particles to collide and the time it takes for the particles to change their velocity—is the key to whether a certain condition of relative velocity and separation distance results in a collision or not. This non-dimensional value, which has not been used before to describe collisions, is what we are calling the Closing Time.

The time-to-collision, τ_c is computed as follows:

$$\mathrm{Time-to-Collision} = \frac{\mathrm{Separation\,Distance}}{\mathrm{Closing\,Speed}}$$

$$\tau_c = \frac{|\vec{r}_{21}|}{(\vec{V}_2 - \vec{V}_1) \cdot \frac{\vec{r}_{21}}{|\vec{r}_{21}|}}$$

$$\tau_c = \frac{r^2}{(\vec{V}_2 - \vec{V}_1) \cdot \vec{r}_{21}} \tag{5.3}$$

To non-dimensionalize τ_c, the particle viscous relaxation time is chosen because it represents the time a particle at low Reynolds number will maintain the same velocity before changing in response to changes in the surrounding fluid velocity. In order to measure a non-zero relative velocity between two droplets that will lead to a collision, at least one of those droplets' velocity must deviate significantly from the local fluid flow. Relative velocities can exist between two flow-tracing droplets, but if they behave like perfect flow tracers in an incompressible flow, then the continuity equation ensures that they would never collide. For a droplet that is moving relative to its carrier fluid, the drag on the droplet is always working to return the droplet to the local flow velocity. A collision must occur before any velocity difference decays back to zero. The right time scale to characterize this relaxation process is the droplet (or particle) viscous relaxation time (τ_p). Thus, it makes sense to relate the time-to-collision with this parameter that characterizes the inertia of the particles, providing a clear threshold to determine collisions: droplets with negative closing times are moving towards each other, and if the ratio between the particle relaxation time and closing time is greater than 1.0, then the droplets will close their separation distance before their velocities relax back to that of the carrier fluid. The Non-Dimensional Closing Time PDFs are shown in Figures 5.10–5.12, with each curve representing the probability of finding particles with different relative velocities at different separation distance ranges.

The particle viscous relaxation time is calculated for the arithmetic-mean droplet diameter from the droplet distribution. Lacking specific information about the sizes of the droplet measured via PTV, the mean diameter value is the best representation of the inertia of the droplet distribution to create a non-dimensional closing time, even though it does not capture the size-specific behavior for individual droplets. The influence of particle size on the Closing Time ratio needs to be the subject of future measurements.

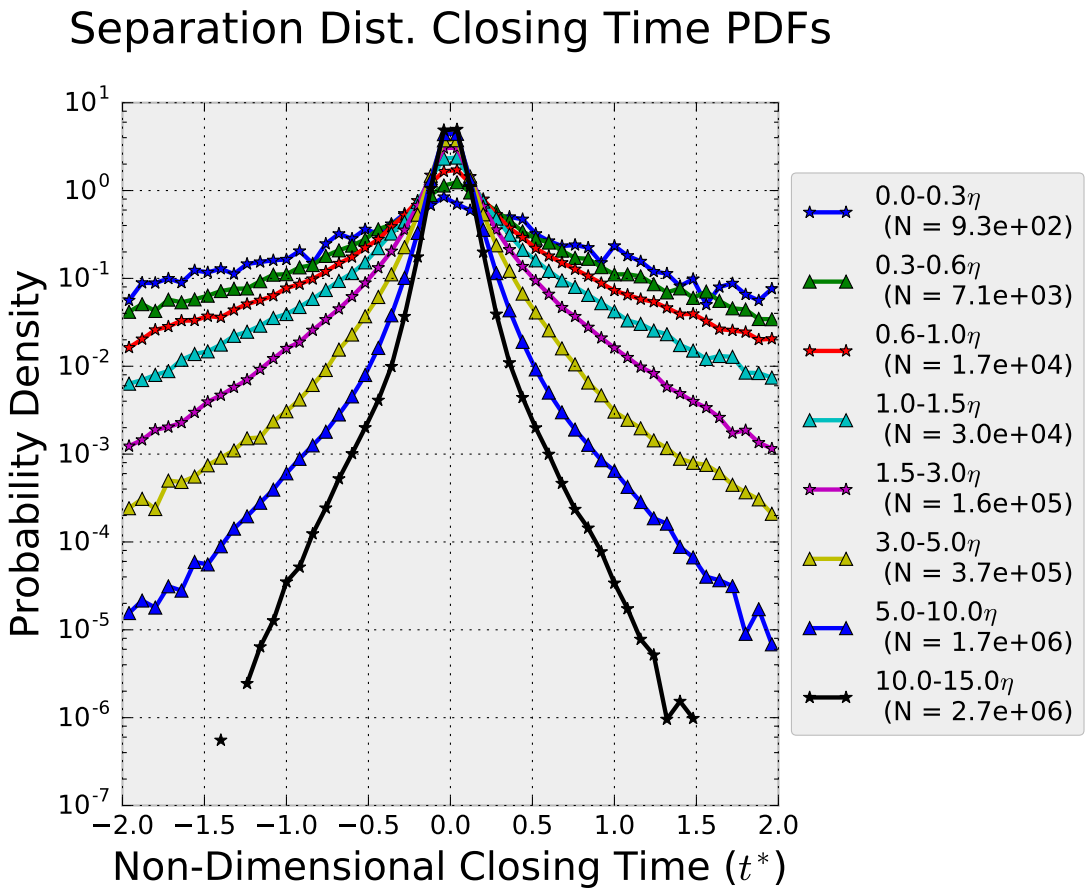

Figure 5.10: PDFs of the Non-dimensional Closing Time (t^*) at $x = 20$M. $t^* \equiv \tau_p/\tau_c$. τ_p is the particle relaxation time (Eq. (1.2)). τ_c is the closing time (Eq. (5.3)). Each curve represents a different radial separation distance bin. The legend shows the range of each bin measured in multiples of the Kolmogorov length (η), as well as the number of droplets (N) used to generate each curve. Droplet pairs with closing times smaller (more negative) than -1.0 will close the distance separating them within one particle relaxation time.

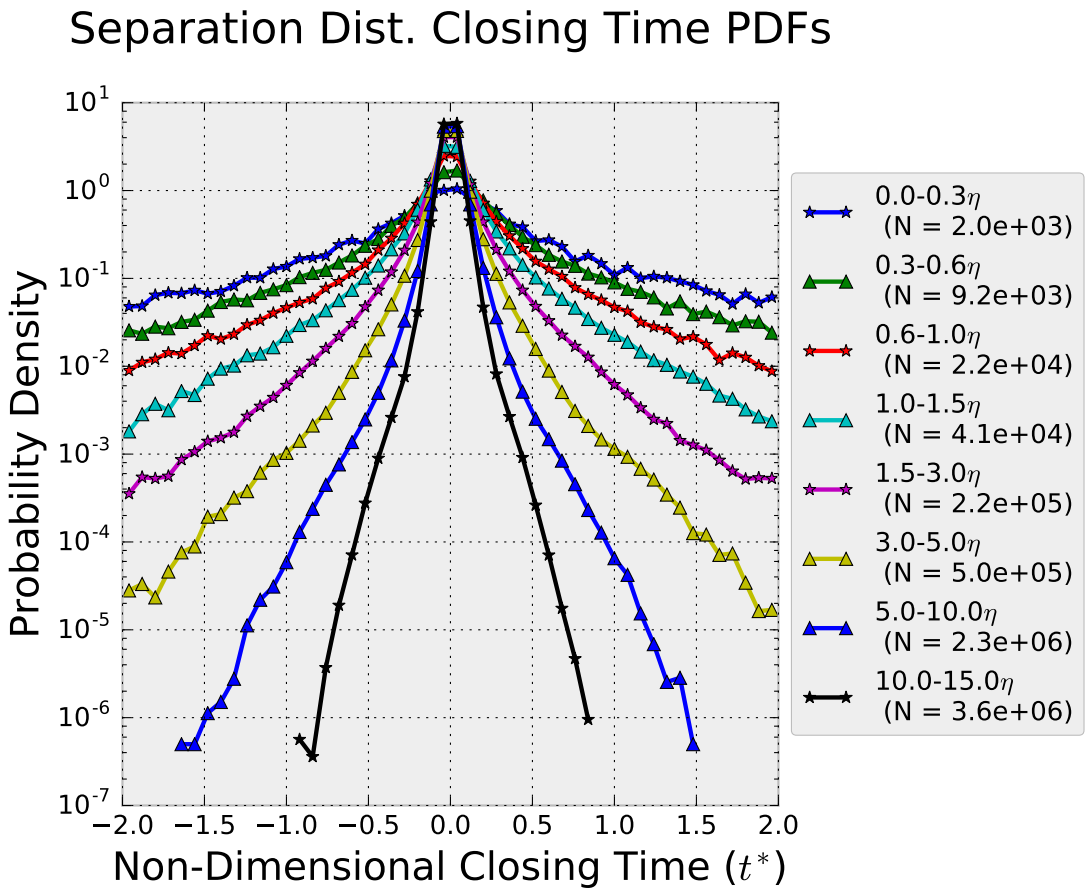

Figure 5.11: PDFs of the Non-dimensional Closing Times (t^*) at x = 30M. $t^* \equiv \tau_p/\tau_c$. τ_p is the particle relaxation time (Eq. (1.2)). τ_c is the closing time (Eq. (5.3)). Each curve represents a different radial separation distance bin. The legend shows the range of each bin measured in multiples of the Kolmogorov length (η), as well as the number of droplets (N) used to generate each curve. Droplet pairs with closing times smaller (more negative) than -1.0 will close the distance separating them within one particle relaxation time.

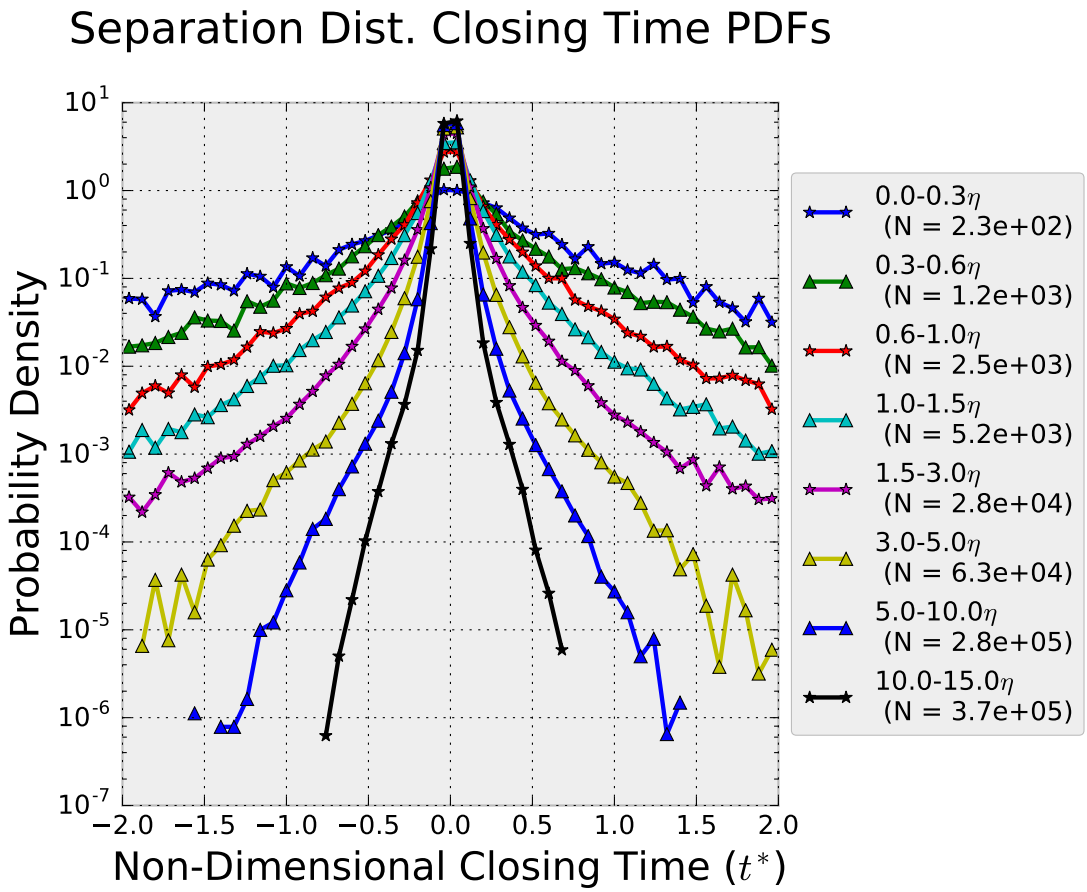

Figure 5.12: PDFs of the Non-dimensional Closing Times (t^*) at $x = 40$M. $t^* \equiv \tau_p/\tau_c$. τ_p is the particle relaxation time (Eq. (1.2)). τ_c is the closing time (Eq. (5.3)). Each curve represents a different radial separation distance bin. The legend shows the range of each bin measured in multiples of the Kolmogorov length (η), as well as the number of droplets (N) used to generate each curve. Droplet pairs with closing times smaller (more negative) than -1.0 will close the distance separating them within one particle relaxation time.

Analysis and Discussion of the Closing Time Ratio

There is a monotonic increase in the probability of the closing time with decreasing separation distance, as expected, because droplets that are closer together are more likely to collide within the span of the particle relaxation time. In this regard, the Closing Time ratio provides a physical interpretation of the measurements of relative velocity that is not obvious from the collapse of the relative velocity PDFs for all the small separation distances. Despite this apparent lack of correlation between the separation distance and the relative velocity, the Closing Time PDFs show that the collision probability does depend strongly on the joint PDF. Once the joint PDF is re-framed in the correct non-dimensional ratio, it provides a more meaningful representation of the droplet inertial dynamics in turbulence. But beyond this qualitative understanding, the main benefit of the Closing Time statistics is that they can be used to compute collision probabilities from experimentally measurable quantities, separation distance and relative velocity, at finite separations. This is a significant contribution to understanding and quantifying inertial particle dynamics leading to collisions. For instance, this makes estimating collision probabilities significantly easier than using the collision equation (1.4) proposed by Sundaram and Collins, which requires the Radial Distribution Function at contact and the full Relative Velocity PDFs.

To relate the Closing Time statistics to a collision probability, one would evaluate the double integral along each of the separation distance curves from -1.0 to $-\infty$, and for all separation curves from $R = 0\eta$ to ∞ (with the contribution of the integrals for the different separation distances decaying with increasing separation so that only a few of the integrals for the smaller separation distances need to be computed),

$$\int_{R_j}^{R_i} \int_{-\infty}^{-1} P(\tau_c|R)\, d\tau_c\, dR$$

as an alternative to

$$\int \mathbf{w}\, P(\mathbf{w}\,|\,\sigma) d\mathbf{w}$$

from Sundaram and Collins's collision equation.

The first integration is easy to calculate with experimentally measured data, especially compared to evaluating the relative velocity of two droplets at that negligible separation distance that occurs at the moment of contact. That is a mathematical construct that simply does not materialize in experiments and is all but impossible to measure in statistically significant numbers. Even trying to approximate this second expression would be difficult, requiring large data sets to get statistically meaningful measurements of such rare events.

Horizontal vs. Vertical Closing Time Results

The Closing Time PDFs from both the vertical and horizontal plane visualizations collected at 30M are compared and negligible differences between the curves were found. The curves for the separations between $3\eta - 10\eta$ show some deviation from each other at larger closing times. This can be attributed to the slight difference in the turbulent dissipation rate measured at the 30M Vertical and 30M Horizontal measurement locations (cf. Figure 2.11 in Section 2.2.4). As will be described in more detail in the next paragraph, there is a definite relationship between the closing time PDFs and the carrier fluid turbulence.

Closing Time Dependence on Turbulence Characteristics

The Closing Time plots from the three measurement stations (Figure 5.14) all have similar shapes, but there is a noticeable narrowing of the distributions as the flow moves down the tunnel. Only a subset of the separation distance curves are included in the plot to keep the data from obscuring the results from these measurements.

When plotted on the same axes, the differences between the data at different turbulence characteristics (measurement stations inside the wind tunnel) are clearly apparent. There is

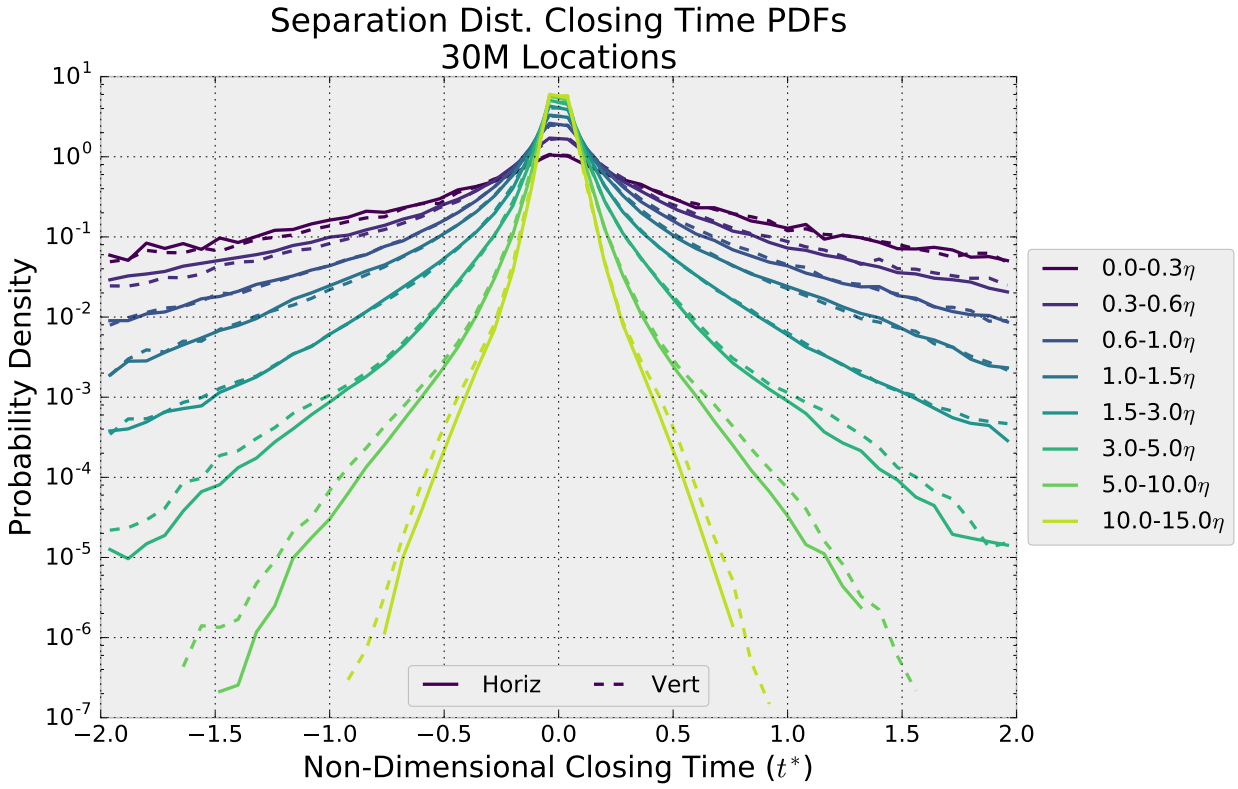

Figure 5.13: PDFs of the Non-dimensional Closing Time (t^*) at x = 30M from both the horizontal (—) and vertical (- -) PTV measurement locations. $t^* \equiv \tau_p/\tau_c$. τ_p is the particle relaxation time (Eq. (1.2)). τ_c is the Closing Time (Eq. (5.3)). Curves with the same color are for the same radial separation distance bin. The legend shows the range of each bin measured in multiples of the Kolmogorov length (η). Droplet pairs with Closing Times smaller (more negative) than -1.0 will close the distance separating them within one particle relaxation time.

a monotonic trend for the PDFs to decrease as the turbulence dissipation rate decreases, and it is consistent for all the separation distance ranges. However, as the separation distance increases, the curves from the two most downstream stations (30M and 40M) are much closer together than they are to the 20M curves. This suggests that the physical mechanism creating separation between the curves is influenced by a length scale that is changing along the length of the tunnel. The most obvious candidate is the Komogorov length scale (η), which increases as the turbulence dissipation rate (ε) decreases. Figure 5.14 shows the influence of turbulence on droplet collision probability, and the working hypothesis in this dissertation is that, as the strength of the turbulence decreases, the collision probabilities also decrease. There is a physical value for the controlling length scale that dominates the inertial particle dynamics, outside of which the decrease in turbulence has a negligible effect on the collision probability. Figure 5.14 shows conclusively that collision probabilities are a function of turbulent dissipation rate.

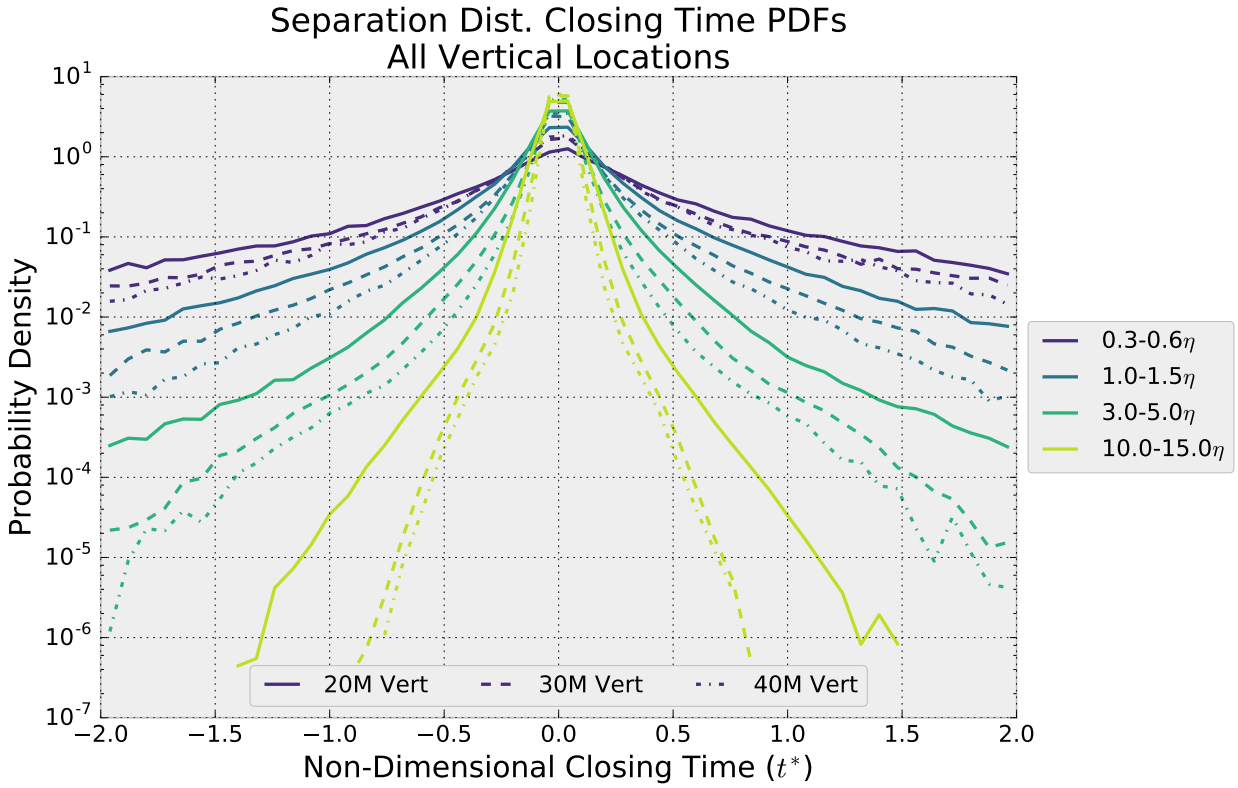

Figure 5.14: PDFs of the Non-dimensional Closing Time (t^*) from all three measurement stations: x = 20M (—), 30M (- -), and 40M (-.-). $t^* \equiv \tau_p/\tau_c$. τ_p is the particle viscous relaxation time (Eq. (1.2)). τ_c is the Closing Time (Eq. (5.3)). Curves with the same color are for the same radial separation distance bin. The legend shows the range of each bin measured in multiples of the Kolmogorov length (η). Droplet pairs with closing times smaller (more negative) than -1.0 will close the distance separating them within one particle relaxation time.

Chapter 6

CONCLUSIONS

An experimental wind tunnel facility has been created to measure droplet dynamics using PDPA and PTV. PDPA measurements of the disperse phase are used to demonstrate that the tunnel test section is seeded with a homogeneous spatial distribution of droplets with sizes appropriate for studying inertial dynamics relevant to warm-rain formation. The carrier fluid phase is characterized using hotwire anemometry and Pitot rake measurements. The linear decay of the turbulence intensity shows that the carrier phase behaves like homogeneous isotropic turbulence and the well-defined inertial range in the turbulent energy spectra highlights the high Reynolds number character of the laboratory flow; not quite matching the Reynolds number of a cumulus cloud (ranging up to $\mathrm{Re}_\lambda = 10,000$), but definitely approaching the asymptotic regime. To overcome an undesirably non-homogeneous velocity profile in the test section, a wall jet system was designed and installed that successfully modified the tunnel's velocity profile. The resulting flow has nearly uniform streamwise velocities and turbulence intensities in the entire region where measurements are collected. The velocity profiles are shown to be uniform to within $\pm 8\%$ of the mean velocity over more than 80% the width of the tunnel cross-section; an improvement over the the previous result in the original wind tunnel design where a $\pm 14\%$ variation about the mean freestream velocity occurred over less than 50% of the tunnel cross-section.

To measure the droplet dynamics, high-speed images are taken of the two-phase flow in the tunnel. These images are successfully corrected for a sensitivity bias in the camera sensor so that the number of particles detected is uniform throughout the measurement area, and thus consistent with the uniformity of seeding confirmed by the PDPA. A new 4-frame N+2

PTV algorithm is implemented to link droplet coordinates across multiple high-speed images into droplet trajectories through the imaging field of view. Spline fits to the coordinates allow for the calculation of smooth derivatives of droplet positions. The resulting velocities successfully match the velocities measured via two different independent techniques (HWA and Pitot tube measurements).

Both 1D and 2D radial distribution functions are calculated to analyze droplet preferential concentration. Calculated using PDPA data, the 1D RDFs show that the droplets accumulate in close proximity to each other due to the turbulence. The length scale of this accumulation relates to the Kolmogorov scale of the carrier flow, but extends out to separations on the order of the integral length scale of the turbulence. The peak of the RDF is measured at the smallest separation, close to the diameter of the droplets (where two droplets would collide at the distance equal to the sum of their radii). This peak is the key measure of the radial distribution function that links preferential concentration of droplets by turbulence to the collision kernel. The RDF evaluated at contact, which can only be calculated by extrapolating the RDF computed from large separations to a value below the Kolmogorov scale (η), is proportional to the collision rate and shows the significant enhancement of the collision probability due to turbulence. The RDFs presented in this dissertation extend previous results of inertial droplet clustering at scales around 10η to much larger Re_λ and lower turbulent dissipation rates—a parameter range more representative of cloud conditions. Notably, the RDF does not decay to a value of 1 until it is calculated for separations on the order of the integral length scale (approximately 2000η) at this Reynolds number. This is in conflict with some previous experimental measurements of the (2D) RDF, but fully consistent with the view that preferential accumulation for a polydisperse particle population occurs throughout the inertial range and thus the purely random spatial distribution is recovered only at lengths larger than any correlation length of the turbulence.

The 2D RDFs calculated from high-speed images of the flow show a consistent trend

where the RDFs from the horizontal imaging configurations were all lower than those from the vertical configurations. This result agrees with the intuition that clusters of inertial particles under the effect of gravity are not isotropic and that particles accumulate on the downward side of eddies. This observation that the 2D RDF is sensitive to orientation is likely the first experimental evidence that clustering is stronger in the direction of gravity and that gravity does indeed play a role in the concentration of inertial particles.

Droplet settling velocities are conditioned on Voronoi areas to assess the relationship between settling and local droplet concentration. The main result from the settling velocity data is that for all but the largest droplets, there is a clear trend between the vertical velocity and Voronoi area. As the Voronoi areas decrease (local concentration increases), collective settling effects result in enhanced settling velocities. The dependency of these results on turbulence characteristics is not straightforward. The settling velocity increases for only the three smallest droplet size bins as the flow moves downstream, suggesting that this behavior is only partially caused by the carrier fluid turbulence. The increase is stronger for the smallest Voronoi areas, suggesting that this trend is related to droplet clustering. As the droplets continue to cluster together, or as they spend more time in a cluster experiencing the effects of the collective dynamics, the result is an increase in the average settling velocity with residence time in the wind tunnel (or downstream measurement location), even if the turbulent dissipation rate decays along the trajectories.

The non-dimensional Closing Time ratio is proposed as a new way to interpret droplet relative velocity data that incorporates the fact that the probability of having two particles collide depends on them having both a large relative closing velocity and a small separation distance. The Closing Time shows that once the relative velocity joint PDF is re-framed in the correct non-dimensional ratio, it provides a more meaningful representation of the inertial droplet dynamics. For example, there is a monotonic trend for the PDFs to decrease as the turbulence dissipation rate decreases, and it is consistent for all the separation distance

ranges. This shows the influence of turbulence on droplet collision probability, whereby as the strength of the turbulence decreases, the collision probabilities also decrease. However, as the separation distance increases, the decrease in collision probability is less pronounced. This suggests that there is a physical value for the controlling length scale that dominates the inertial particle dynamics, outside of which, the decay of the turbulence intensity and dissipation rate have a negligible effect on the collision probability.

Beyond this ability to provide qualitative understanding, the main benefit of the Closing Time statistics is that they can be used to compute collision probabilities from experimentally measurable quantities of separation distance and relative velocity measured at finite separations. This is a significant and novel contribution to understanding and quantifying inertial particle dynamics leading to collisions.

BIBLIOGRAPHY

H.-E. Albrecht. *Laser Doppler and phase Doppler measurement techniques.* Experimental fluid mechanics. Springer, Berlin; New York, 2003.

A. Aliseda, F. Hainaux, A. Cartellier, and J.C. Lasheras. Effect of preferential concentration on the settling velocity of heavy particles in homogeneous isotropic turbulence. *J. Fluid Mech.*, 468:77–105, 2002.

D. Arenberg. Turbulence as the major factor in the growth of cloud drops. *Bull. Am. Meteorol. Soc.*, 20:444–448, 1939.

O. Ayala, B. Rosa, L.-P. Wang, and W. W. Grabowski. Effects of turbulence on the geometric collision rate of sedimenting droplets. Part 1. Results from direct numerical simulation. *New J. Phys.*, 10(7):075015–+, July 2008.

W.D. Bachalo. Experimental methods in multiphase flows. *Int. J. Multiphase Flow*, 20 (Suppl):261–295, 1994.

C.P. Bateson. The radial distribution function as a quantication of the preferential concentration of cloud droplets in a turbulent flow. Master's thesis, University of Washington, 2010.

C.P. Bateson and A. Aliseda. Wind tunnel measurements of the preferential concentration of inertial droplets in homogeneous isotropic turbulence. *Exp. Fluids.*, 52:1373–1387, 2012. doi: 10.1007/s00348-011-1252-6.

S. Corrsin. Turbulence: Experimental methods. In S. Flugge and C.A. Truesdall, editors, *Handbuch der Physik*, volume VIII, pages 524–590. Springer-Verlag, Berlin, 1963.

F. C. de Almeida. The collision problem of cloud droplets moving in a turbulent environment. part i: A method of solution. *J. Atmospher. Sci.*, 33:1571–1578, 1976.

F. C. de Almeida. The collision problem of cloud droplets moving in a turbulent environment. part ii: Turbulent collision efficiencies. *J. Atmospher. Sci.*, 36:1564–1576, 1979a.

F. C. de Almeida. The effects of small-scale turbulent motions on the growth of a cloud droplet spectrum. *J. Atmospher. Sci.*, 36:1557–1563, 1979b.

T.W.R. East and J.S. Marshall. Turbulence in clouds as a factor in precipitation. *Q. J. R. Meteorol. Soc.*, 80:26–47, 1954.

J.K. Eaton and J.R. Fessler. Preferential concentration of particles by turbulence. *Int. J. Multiphase Flow*, 20(Suppl):169–209, 1994.

J. Ferenc and Z. Néda. On the size distribution of poisson voronoi cells. *Physica A*, 385(2): 518 – 526, 2007. ISSN 0378-4371.

M. Gad-el Hak and S. Corrsin. Measurements of the nearly isotropic turbulence behind a uniform jet grid. *J. Fluid Mech.*, 62, part 1:115–143, 1974.

W.K. George, P.D. Beuther, and J.L. Lumley. Processing of random signals. *Proc. Dynamic Flow Conf.*, 1978.

R.J. Goldstein, editor. *Fluid Mechanics Measurements*. Taylor & Francis, Washington, D.C., 2nd edition, 1996.

S.N. Grover and H. R. Pruppacher. The effect of vertical turbulent fluctuations in the atmosphere on the collection of aerosol particles by cloud drops. *J. Atmospher. Sci.*, 42: 2305–2318, 1985.

G.L. Holtzer and L.R. Collins. Relationship between the intrinsic radial distribution function for an isotropic field of particles and lower-dimensional measurements. *J. Fluid Mech.*, 459: 93–102, 2002.

A. P. Khain and M. B. Pinsky. Drop inertia and its contribution to turbulent coalescence in convective clouds. part I: Drop fall in the flow with random horizontal velocity. *J. Atmospher. Sci.*, 52:192–204, 1995.

A. P. Khain and M. B. Pinsky. Turbulence effects on the collision kernel. II: Increase of the swept volume of colliding drops. *Q. J. R. Meteorol. Soc.*, 123:1543–1560, 1997.

A. N. Kolmogorov. Dissipation of energy in the locally isotropic turbulence. *Dokl. Akad. Nuak. SSSR*, 31:538–540, 1941.

I. Langmuir. The production of rain by a chain reaction in cumulus clouds at temperatures above freezing. *J. Atmospher. Sci.*, 5(5):175–192, 1948.

B. J. Lázaro and J.C. Lasheras. Particle dispersion in the developing free shear layer. part 1. unforced flow. *J. Fluid Mech.*, 235:143–178, 1992.

J.L. Lumley. Interpretation of time spectra measured in high-intensity shear flows. *Phys. Fluids*, 8(6):1056–1062, 1965.

M.R. Maxey. The motion of small spherical particles in a cellular flow field. *Phys. Fluids*, 30(4):1915–1928, 1987a.

M.R. Maxey. The gravitational settling of aerosol particles in homogeneous turbulence and random flow fields. *J. Fluid Mech.*, 174:441–465, 1987b.

M.R. Maxey and S. Corrsin. Gravitational settling of aerosol particles in randomly oriented cellular flows. *J. Atmospher. Sci.*, 43:1112–1134, 1986.

M.R. Maxey and J.J. Riley. Equation of motion for a small rigid sphere in a nonuniform flow. *Phys. Fluids*, 26(4):883–889, 1983.

R. Monchaux, M. Bourgoin, and A. Cartellier. Preferential concentration of heavy particles: A voronoi analysis. *Phys. Fluids*, 22(10), 2010.

N.T. Ouellette, H. Xu, and E. Bodenschatz. A quantitative study of three-dimensional lagrangian particle tracking algorithms. *Exp. Fluids.*, 40(2):301–313, 2006.

M.B. Pinsky and A.P. Khain. Turbulence effects on the collision kernel. I: Formation of velocity deviations of drops falling within a turbulent three-dimensional flow. *Q. J. R. Meteorol. Soc.*, 123:1517–1542, 1997.

M.B. Pinsky, A.P. Khain, and M. Shapiro. Turbulence effects on droplet growth and size distribution in clouds - a review. *J. Aerosol Sci.*, 28:1177–1214, 1997.

M.B. Pinsky, A.P. Khain, and M. Shapiro. Collisions of small drops in a turbulent flow. part I: Collision efficiency. problem formulation and preliminary results. *J. Atmospher. Sci.*, 56 (15):2585–2600, 1999.

M.B. Pinsky, A.P. Khain, and M. Shapiro. Stochastic effects of cloud droplet hydrodynamic interaction in a turbulent flow. *Atm. Res.*, 53(1-3):131–169, 2000.

M.B. Pinsky, M. Shapiro, and A.P. Khain. Collision efficiency of drops in a wide range of Reynolds numbers: Effect of pressure on spectrum evolution. *J. Atmospher. Sci.*, 58(17): 742–764, 2001.

S.B. Pope. *Turbulent Flows*. Cambridge University Press, Cambridge, 2006.

W.C. Reade and L.R. Collins. Effect of preferential concentration on turbulent collision rates. *Phys. Fluids*, 12(10):2530–2540, 2000.

G. W. Reuter, R. de Villiers, and Y. Yavin. The collection kernel for two falling cloud drops subjected to random perturbations in a turbulent air flow: A stochastic model. *J. Atmospher. Sci.*, 45:765–773, 1988.

G. W. Reuter, C. J. Wright, and D. Eyre. Effects of turbulence on the growth of a cloud drop spectrum. *J. Atmospher. Sci.*, 46:1407–1410, 1989.

P.G. Saffman and J.S. Turner. On the collision of drops in turbulent clouds. *J. Fluid Mech.*, 1:16–30, 1956.

E.W. Saw. *Studies of spatial clustering of inertial particles in turbulence*. PhD thesis, Michigan Technical University, 2008.

E.W. Saw, J. PLC Salazar, L.R. Collins, and R.A. Shaw. Spatial clustering of polydisperse inertial particles in turbulence: I. comparing simulation with theory. *New J. Phys.*, 14 (10):105030, 2012.

K.D. Squires and J.K. Eaton. Particle response and turbulence modification in isotropic turbulence. *Phys. Fluids*, 2(7):1191–1203, 1990.

S. Sundaram and L.R. Collins. Collision statistics in an isotropic particle-laden turbulent suspension. part 1. direct numerical simulations. *J. Fluid Mech.*, 335:75–109, 1997.

G.I. Taylor. Diffusion by continuous movements. *Proc. R. Soc. Lond. A*, 20:196–211, 1921.

G.I. Taylor. The spectrum of turbulence. *Proc. R. Soc. Lond. A*, 164(919):476–490, 1938.

C. Tropea, A.L. Yarin, and J.F. Foss, editors. *Springer Handbook of Experimental Fluid Mechanics*. Springer Berlin Heidelberg, Berlin, Heidelberg, 2007.

P. A. Vaillancourt and M. K. Yau. Review of particle-turbulence interactions and consequences for cloud physics. *Bull. Am. Meteorol. Soc.*, 81:285–298, 2000.

M. van Dyke. Higher-order boundary-layer theory. *Ann. Rev. Fluid Mech.*, 1(1):265–292, 1969.

L.-P. Wang, O. Ayala, B. Rosa, and W. W. Grabowski. Turbulent collision efficiency of heavy particles relevant to cloud droplets. *New J. Phys.*, 10(7):075013–+, July 2008.

L.P. Wang and M.R. Maxey. Settling velocity and concentration distribution of heavy particles in homogeneous isotropic turbulence. *J. Fluid Mech.*, 256:27–68, 1993.

L.P. Wang, A.S. Wexler, and Y. Zhou. Statistical mechanical description and modelling of turbulent collision of inertial particles. *J. Fluid Mech.*, 415:117–153, 2000.

L.P. Wang, O. Ayala, S.E. Kasprzak, and W.W. Grabowski. Theoretical formulation of collision rate and collision efficiency of hydrodynamically interacting cloud droplets in turbulent atmosphere. *J. Atmospher. Sci.*, 62(7):2433–2450, 2005.

L.P. Wang, Y. Xue, O. Ayala, and W.W. Grabowski. Effects of stochastic coalescence and air turbulence on the size distribution of cloud droplets. *Atm. Res.*, 82:416–432, 2006.

M.R. Wells and D.E. Stock. The effect of crossing trajectories on the dispersion of particles in a turbulent flow. *J. Fluid Mech.*, 136:31–62, 1983.

Y. Zhou, A.S. Wexler, and L.P. Wang. Modelling turbulent collision of bidisperse inertial particles. *J. Fluid Mech.*, 433:77–104, 2001.

Appendix A

ADDITIONAL SETTLING VELOCITY PLOTS

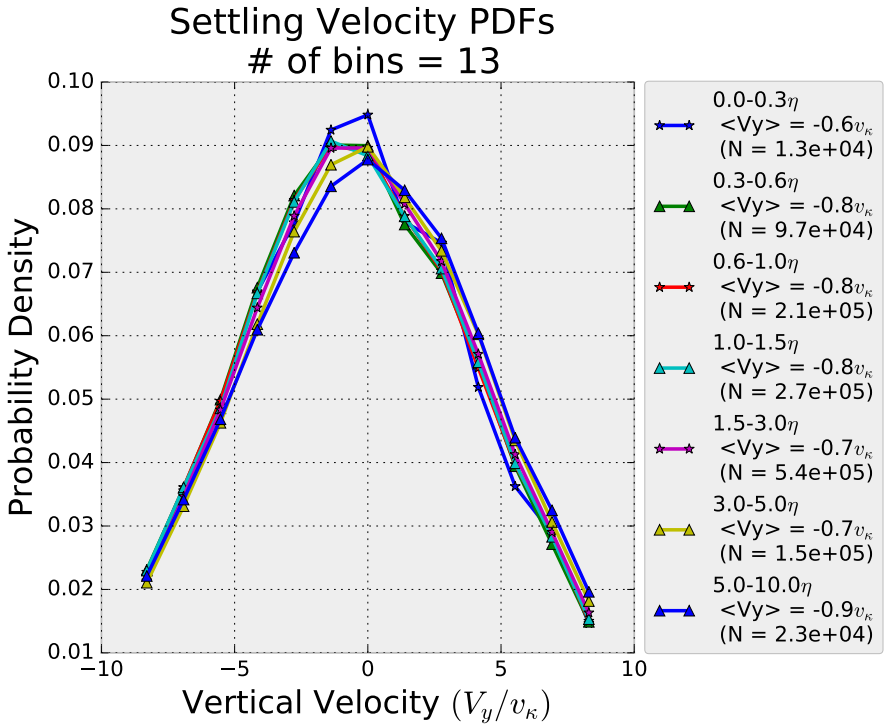

Figure A.1: Settling velocity Probability Density Functions (PDF) measured at $x = 20$M. The PDFs are plotted as a function of vertical velocity (V_y) scaled by the Kolmogorov velocity (v_κ). The data is binned according to distance to the nearest neighboring droplet measured in multiples of the Kolmogorov length (η). The legend shows the the number (N) of droplets in the bin, as well as the mean velocity ($\langle V_y \rangle$), in therm of the Kolmogorov velocity, for all those droplets.

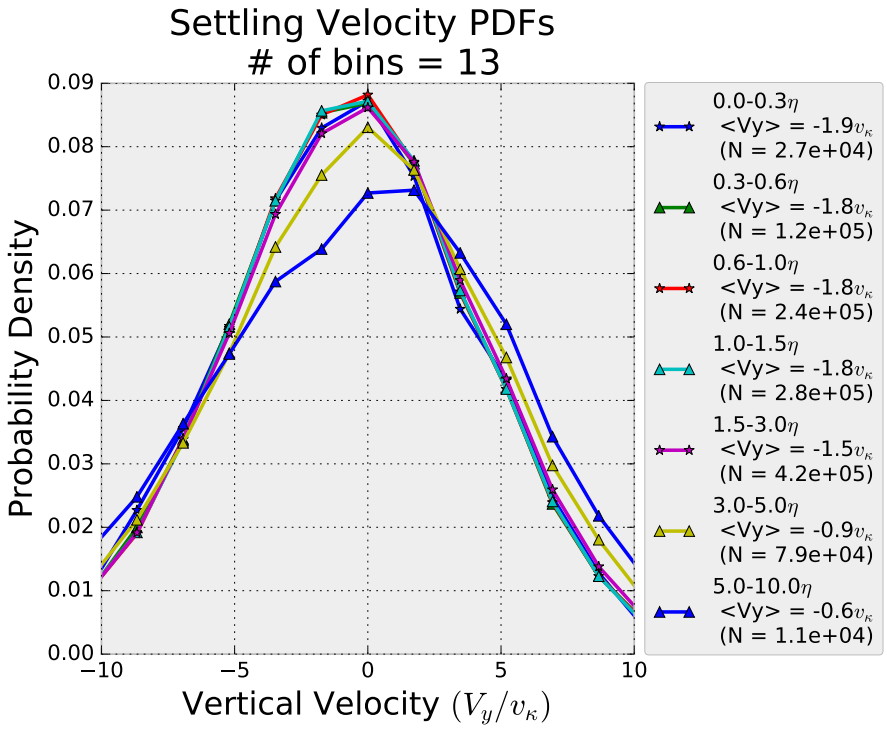

Figure A.2: Settling velocity Probability Density Functions (PDF) measured at $x = 30$M. The PDFs are plotted as a function of vertical velocity (V_y) scaled by the Kolmogorov velocity (v_κ). The data is binned according to distance to the nearest neighboring droplet measured in multiples of the Kolmogorov length (η). The legend shows the the number (N) of droplets in the bin, as well as the mean velocity ($\langle V_y \rangle$), in therm of the Kolmogorov velocity, for all those droplets.

Appendix B

ADDITIONAL TURBULENCE ENERGY SPECTRA PLOTS

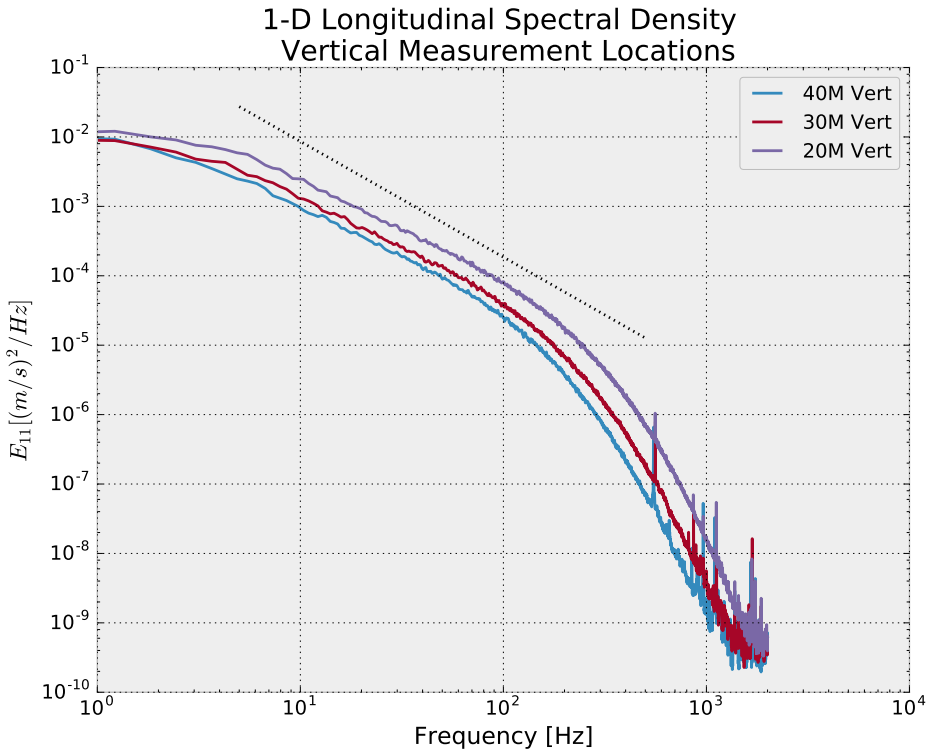

Figure B.1: A plot of the longitudinal 1D turbulent energy spectrum from hotwire measurements made at the vertical high-speed imaging location for Stations 20M, 30M, and 40M. The dashed line, with a -5/3 slope, is included as a visual reference for the slope predicted by Kolmogorov's theory for the inertial range of turbulent energy spectra.

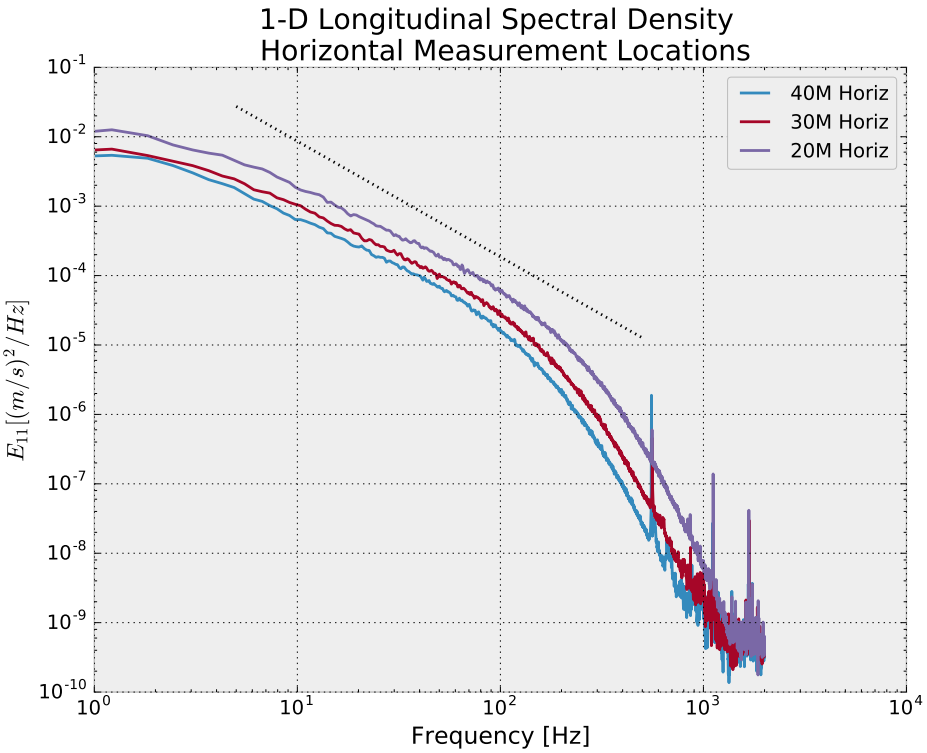

Figure B.2: A plot of the longitudinal 1D turbulent energy spectrum from hotwire measurements made at the horizontal high-speed imaging location for Stations 20M, 30M, and 40M. The dashed line, with a -5/3 slope, is included as a visual reference for the slope predicted by Kolmogorov's theory for the inertial range of turbulent energy spectra.

Appendix C

HOTWIRE ANENOMETRY (HWA) - CALIBRATION AND ERROR ANALYSIS

C.1 HWA Calibration

We calibrated the HWA by making co-located hotwire and pitot tube measurements over a range of velocities. The differential pressure in the pitot tube was measured using a pressure transducer* and the resultant velocities were related to corresponding hotwire voltage data using a 4th order polynomial fit (Figure C.1).

C.2 HWA Error Analysis

To evaluate the error in the HWA measurements, we use the evolution of the velocity RMS statistics. If a time-series (x) with mean (X) and "true" variance (σ^2) is split into i independent samples (x_i), the variance in the mean calculated from N independent samples is related to the variance of the entire time-series by $\mathrm{VAR}(X_N) \sim \sigma^2/N$ (George et al., 1978).

In our measurements, when we split a single time series into 50 independent, non-overlapping samples of 20,000 velocity measurements each, we observed that the variance in the mean velocity asymptotes to a constant value and does not decrease like $1/N$ as predicted by the theory. We deduced that the component of the variance due to the turbulent fluctuations decays according to the theory, but the truly random error in the HWA system persists (Figure C.2). The asymptotic value of the variance is thus the error of the HWA. On average across the core region we found this error to be less than 5% of the full measurement.

---

*OMEGA® PX653 with a resolution of 2.5×10^{-4} in. H_2O (0.06 Pa)

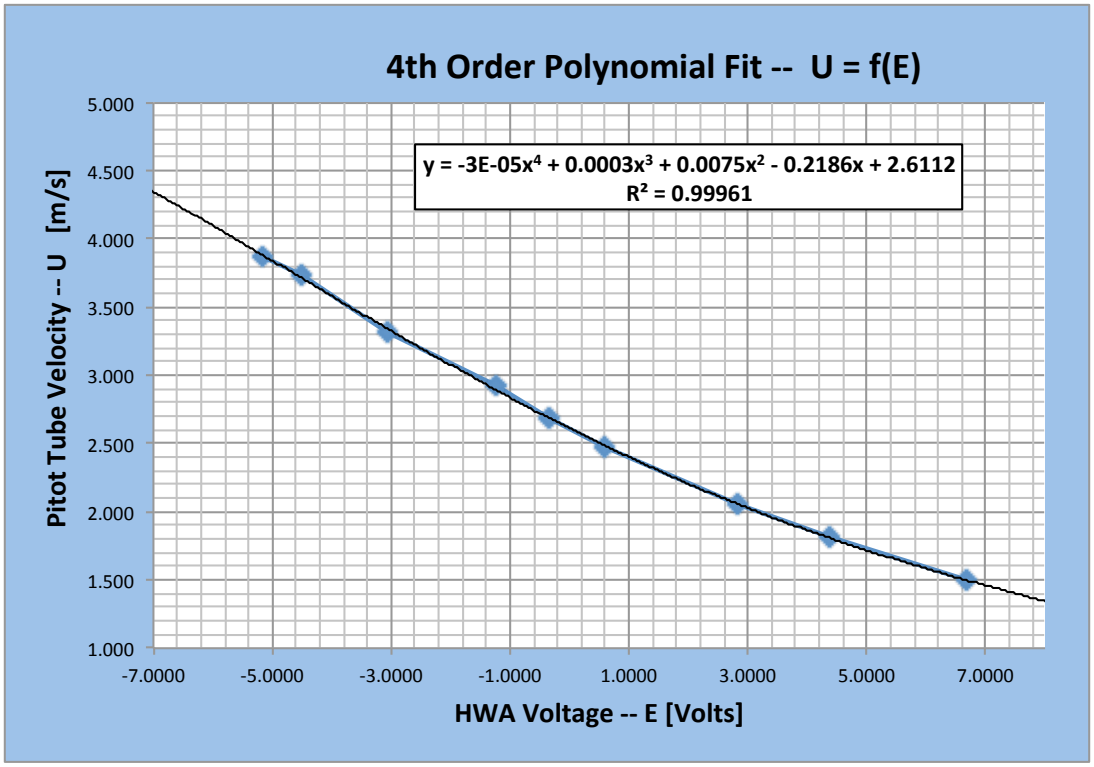

Figure C.1: A plot showing the hotwire calibration equation; a 4th order polynomial fit to the Pitot tube velocities and the corresponding hotwire voltages measurements.

A second source of error in our velocity measurements results from using a single component hotwire probe and ignoring the significant fluctuations in the two other components. We estimate this error to be less than 2% of the mean streamwise velocity since our turbulence intensities are always below 0.2 (Goldstein, 1996).

The uncertainty in our calibration was less than 1% across our entire velocity range. Thus our estimate of the total error in the HWA velocity measurements is approximately 8%.

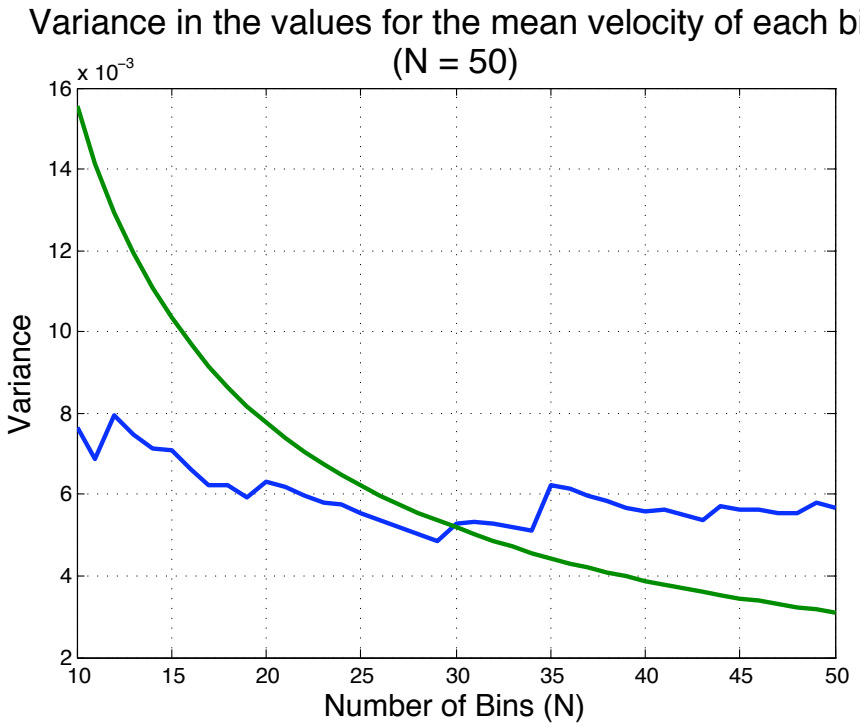

Figure C.2: A plot showing the variance in the mean value of N independent, non-overlapping samples of the HWA measurement of the RMS velocity (blue curve) compared to the analytical value of the variance as predicted by (George et al., 1978) (green curve).

Appendix D

PITOT RAKE INSTRUMENT ERROR CHARACTERIZATION

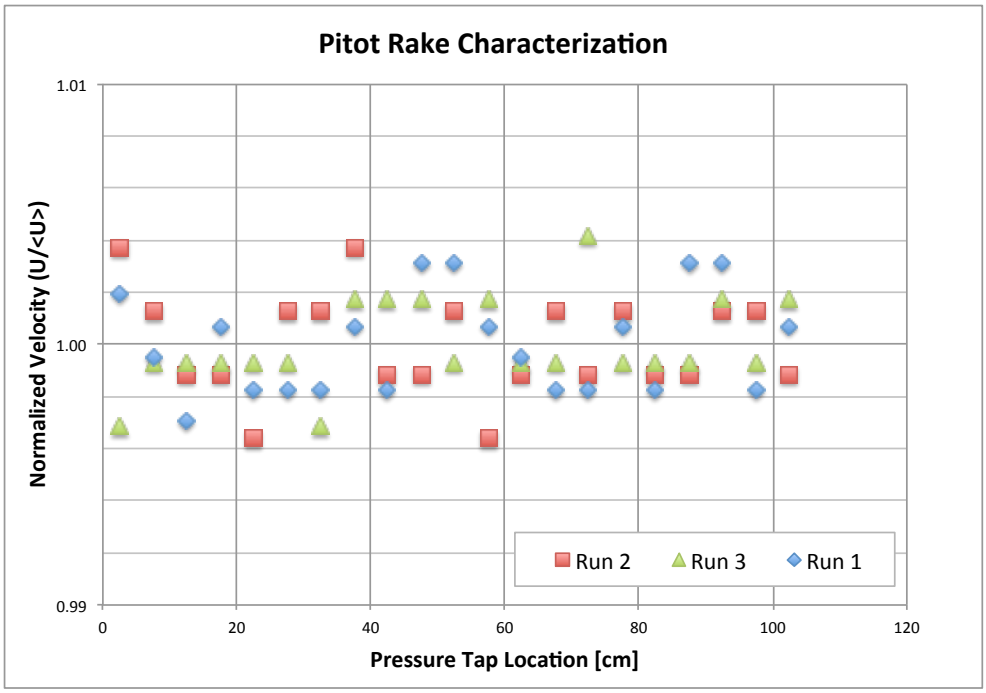

Figure D.1: Pitot Rake Instrument Error Characterization. A plot showing the velocities measured at each location along the pitot rake when exposed to a constant velocity flow source. The experiment was repeated three times.